METHODOLOGIES FOR ELECTROMAGNETIC FIELD MODELING FOR COMPUTER AIDED ANALYSIS OF MULTI-DOMAIN PHYSICAL INTERACTIONS

BY

JOHANNES ANTON RUSSER

DISSERTATION

Submitted in partial fulfillment of the requirements
for the degree of Doctor of Philosophy in Electrical and Computer Engineering
in the Graduate College of the
University of Illinois at Urbana-Champaign, 2010

Urbana, Illinois

Doctoral Committee:

Professor Andreas C. Cangellaris, Chair
Professor Jianming Jin
Professor Umberto Ravaioli
Professor José E. Schutt-Ainé

Abstract

Several methodologies are presented in this work to facilitate the modeling of electromagnetic fields in the context of multi-domain physical interactions. Among the challenges for computer aided analysis of electromagnetic problems in interaction with other physical phenomena are the largely different temporal and spatial scales that may occur and the task of maintaining accuracy and computational efficiency in the implementation of boundary conditions for time-varying media.

First, we present a methodology for the phenomenological modeling of passive intermodulation generation in metallic contacts due to electron tunneling. The methodology provides for the development of passive intermodulation source models that are compatible with general-purpose electromagnetic and non-linear network analysis-oriented circuit simulators. The derived model allows for an investigation of the impact of surface roughness and skin effect on the levels and frequency dependence of passive intermodulation interference. Thus, the model is intended to enhance the understanding of the passive intermodulation source due to electron tunneling in metallic contacts.

The second methodology presented is a Lagrangian approach for increasing the accuracy of the finite difference time domain method for modeling wave propagation in geometries involving curved and moving boundaries. This methodology provides for the definition of an equivalent electromagnetic boundary value problem over a domain with fixed boundaries. A modified time-dependent operator is derived for

the Lagrangian formulation, operating on a modified set of Maxwell's equations on a reference domain. This method relaxes spatial oversampling requirement and achieves high accuracy and computational efficiency.

The third methodology provides for an efficient analysis of problems with widely separated time scales. We propose the application of the method of multi-time partial differential equations to the numerical solution of one-dimensional electromagnetic wave interactions involving highly disparate temporal variations in both excitation and time-varying media properties and boundary conditions. The temporal oversampling requirement is relaxed by introducing multiple time scales for quasi-periodic functions and, upon solution of the multivariate partial differential equation, we recover a solution to the univariate problem.

To my family

Acknowledgments

I would like to express my deepest gratitude to my adviser, Professor Andreas Cangellaris, for his enduring support and guidance, his patience, and the countless discussions and the deep insights he has provided me with. Working with him during the course of my research gave me many valuable experiences. I would like to sincerely thank my committee members — Professor Jianming Jin, Professor Umberto Ravaioli, and Professor José Schutt-Ainé — for their valuable comments and suggestions that helped me to complete and improve this work. Furthermore, I am very indebted to Dr. Mehyar Khazei for his support and the valuable experience I was able to gain during my time working for Qualcomm Inc.

Special thanks go to Prasad Sumant whose quasi-elastic solver I have used in Chapter 5. I would like to thank him, Dr. Anand Ramachandran, Dr. Aravind Ramachandran, and Dr. Anne Woo for many interesting and exciting discussions. I would like to extend my thanks to all my colleagues and friends in the electromagnetics laboratory who helped me with the diverse questions that occur now and then, who worked on projects together with me or simply provided good company and discussions.

Last but not least, I would like to thank my family. I thank my parents for their enduring support and love all through my life. Furthermore, I thank my siblings Martin and Andrea for their encouragement. My gratitude also goes to my late aunt Herta for all her encouragement and love. Finally, I am very thankful to my dear wife Moushumi who is always there for me.

Table of Contents

List of Figures

List of Symbols

A_{pl} plate surface area, page 18

$\boldsymbol{B}$ magnetic flux density, page 9

$\overline{\boldsymbol{c}}$ elastic tensor, page 3

c speed of light, page 14

C_p parallel capacitance, page 24

C_{pl} capacitance of parallel plate capacitor, page 18

d plate separation, page 18

$D_{x_1 x_2}^{\alpha_1 \alpha_2}$ Jacobian determinant, page 38

D_N Fourier interpolation derivative matrix, page 78

$\boldsymbol{D}$ electric flux density, page 9

$\mathcal{D}_N u$ Fourier interpolation derivative, page 77

$\tilde{\mathcal{D}}$ matrix of Jacobian determinants, page 38

$\overline{\boldsymbol{e}}$ piezoelectric tensor, page 3

e electron charge, page 24

$\boldsymbol{E}$ electric field intensity, page 9

$\tilde{\boldsymbol{E}}$ mapped electric field vector, page 38

$\hat{\boldsymbol{E}}$ multi-time electric field vector, page 79

f frequency, page 28

$\boldsymbol{F}_{EK}$ net electrokinetic body force, page 3

$\mathcal{F}$ deformation gradient matrix, page 37

G_p parallel conductance, page 24

$\mathcal{G}$ mapping matrix, page 37

h Planck's constant, page 24

$\boldsymbol{H}$ magnetic field intensity, page 9

$\tilde{\boldsymbol{H}}$ mapped magnetic field vector, page 38

$\hat{\boldsymbol{H}}$ multi-time magnetic field vector, page 79

I electric current, page 24

j imaginary unit, $j = \sqrt{-1}$, page 14

J electric current density, page 24

$\boldsymbol{J}_e$ electric current, page 9

$\boldsymbol{J}_m$ magnetic current, page 9

$\boldsymbol{J}_{e0}$ impressed electric current, page 9

$\boldsymbol{J}_{m0}$ impressed magnetic current, page 9

$\tilde{k}$ numerical propagation vector, page 14

$\boldsymbol{k}$ propagation vector, page 14

L_s series inductance, page 24

m_e mass of the electron, page 24

$\boldsymbol{M}$ magnetic polarization, page 10

p pressure, page 3

P_IMF spectral power at intermodulation frequency, page 28

$\boldsymbol{P}$ electric polarization, page 10

r correlation coefficient, page 30

R_s series resistance, page 24

s complex number for Laplace transform, $s = j\omega$, page 27

s_ox thickness oxide film, page 24

t time, page 14

$\tan\delta$ loss tangent, page 27

U mechanical displacement, page 3

U_bp barrier potential, page 16

$\boldsymbol{u}_v$ velocity field, page 3

V voltage, page 18

Y_p parallel admittance, page 24

Z_s series impedance, page 24

Δ finite difference, page 12

∂ partial derivative symbol, page 3

$\overline{\boldsymbol{\epsilon}}$ dielectric permittivity tensor, page 10

ϵ_0 dielectric permittivity, page 10

λ wave length, page 15

μ_0 magnetic permeability, page 10

μ_v dynamic viscosity, page 3

$\overline{\mu}_p$ expectation value of spectral power, page 28

$\overline{\boldsymbol{\mu}}$ magnetic permeability tensor, page 10

π circular constant, page 55

ρ' equivalent magnetic resistivity, page 9

ρ_e electric charge density, page 9

ρ_f fluid density, page 3

ρ_{Al} resistivity of aluminium, page 27

ρ_{oxide} resistivity of oxide, page 27

σ electric conductivity, page 9

σ_p standard deviation of spectral power, page 28

ϕ electric potential, page 3

φ_0 work function, page 24

ω angular frequency, page 3

ω_r resonant frequency, page 50

$\Delta\omega_r$ shift in resonant frequency, page 50

∇ Nabla operator ("del"), page 9

$\tilde{\nabla}$ modified Nabla operator, page 39

$\times$ vector multiplication of two vectors, page 9

$\cdot$ scalar multiplication of two vectors, page 9

List of Abbreviations

ABC	absorbing boundary condition
ADI	alternate direction implicit
AMR	adaptive mesh refinement
BVP	boundary value problem
CFL	Courant-Friedrichs-Lewy
CPW	coplanar waveguide
DFT	discrete Fourier transform
EM	electromagnetic
EOF	electro-osmotic flow
FD	frequency domain
FDTD	finite difference time domain
FEM	finite element method
FT	Fourier transform
FWHM	full-width at half-maximum
IC	integrated circuit
IDFT	inverse discrete Fourier transform
IMF	intermodulation frequency
IML	intermodulation level
LM	Lagrangian mapping
MCM	Monte Carlo method

MEMS	micro-electro-mechanical-system
MoM	method of moments
MPDE	multi-time partial differential equation
MRTD	multiresolution time domain
NEMS	nano-electro-mechanical-system
PDE	partial differential equation
PEC	perfectly electrically conducting
PIM	passive intermodulation
PMC	perfectly magnetically conducting
PML	perfectly matched layer
RF	radio frequency
SAW	surface acoustic wave
TD	time domain
TE	transverse electric
TEM	transverse electromagnetic
TLM	transmission line matrix
TM	transverse magnetic
WKBJ	Wentzel-Kramers-Brillouin-Jeffreys

Chapter 1

Introduction

1.1 The Problem

As the fabrication and integration techniques of nano- and microscale devices have advanced, new possibilities have opened up for the design of devices incorporating aspects of different physical domains. Electro- and magnetostatic, electrodynamic, mechanical, quantum mechanical, thermal and fluid-dynamical effects can contribute to the functionality of these devices. Clearly, advances in the modeling techniques are required to combine numerical solvers of these different domains in order to allow for efficient and accurate modeling of new designs prior to their realization in the lab, and these techniques are currently being pushed forward. *Multiphysics modeling* is the term that has been coined in order to refer to techniques which attempt to couple physical modeling domains which traditionally had been separated. It includes analytic and numerical modeling techniques and deals with problems like the coupling of the electrical and acoustic domain for piezo-acoustic transducers or surface acoustic wave (SAW) filters and resonators [1] or electrostatically controlled microchannels that transport fluids for chemical analysis or applications like inkjet printers [2–4]. Mechanical switches realized as micro-electro-mechanical-systems (MEMS) [5] have brought great benefit, like reduced insertion loss and improved linearity, to radio frequency (RF) integrated circuits (IC). Tunable capacitors and acceleration sensors have been realized as MEMS. Quantum effects become relevant in electric conduc-

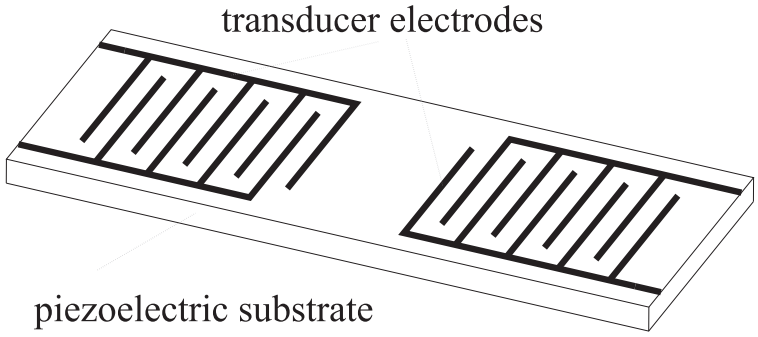

Figure 1.1: SAW filter structure.

tors with metal-oxide-metal contacts or for RF switches realized as nano-electro-mechanical-systems (NEMS) using carbon nanotubes [6]. Accounting for generation and distribution of thermal energy in the design process of mechanical or electric devices may improve models as the temperature change feeds back into the mechanical and electrical properties of the device. Multiphysics techniques strive for the hybridization of different modeling techniques to achieve a unified modeling process from the atom- to the system level [7].

SAW filters take advantage of the relatively low propagation velocity of acoustic waves, usually around 3×10^3 to 1×10^4 m/s compared to electromagnetic (EM) waves at 3×10^8 m/s in vacuum, allowing for significant time delay of signals on a small device footprint. Thus SAW filters are today ubiquitous in cellular phone and other mobile radio systems. Crystalline structures like lithium tantalate ($LiTaO_3$), lithium niobate ($LiNbO_3$), or quartz (α-SiO_2) with a low attenuation coefficient and strong piezoelectric coupling between the acoustic and the EM wave are commonly used for SAW devices [8]. Figure 1.1 shows a SAW filter structure with two interdigital transducers converting the EM signal to the acoustic domain and back again. The

elastic surface wave propagation in a piezoelectric is described by [9–12]

$$c_{ijkl}\partial^2 U_k/\partial x_l \partial x_i + e_{kij}\partial^2\phi/\partial x_k\partial x_i + \omega^2\rho U_j = 0, \qquad j = 1,2,3 \tag{1.1}$$

$$e_{ikl}\partial^2 U_k/\partial x_l \partial x_i - \epsilon_{ik}\partial^2\phi/\partial x_k\partial x_i = 0\,, \tag{1.2}$$

where c_{ijkl} is an element of the elastic, e_{ikl} of the piezoelectric, and ϵ_{ik} of the dielectric tensor. These equations are coupled to Maxwell's equations in their electrostatic approximation via

$$E_j = -\partial\phi/\partial x_j \tag{1.3}$$

$$\partial D_j/\partial x_j = 0\,, \tag{1.4}$$

where $\boldsymbol{E}$ is the electric field, ϕ the electric potential and U the mechanical displacement.

An example of the interaction of electrostatics with fluid dynamics is the electro-osmotic flow (EOF), which is an electrokinetic effect that allows one to control the flow in microchannnels [2, 13, 14]. EOF provides more control over the fluid transport and is more convenient to implement than hydraulic pressure flow. A precondition for the EOF is that an imprint surface charge at the walls of the microchannel, as common to many materials, will be compensated by a charge accumulation of the fluid in proximity to the channel wall. An applied electrostatic field will exert force to the particles in the layer of accumulated charge. Viscous forces act on the remainder fluid causing the EOF. The EOF is illustrated in Figure 1.2. The EOF is governed by the Navier-Stokes equation [2]

$$\rho_f\big(\frac{\partial \boldsymbol{u}_v}{\partial t} + (\boldsymbol{u}_v\cdot\nabla)\boldsymbol{u}_v\big) = -\nabla p + \mu_v\nabla^2\boldsymbol{u}_v + \boldsymbol{F}_{EK} \tag{1.5}$$

and by the equation for the electrokinetic force

$$\boldsymbol{F}_{EK} = \rho_e \boldsymbol{E} - \frac{1}{2}\boldsymbol{E}\cdot\boldsymbol{E}\epsilon_0\nabla\epsilon + \frac{\epsilon_0}{2}\nabla\left(\rho_f \frac{\partial\epsilon}{\partial\rho_f}\boldsymbol{E}\cdot\boldsymbol{E}\right), \tag{1.6}$$

where ρ_f is the fluid density, $\boldsymbol{u}_v$ is the velocity field, p is the pressure, μ_v is the dynamic viscosity, and $\boldsymbol{F}_{EK}$ is the net electrokinetic body force acting on the fluid.

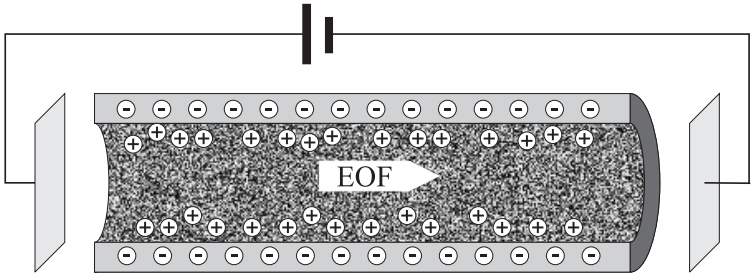

Figure 1.2: Electro-osmotic flow.

The above problems are intended to demonstrate the relevance of multiphysics modeling approaches. Furthermore, these cases can serve as examples for a localized change of dielectric material properties due to mechanical deformation or controlled fluid transport. Acoustic coupling to a dielectric slab causes mechanical deformation of the slab's boundaries as well as a modulation of the dielectric properties. We will investigate in this work a technique to incorporate time-varying boundaries in the context of electrodynamic field modeling. A tight coupling of the different physical domains in the modeling process will bring dramatic improvement to the performance of devices and systems.

1.2 State of the Art

Numerous numerical techniques have been developed over the past few decades to solve complex physical problems for which analytic solutions are non-existent or hard to access. In electromagnetics, some of these techniques have been adapted from other

engineering disciplines like structural mechanics or fluid dynamics. Optimization and refinement of numerical solvers, in order to improve accuracy and computational performance, are subjects of permanent research interest in order to provide for modeling tools for cutting edge devices.

Numerical methods solve electromagnetic boundary value problems either in time-domain (TD) or in the frequency domain (FD) with the Fourier transform (FT) providing the necessary link between these two domains [15]. These methods can be further categorized according to whether they are based on the integral equation or differential equation formulation of Maxwell's equations (2.1)-(2.4). Problems with open radiating structures, closed structures, or narrow or broad frequency spectrum of interest may be solved computationally more efficiently with specific methods. TD methods, for example, can accommodate nonlinearities in a more direct way than FD techniques which have to rely on special techniques like harmonic balance [16, 17].

Amongst the widely used methods are the method of moments (MoM) [18], the finite element method (FEM) [19], the finite difference time domain (FDTD) method [20, 21], and the transmission line matrix (TLM) method [22, 23]. MoM and FEM are most commonly implemented in the frequency domain, whereas the FDTD method and the TLM method are usually implemented in the time domain. However, TD and FD implementations exist for all of the above methods. The TLM method is based on a network representation of Maxwell's equations; the other three methods are based on the field representation of Maxwell's equations.

Higher level electronic systems are modeled by network analysis tools like SPICE[1] [24, 25]. Low level models are incorporated in high level models by deriving models with reduced complexity. This is done for example with transistor models in network analysis tools which provide current-voltage characteristics for the device derived

[1]SPICE: Simulation Program with Integrated Circuit Emphasis

from a model based on quantum mechanics. Deriving simplified models from complex physical problems or problems accessible only phenomenologically can be achieved by the technique of macro- or reduced order modeling [26, 27]. Low level problems on an atomistic scale are often modeled with probabilistic techniques like the Monte Carlo method (MCM) [28, 29] or with the help of mesh-free modeling techniques [30].

In hierarchical methodologies information is often lost between the modeling levels and thus feedback, in particular from the higher level model to the lower level model, is often incomplete, reducing the capability to model complex systems.

In recent years interest has grown to couple electromagnetic solvers more tightly with other physical solvers. Commercial solvers for multiphysics problems have become available, like ANSYS[2] or COMSOL[3] [31, 32], which provide capabilities to couple electromagnetic phenomena to problems of heat transfer and structural mechanics. Critical for multiphysics modeling is the handling of the different spatial resolutions required for models in the different physical domains. Another challenge is imposed to the electromagnetic field modeling by the time variation of the physical boundaries.

1.3 Summary of this Work

This thesis provides methodologies that facilitate the handling of multiple scales and variable structures in the electromagnetic field domain and thus aims to improve computer aided analysis of multiphysics problems. Chapter 2 will provide fundamental equations and theory for the work presented subsequently.

In Chapter 3 we present a methodology for the phenomenological modeling of passive intermodulation (PIM) generation due to electron tunneling in metallic contacts

[2]ANSYS Inc., 275 Technology Dr., Canonsburg, PA 15317, U.S.A., `http://www.ansys.com`
[3]COMSOL AB, Tegnérgatan 23, SE-111 40 Stockholm, Sweden, `http://www.comsol.com`

in the signal transmission path of an RF/microwave system. The model aims at enhancing the understanding of this type of PIM source through the investigation of the impact of surface roughness and skin effect on the levels and frequency dependence of PIM interference. The methodology is such that it provides for the development of PIM source models for metallic contacts that are compatible with general-purpose electromagnetic and network analysis-oriented, non-linear circuit simulators.

Chapter 4 presents a Lagrangian approach for increasing the accuracy of the finite difference time domain method in modeling electromagnetic wave interactions in geometries involving curved and moving boundaries. The methodology, which is implemented numerically using the FDTD method, relies upon the definition of an equivalent electromagnetic boundary value problem (BVP) over a domain with fixed boundaries but with a modified operator exhibiting time variation. The Lagrangian formulation offers a convenient way to define a modified set of Maxwell's equations on a reference domain. This modified set of equations is then discretized using the staggered Cartesian grids of the Yee's lattice. The attributes of the method are demonstrated in several examples in Chapter 5.

In Chapter 6 we discuss the technique of multi-time partial differential equations and its implementation to solve the electromagnetic wave equation. For problems which exhibit certain periodic properties for their solution, this technique allows for an expansion of the time variable into multiple variables which are all dependent variables to the partial differential equation. This may reduce the computational cost for problems with widely separated time scales. Towards the implementation of the multivariate technique we will give an introduction to spectral methods. The formulation and a numerical example of the solution of the one-dimensional wave equation are given subsequently.

Finally, the presented work is summarized and directions for future research are

outlined in Chapter 7.

Chapter 2

The Fundamental Equations

2.1 Partial Differential Equations in Electrodynamics

The phenomena of electromagnetic wave propagation are governed by Maxwell's equations, in their differential form given as

$$\nabla \times \boldsymbol{E}(\boldsymbol{r},t) = -\frac{\partial \boldsymbol{B}(\boldsymbol{r},t)}{\partial t} - \boldsymbol{J}_m(\boldsymbol{r},t)\,, \tag{2.1}$$

$$\nabla \times \boldsymbol{H}(\boldsymbol{r},t) = \frac{\partial \boldsymbol{D}(\boldsymbol{r},t)}{\partial t} + \boldsymbol{J}_e(\boldsymbol{r},t)\ , \tag{2.2}$$

$$\nabla \cdot \boldsymbol{D}(\boldsymbol{r},t) = \rho_e(\boldsymbol{r},t)\,, \tag{2.3}$$

$$\nabla \cdot \boldsymbol{B}(\boldsymbol{r},t) = 0\,, \tag{2.4}$$

where $\boldsymbol{E}$ and $\boldsymbol{H}$ are electric and magnetic field intensity, $\boldsymbol{D}$ and $\boldsymbol{B}$ the electric and magnetic flux density, $\boldsymbol{J}_e$ and $\boldsymbol{J}_m$ the electric and magnetic current, and ρ_e the electric charge density [33, 34]. The currents are defined as

$$\boldsymbol{J}_e(\boldsymbol{r},t) = \boldsymbol{J}_{e0}(\boldsymbol{r},t) + \sigma \boldsymbol{E}(\boldsymbol{r},t)\,, \tag{2.5}$$

$$\boldsymbol{J}_m(\boldsymbol{r},t) = \boldsymbol{J}_{m0}(\boldsymbol{r},t) + \rho' \boldsymbol{H}(\boldsymbol{r},t)\,, \tag{2.6}$$

where $\boldsymbol{J}_{e0}(\boldsymbol{r},t)$ and $\boldsymbol{J}_{m0}(\boldsymbol{r},t)$ are the impressed electric and magnetic current, σ is the electric conductivity, and ρ' equivalent magnetic resistivity. The electric and magnetic field intensities are linked to the respective flux densities by the constitutive relations

$$\boldsymbol{D}(\boldsymbol{r},t) = \epsilon_0 \boldsymbol{E}(\boldsymbol{r},t) + \epsilon_0 \boldsymbol{P}(\boldsymbol{r},t)\,, \tag{2.7}$$

$$\boldsymbol{B}(\boldsymbol{r},t) = \mu_0 \boldsymbol{H}(\boldsymbol{r},t) + \mu_0 \boldsymbol{M}(\boldsymbol{r},t)\,, \tag{2.8}$$

where ϵ_0 is the free space dielectric permittivity, μ_0 is the free space magnetic permeability, $\boldsymbol{P}$ is the electric polarization and $\boldsymbol{M}$ is the magnetic polarization. For non-dispersive media the above relation can be cast as

$$\boldsymbol{D}(\boldsymbol{r},t) = \epsilon_0 \overline{\boldsymbol{\epsilon}}_r \boldsymbol{E}(\boldsymbol{r},t)\,, \tag{2.9}$$

$$\boldsymbol{B}(\boldsymbol{r},t) = \mu_0 \overline{\boldsymbol{\mu}}_r \boldsymbol{H}(\boldsymbol{r},t)\,, \tag{2.10}$$

$$\overline{\boldsymbol{\epsilon}}_r = \begin{bmatrix} \epsilon_{r_{xx}} & \epsilon_{r_{xy}} & \epsilon_{r_{xz}} \\ \epsilon_{r_{yx}} & \epsilon_{r_{yy}} & \epsilon_{r_{yz}} \\ \epsilon_{r_{zx}} & \epsilon_{r_{zy}} & \epsilon_{r_{zz}} \end{bmatrix}\,, \qquad \overline{\boldsymbol{\mu}}_r = \begin{bmatrix} \mu_{r_{xx}} & \mu_{r_{xy}} & \mu_{r_{xz}} \\ \mu_{r_{yx}} & \mu_{r_{yy}} & \mu_{r_{yz}} \\ \mu_{r_{zx}} & \mu_{r_{zy}} & \mu_{r_{zz}} \end{bmatrix}\,, \tag{2.11}$$

where $\overline{\boldsymbol{\epsilon}}_r$ is the relative dielectric permittivity tensor and $\overline{\boldsymbol{\mu}}_r$ is the relative magnetic permeability tensor. Hence, Maxwell's equations (2.1)-(2.4) constitute a set of two coupled first order partial differential equations (PDEs) or can be written as a single second order hyperbolic PDE [35, 36].

2.2 The FDTD Method

The FDTD method is applied in electromagnetics by discretizing the partial differences on a spatial and temporal grid. Several differencing schemes are available. The Euler method provides a basic differencing scheme which is derived by truncating the Taylor-series expansion of the partial derivative at the desired order [36, 37]. Backward, central and forward Euler schemes exist, named according to the location of the supporting numerical nodes in the finite difference equation. Further numerical differencing schemes include the Crank-Nicolson scheme [37, 38], which is an implicit and unconditionally stable scheme, or the Leapfrog scheme [37]. We will briefly discuss in the following the FDTD implementation of Maxwell's equations in the Yee scheme and some aspects pertinent to it.

2.2.1 Yee's staggered grid

In the Yee scheme [20] Maxwell's equations (2.1)-(2.4) are approximated by a finite difference scheme. Electric and magnetic field values and their respective flux quantities are discretized on a staggered grid, as shown in Figure 2.1. Dielectric and magnetic fluxes can be obtained easily by evaluation of the magnetic and electric field quantities along a circular path on the respective staggered grid. Electric and magnetic field quantities are alternately updated. The applied central difference scheme is explicit, has a low memory requirement since the field values have to be stored for only one time step, and allows for a convenient implementation of boundary conditions where the $\boldsymbol{E}$- and $\boldsymbol{H}$-field can both be enforced. The resulting algorithm is numerically robust and easy to implement, which makes it a very attractive choice. For convenience we shall write the time index of a function u as upper index and the

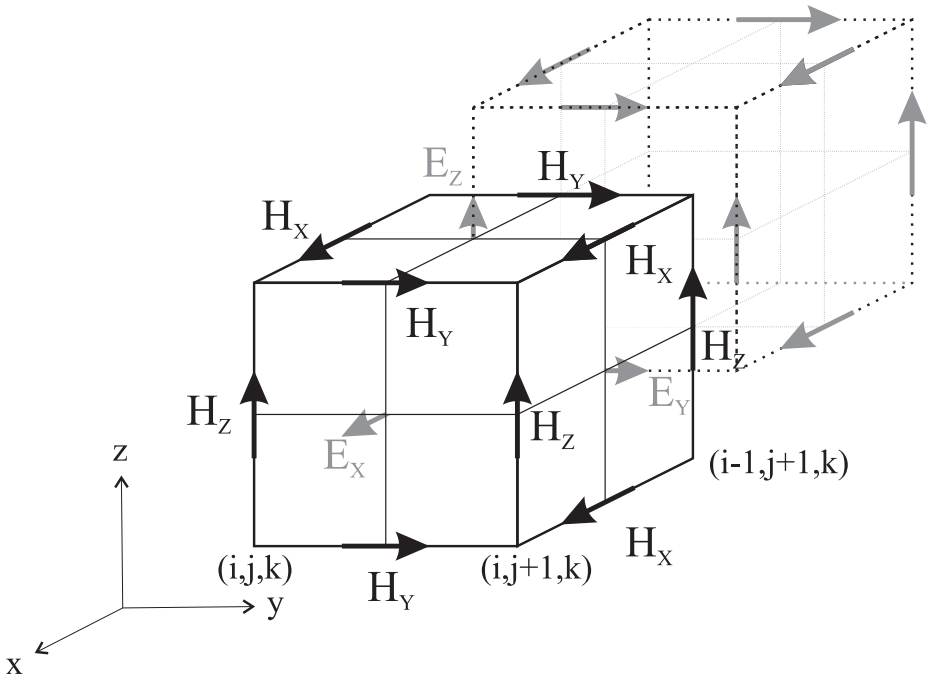

Figure 2.1: Yee's staggered grid.

spatial ones are denoted as lower indices

$$u|^n_{i,j,k} \equiv u(i\Delta x, j\Delta y, k\Delta z, n\Delta t)\,, \tag{2.12}$$

and for a vector-valued $\boldsymbol{u}$ we write

$$\boldsymbol{u} =< u_x\hat{\boldsymbol{x}}, u_y\hat{\boldsymbol{y}}, u_z\hat{\boldsymbol{z}} >^T\ . \tag{2.13}$$

Since the $\boldsymbol{E}$- and $\boldsymbol{H}$-field are evaluated half a time step apart, field values in between are averaged by

$$\boldsymbol{u}|^n_{i,j,k} = \frac{\boldsymbol{u}|^{n-1/2}_{i,j,k} + \boldsymbol{u}|^{n+1/2}_{i,j,k}}{2}\,. \tag{2.14}$$

The first order partial difference is approximated by the finite difference

$$\frac{\partial u|^n_{i,j,k}}{\partial x} \approx \frac{u|^n_{i+1/2,j,k} - u|^n_{i-1/2,j,k}}{\Delta x}\,. \tag{2.15}$$

Thus, the resulting update equations in Yee's scheme for fields $\hat{\boldsymbol{x}}$-components are given by [21]

$$H_x|_{i,j,k}^{n+1/2} = \left(\frac{1-\frac{\rho'_{i,j,k}}{2\mu_{i,j,k}}}{1+\frac{\rho'_{i,j,k}}{2\mu_{i,j,k}}}\right) H_x|_{i,k}^{n-1/2} + \left(\frac{\frac{\Delta t}{\mu}}{1+\frac{\rho'_{i,j,k}\Delta t}{2\mu_{i,j,k}}}\right)\left(\frac{E_y|_{i,j,k+1/2}^{n} - E_y|_{i,j,k-1/2}^{n}}{\Delta z} - \frac{E_z|_{i,j+1/2,k}^{n} - E_z|_{i,j-1/2,k}^{n}}{\Delta y}\right), \tag{2.16}$$

$$E_x|_{i,j,k}^{n+1} = \left(\frac{1-\frac{\sigma_{i,j,k}\Delta t}{2\epsilon_{i,j,k}}}{1+\frac{\sigma_{i,j,k}}{2\epsilon_{i,j,k}}}\right) E_x|_{i,j,k}^{n} + \left(\frac{\frac{\Delta t}{\epsilon_{i,j,k}}}{1+\frac{\sigma_{i,j,k}\Delta t}{2\epsilon_{i,j,k}}}\right)\left(\frac{H_z|_{i,j+1/2,k}^{n+1/2} - H_z|_{i,j-1/2,k}^{n+1/2}}{\Delta y} - \frac{H_y|_{i,j,k+1/2}^{n+1/2} - H_y|_{i,j,k-1/2}^{n+1/2}}{\Delta z}\right), \tag{2.17}$$

and analog equations are found for H_y, H_z, E_y, and E_z.

2.2.2 Convergence, stability and numerical dispersion

Let us denote the exact solution of a PDE as U, whereas its numerical approximation shall be u. The PDE's independent variables are x, y and z. The finite difference solution is called convergent if u tends to U at a fixed point as Δx, Δy, and Δz all go to zero [35]. According to Lax' equivalence theorem, the finite difference approximation to the initial value problem is convergent if the approximation satisfies the consistency condition and is stable [39, 40]. Let $L(U) = 0$ be the representation of the PDE with the exact solution U and $F(u) = 0$ be the representation of the finite difference approximation to the PDE. The truncation error at the grid point (i, j, k) is thus

$$T_{i,j,k}(v) = F_{i,j,k}(v) - L(v_{i,j,k})\,, \tag{2.18}$$

where v is a continuous function of x, y, and z. The function is called consistent if $T_{i,j,k} \to 0$ as $\Delta x \to 0$, $\Delta y \to 0$, and $\Delta z \to 0$.

The stability refers to the boundedness of the finite difference solution as it is propagated forward. Different schemes exist to ensure the boundedness of the solution of the finite difference approximation and of rounding errors. The Fourier series method and the amplification matrix method belong to the most widely used methods [35, 41]. The Yee algorithm is conditionally stable. In order to prevent unbounded growth the time step has to be limited. The Courant-Friedrichs-Lewy (CFL) condition provides the criteria for the stability of explicit finite difference PDE approximations [42]. The CFL condition demands for Yee's time-marching scheme that values on the numerical grid are not propagated with a numerical velocity faster than the actual velocity. Thus Yee's scheme for three-dimensional problems is found to be stable for

$$\Delta t \leq \frac{1}{c\sqrt{\frac{1}{(\Delta x)^2} + \frac{1}{(\Delta y)^2} + \frac{1}{(\Delta z)^2}}}\,. \tag{2.19}$$

Numerical dispersion occurs in the FDTD scheme and it is determined by the propagation direction of the wave on the numerical grid and by the discretization of the grid. A time harmonic propagating wave is described by

$$u(\boldsymbol{x}, t) = e^{j(\omega t - \boldsymbol{k}\cdot\boldsymbol{x})}\,, \tag{2.20}$$

with $\boldsymbol{k} = \frac{\omega}{c}$ being the propagation vector. The numerical propagation vector $\tilde{k}$ in the finite difference solution to this equation is in general not identical to k. The

numerical dispersion relation is found to be [21]

$$\left(\frac{1}{c\Delta t}\sin\left(\frac{\omega\Delta t}{2}\right)\right)^2 = \left(\frac{1}{\Delta x}\sin\left(\frac{\tilde{k}_x\Delta x}{2}\right)\right)^2 + \left(\frac{1}{\Delta y}\sin\left(\frac{\tilde{k}_y\Delta y}{2}\right)\right)^2 + \\ + \left(\frac{1}{\Delta z}\sin\left(\frac{\tilde{k}_z\Delta z}{2}\right)\right)^2. \quad (2.21)$$

The dispersion error can be kept small by choosing a fine enough grid resolution. For a grid spacing of $\Delta x = \lambda/20$, where λ is the wave length, the phase velocity error relative to c is confined to -0.31% [21].

2.2.3 Absorbing boundary conditions

The computational domain for finite difference schemes has to be finite and a truncation will be necessary for any problem in an unbounded region. Multiple methods have been proposed to introduce absorbing boundary conditions (ABC) in the FDTD scheme [21]. The Sommerfeld radiation condition is known as an analytical boundary condition for radiation problems [43, 44]. Some ABC methods approximate this radiation condition for the FDTD scheme, e.g., the methods by Bayliss-Turkel [45], Engquist-Majda [46], or Mur [47]. The perfectly matched layer (PML) proposed by Bérenger [48, 49] introduces a nonphysical computational layer with provides impedance matching and high damping for an impinging wave.

2.3 Intermodulation Phenomena

Passive intermodulation (PIM) can be caused by bulk material nonlinearities, surface effects, and contact nonlinearities [50, 51]. Bulk nonlinearities occur in ferro- and ferrimagnetic as well as in dielectric material. Rough surfaces can give rise to nonlinear properties of the material surface and thus to PIM, in which case the current flow

direction relative to the surface abrasion will be critical for how strong an effect will occur [52]. So called a-spots [53] can give rise to PIM due to contact nonlinearities.

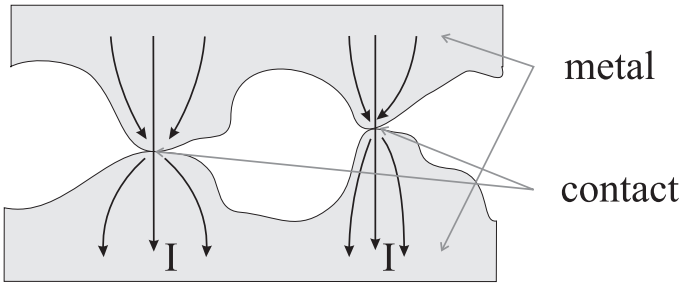

Figure 2.2: Current constriction to a-spots.

Due to the surface roughness and thus the non-perfect contact between two surfaces, the current is concentrated to contact spots as depicted in Figure 2.2. The local resistance and in particular the change of the resistance due to thermal effects gives rise to PIM. However, these metal-metal contact nonlinearities can be reduced if the pressure between the contact surfaces of the connector is increased, making metal-insulator-metal contact nonlinearities the dominant source for PIM [54, 55]. More specifically, the tunneling effect becomes dominant for thin contact layers [56]. For oxidized contact surfaces a potential barrier is introduced, hampering the free current flow. This potential barrier U_{bp} is plotted in Figure 2.3, shown along with the impact of the image force effect. The image force effect reduces the thickness of the barrier and softens the edges of the barrier causing an increased tunneling current. The nonlinear voltage-current relation generates intermodulation products. Connectors often show irregular contact surfaces due to the material roughness, and in addition different oxidation levels due to corrosion at the microscopic contact point. These oxidation levels are changing with time. This PIM generating effect is commonly referred to as the *rusty bolt effect*.

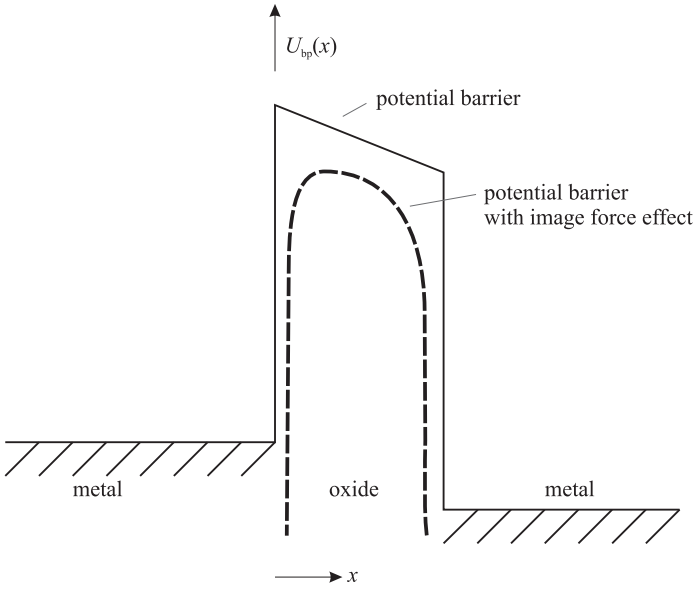

Figure 2.3: Barrier potential $U_{\mathrm{bp}}(x)$ for a metal-oxide-metal contact with image force effect.

2.4 Multi-Scale Modeling

One core issue in many multiphysics modeling tasks is the presence of multiple spatial and temporal scales that exhibit significant disparity and, yet, need to be resolved for the accurate quantitative analysis of the multiphysics phenomenon. MEMS devices are commonly a fraction of the bulk feature size which poses a challenge to any full wave electromagnetic (EM) analysis [57–59]. To resolve the small details of a MEMS device a finely resolved computational grid is required, resulting in a discrete problem of very high dimension.

Some examples for MEMS capacitors and switches [60–62] are presented in Figure 2.4. Frequently these devices are modeled in the mechanical and electrostatic domain. Figure 2.4(a) shows the schematic of a tunable MEMS capacitor. The separation d of two parallel plates is controlled by the voltage V applied between the plates, changing the balances of the Coulomb force and the retaining mechanical force due

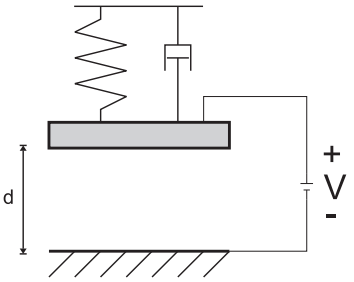

(a) Tunable parallel plate capacitor.

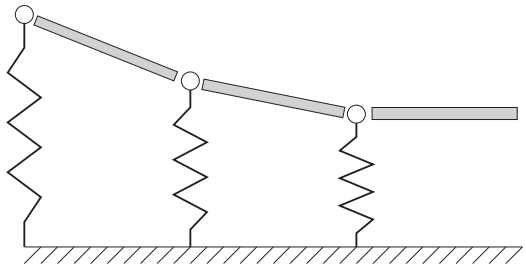

(b) Segmented-plate tunable capacitor.

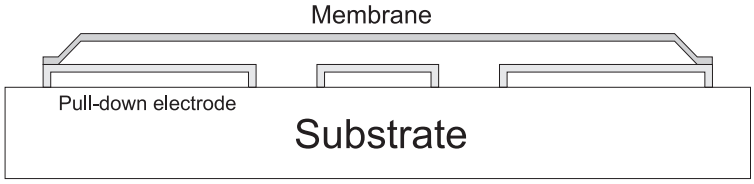

(c) CPW switch.

Figure 2.4: MEMS capacitor and switch devices.

to the spring. Hence, we obtain a change in the capacitance

$$C_{\mathrm{pl}}(V) = \frac{\epsilon A_{\mathrm{pl}}}{d(V)} \quad , \tag{2.22}$$

where A_{pl} is the plate surface. Concatenating several plate elements together to form a capacitor, as shown in Figure 2.4(b), with distinct properties of the spring support at the joints, allows for a linearization of the capacitance to voltage relation [61]. Figure 2.4(c) shows the schematic of a MEMS switch for a coplanar waveguide (CPW) [62]. The feature size for these devices is typically several hundred microns for the edge of a capacitor plate or of the plate of the switch. Operating those devices with signals in the range from some gigahertz to several tens of gigahertz would typical require a mesh size of at least several hundred microns for a full wave EM analysis and a finer mesh to resolve the lateral dimensions of the MEMS. However, the separation distance d is typically in the order of 1 μm. The large aspect ratio of the lateral extent and contact separation distance of MEMS devices proves to be a challenge. Thus we have to reduce the mesh size considerably in order to accurately model the

capacitor or switch in a full wave analysis.

A reduced mesh size increases the computational costs in terms of memory allocation and process time. Local mesh refinement can offset this problem by applying it only in regions where large field variations are anticipated, e.g., in the presence of sharp discontinuities [63]. At the interface between different grid sizings, spatial and temporal inter- or extrapolation schemes will be necessary.

Alternatively, different resolutions for certain areas of the computational domain can be achieved by means of the multiresolution time domain (MRTD) technique [64, 65]. This technique uses wavelets and a Galerkin-based approach to represent the fields in the computational cells. The MRTD methodology provides for a time-marching scheme and can be coupled with Yee's FDTD. Adaptive mesh refinement (AMR) allows for time variable resolution of the field within a computational cell by changing the number of wavelets [66]. We will present a methodology to relax the requirements for local subgriding in Chapter 4.

Challenges for multi-scale modeling occur not only with respect to different spatial scales but as well for different temporal scales. In the above mentioned examples of MEMS capacitors, for example, any mechanical motion will take place on a significantly longer timescale than any electromagnetic wave propagation phenomena. Often the process that evolves over the long time scale can be considered as static from the viewpoint of the fast process. However, the slow and the fast process may couple to each other such that a static approximation for the process at the long time scale is not appropriate. Modeling such a problem will require choosing a time interval long enough to account for the slow time scale and a temporal resolution fine enough to account for the fast scale. Hence, the computational cost of the problem scales proportionally to the ratio of long to short time scale. Possible long-term instabilities in the numerical solution algorithm add to the challenge. In Chapter 6 we

will address this problem using a multi-time approach for the solution of PDEs.

2.5 Modeling of Time-Varying Structures

Time-varying structures, like the above mentioned MEMS capacitors or switches, impose another challenge to full wave EM modeling. Full wave numerical modeling requires matching the discretization of the structure's boundary and interfaces and/or the entire space under investigation. Methods like the finite difference time domain (FDTD) method [20, 21], finite element method (FEM) [19] or transmission line matrix (TLM) method [22, 67] require a computational mesh over the entire domain to be modeled. To enforce the boundary conditions accurately it is important for the boundaries to coincide with the nodes of the mesh. As the structural elements of the device move during the course of the simulation, the conformity of the grid with the actual boundary is no longer given. Re-meshing of the computational grid and computing the electromagnetic field at the shifted node positions by interpolation is a common, though computationally costly, technique. In the re-meshing process a new mesh has to be generated and the fields known at the previous grid points have to be interpolated to determine the values at the node locations. The problem of moving boundaries has been addressed in the context of TLM in [68]. We will provide an approach to handle time-varying boundaries by using a time-dependent mapping approach for Maxwell's equations in Chapter 4.

Chapter 3

A Statistical Method for Modeling Multiphysics Phenomena in EM Waveguiding Structures

The very small ratio of received to transmitted power levels at base stations makes passive intermodulation-induced interference a serious liability on communication system performance. Because of this, there has been a renewed interest in the assessment of the impact of PIM on wireless communication system performance (see, for example, [69–72]) and in the investigation and quantification of the various PIM source mechanisms [73–76]. Nonlinear effects associated with the conduction properties of metal-to-metal contacts have been identified as one of the most important sources of PIM. An overview of the possible physical phenomena occurring in such contacts that may be responsible for PIM generation is provided in [50]. Among them, the temperature dependence of the contact resistance [77] and electron tunneling through very thin (in the order of nanometers) metal-oxide-metal films have received special attention, and macroscopic mathematical models have been proposed for their quantitative description [78, 79].

For the case of electron tunneling, the developed models have been used in support of experimental and theoretical quantification of PIM at metallic junctions [80, 81]. In these studies, voltage-current characteristics measurements under dc conditions as well as junction capacitance measurements have been used to develop circuit models describing the electron tunneling through the junction. The poor agreement (± 15 dB) between PIM power levels predicted by the generated circuit model, consisting of the series connection of a series resistance with the impedance formed by the parallel

combination of a nonlinear resistance with a linear capacitance, and those obtained through measurement, was attributed to the fact that the equivalent circuit did not include current crowding due to skin effect as well as the impact of contact surface roughness. However, no experimental studies which have linked the PIM power levels consistently to the skin effect have been presented so far.

The modeling methodology presented below aims at overcoming the aforementioned modeling shortcomings [82]. Toward this objective a distributed model is developed for the metal-oxide-metal contact, that allows for both surface roughness and skin effect to be taken into account. Because of the sub-micron thickness of the contact layer, the distributed model may be cast in terms of a distributed equivalent circuit. Such a representation makes the proposed PIM source model compatible with both nonlinear electromagnetic field solvers and general-purpose, network analysis oriented, nonlinear circuit simulators.

3.1 Modeling Methodology

Shown in Figure 3.1(a,b) is a schematic drawing of the electrical contact formed by two metal plates. The thickness of the actual contact layer is assumed to be at most 1 μm, much smaller than the transverse dimensions of the metal plates. For the purpose of this model, surface roughness is taken into account by allowing the distance between the plates to be variable. Thus, as the cross-sectional view of Figure 3.1(c) indicates, a rectangular saw-tooth profile is used to approximate the contact layer between the metal plates. For a planar contact along x and y, the saw-tooth profile is clearly two-dimensional. However, for the purposes of this study, and without loss of generality, we assume that the length of the metal contact (along x) is sufficiently larger than its width (along y) for the current flow in the metal plates to be predominantly along x.

This, for example, would be the case when the contact is formed between two metal strips oriented in the x-direction. Under this assumption, Figure 3.1(c) is interpreted as the longitudinal, cross-sectional view of the contact region between two metal plates of equal width w, exhibiting no geometry variation along their width.

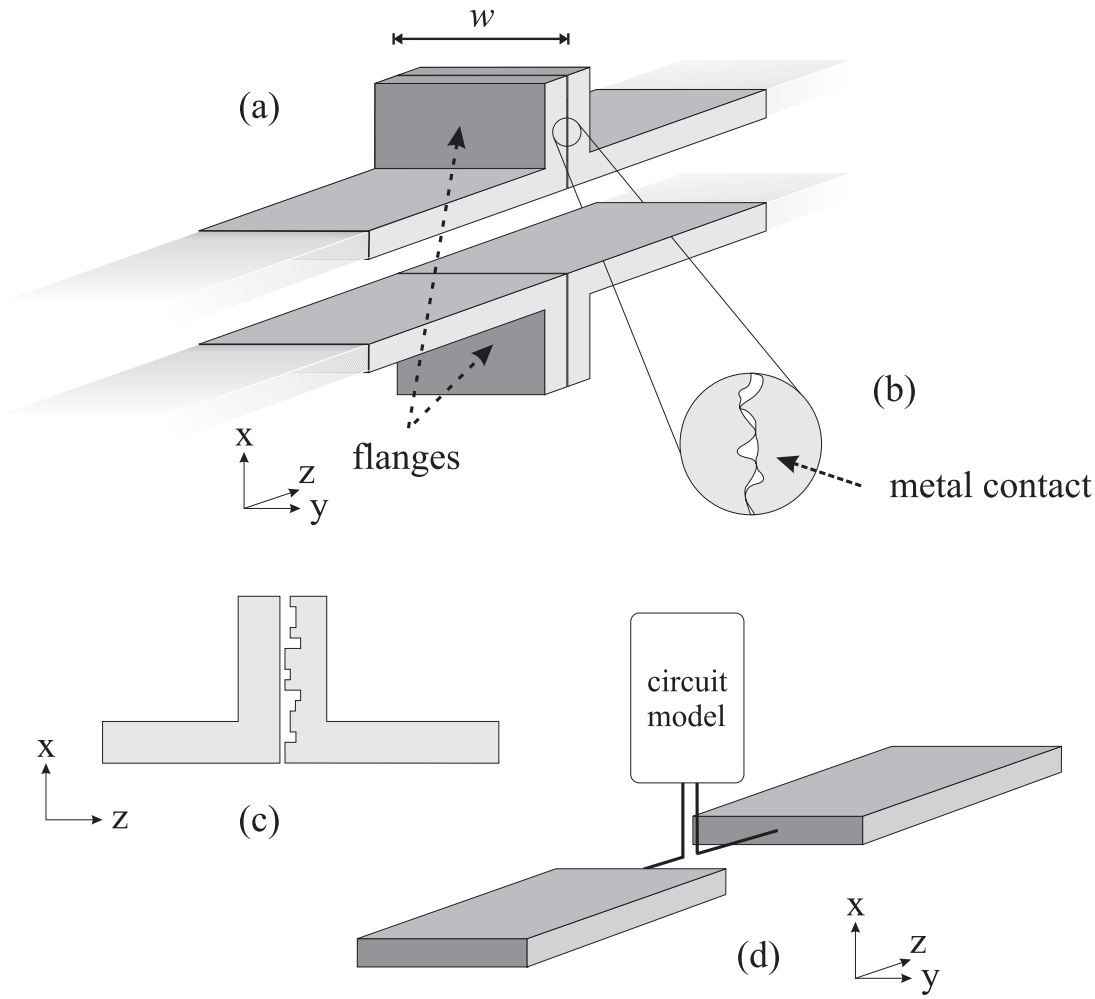

Figure 3.1: Contact model. (a) View of the contact between two metal plates formed by the flanges of a parallel plate waveguide. (b) The thin film contact layer between the metal plates is characterized by a surface roughness. (c) An approximate model of this surface roughness utilizes a rectangular saw-tooth profile with a position-dependent distance between the metal surfaces, shown for the upper part of the parallel plate waveguide. (d) Synthesized circuit model of the upper flange metal contact linked to the upper plate of the parallel plate waveguide.

In view of the above discussion, and for the special case of an x-directed current flow in the metal plates, it should be evident that the electromagnetic field distribution

between the metal plates is predominantly transverse magnetic (TM) to x. This, then, suggests that for each "parallel-plate" section of the approximate model depicted in Figure 3.1(c), a lumped circuit model can be developed consisting of a series impedance, $Z_s(\omega) = R_s(\omega) + j\omega L_s(\omega)$, which accounts for the frequency-dependent internal impedance of the metallization and the inductance of the (effective) loop formed by the current flow in the parallel plates, and a shunt admittance, $Y_p = G_p + j\omega C_p$, which accounts for the capacitance between the plates and the conduction loss in the oxide film. The computation of these elements is discussed later in the section. The final model for the metal contact, derived in the following, is linked to the waveguide as shown in the schematic of Figure 3.1(d).

If the separation between the metal plates is in the order of a few tens of angstroms, then electron tunneling is possible through the oxide film. For a potential $V < \varphi_0/e$ between the plates, the tunneling current density is given by [78]

$$J(V) = \frac{e}{2\pi h s_{\text{ox}}^2}\left\{\left(\varphi_0 - \frac{eV}{2}\right)\exp\left[-\frac{4\pi s_{\text{ox}}}{h}\sqrt{2m\left(\varphi_0 - \frac{eV}{2}\right)}\right] - \left(\varphi_0 + \frac{eV}{2}\right)\exp\left[-\frac{4\pi s_{\text{ox}}}{h}\sqrt{2m_{\text{e}}\left(\varphi_0 + \frac{eV}{2}\right)}\right]\right\}, \quad (3.1)$$

where φ_0 is the work function of the metal, m_{e} is the mass of electron, e the charge of electron, h is Planck's constant and s_{ox} the thickness of the oxide film. This equation is based on the Wentzel-Kramers-Brillouin-Jeffreys (WKBJ) approximation to the one-dimensional Schrödinger equation [83, 84]; hence it does not take into account the two-dimensional potential barrier at the edges of the parallel plates. A voltage-dependent current source is introduced between the plates to model the relation in (3.1). Following [81], or by a polynomial approximation to (3.1), the source exhibits the $I - V$ characteristics

$$I(V) = g_1 V + g_3 V^3, \quad (3.2)$$

with the values of the constants g_1 and g_3 being dictated by the metallization material, the thickness of the film and the area of the contact [79]. Thus, the general model of the equivalent lumped circuit used for the modeling of a longitudinal (x-directed) section of the rectangular, saw-tooth contact geometry approximation of Figure 3.1(c) is as shown in Figure 3.2(a). The electrical model for the contact is obtained through the concatenation of the models for all longitudinal sections. The resulting model is depicted in Figure 3.2(b). The extension of this model to the general case where current flow in the contact is along both transverse directions x and y is straightforward with the model of Figure 3.2(a) replaced by its two-dimensional version depicted in Figure 3.2(c).

Because of the transverse magnetic attribute of the electromagnetic fields in the contact layer, the calculation of $Z_s(\omega)$ and Y_p can be effected through the application of quasi-static field solvers. For example, for the one-dimensional current flow situation depicted in Figure 3.1, the methodology used in [85] is employed for their calculation, given the width and thickness of the metal plates, their separation and the metallization and oxide properties. Since Z_s is frequency-dependent, the magneto-quasi-static solver discussed in [85] is used to calculate their values for a number of frequency points over the frequency bandwidth of interest. Subsequently, the calculated values are used to generate rational function approximations of these quantities, which, in turn, lend themselves to the direct synthesis of equivalent circuits of constant (frequency-independent) elements that exhibit the same impedance behavior over the bandwidth of interest.

More specifically, using the methodology described in [86], a rational fit of its calculated values at discrete frequencies over the bandwidth of interest yields the

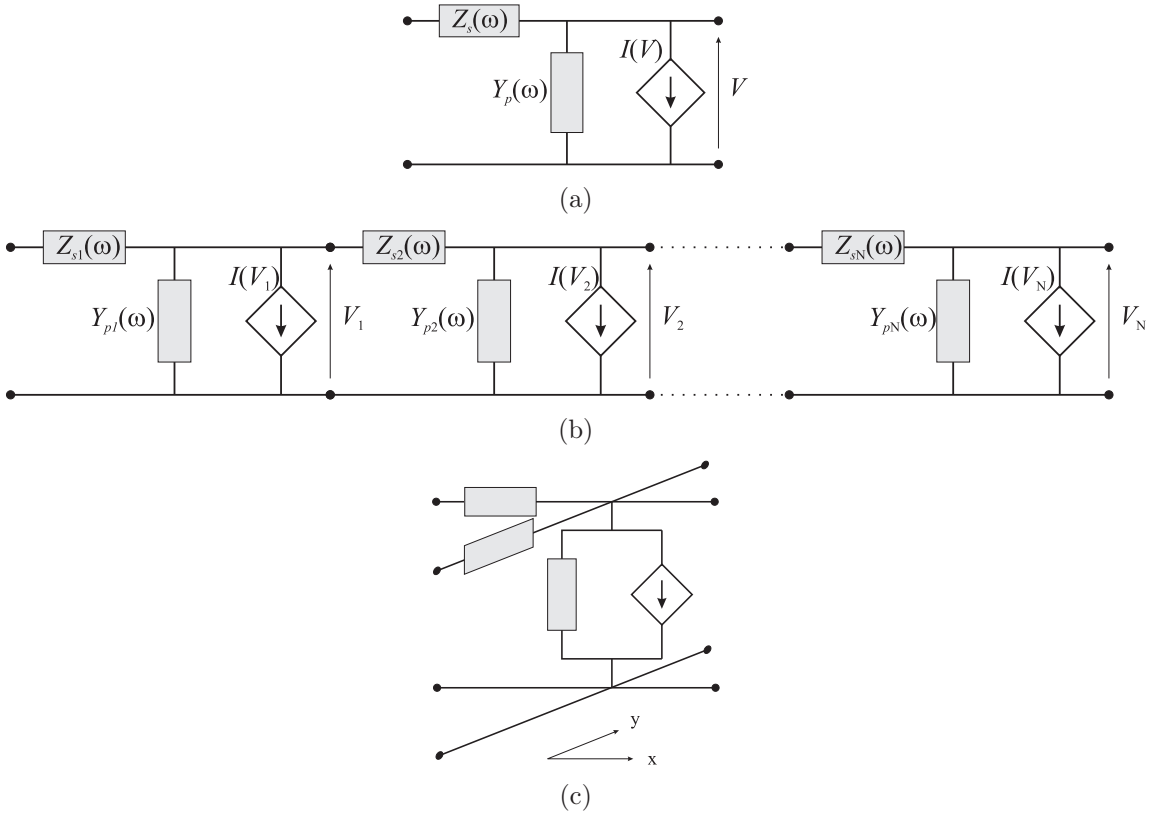

Figure 3.2: Circuit equivalent model. (a) Lumped element circuit equivalent for a single, parallel-plate section under the assumption of one-dimensional current flow. (b) Overall distributed-circuit model for metal-to-metal contact under the assumption of one-dimensional current flow. (c) Lumped circuit for a single, parallel-plate section for the general case of two-dimensional current flow.

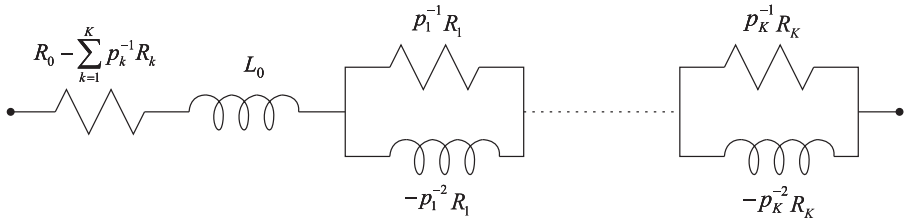

Figure 3.3: Synthesized impedance of the equivalent circuit.

following closed-form expression for its approximation:

$$Z_s(s) \approx R_0 + sL_0 + \sum_{k=1}^{K} \frac{R_k}{s - p_k}\,, \tag{3.3}$$

where $s = j\omega$. The circuit representation of the synthesized impedance is depicted in Figure 3.3. Use of this synthesized equivalent circuit in place of the series impedances in the distributed circuit model of Figure 3.2(b) results in a circuit netlist that is readily compatible with all popular nonlinear circuit simulators.

3.2 Simulation Studies

For the purposes of this numerical study the plate width was taken to be 10 μm and the plate thickness 1 μm. The total length of the contact was 1 cm (in the x direction) as shown in Figure 3.1(c). To account for the roughness the metal contact is subdivided into 50 segments along the x-direction. The length of each segment varied between 0.01 cm and 0.03 cm. For each segment the plate separation was assigned a value in the range [10 Å$-$1 μm]. The material in the gap was randomly assigned to be either air, or metal oxide, or a lossy dielectric to model the contact and corrosion profile. With the metallization taken to be aluminium, the following resistivity values were used: $\rho_{\text{Al}} = 2.65 \times 10^{-8}$ Ωm, $\rho_{\text{oxide}} = 1 \times 10^{-14}$ Ωm [87]. The loss tangent of the dielectric was taken to be $\tan\delta = 0.001$. Segment length, metal separation (gap size), and gap filling are randomly chosen for each segment from a discrete set of

values in the ranges mentioned above. The probability distribution for each set of values is uniform. For each segment the equivalent circuit was developed using the methodology described in the previous section. The frequency bandwidth over which the circuit of Figure 3.3 was synthesized was 5 GHz. Through concatenation of the equivalent circuit for each segment, the circuit representation of Figure 3.2 was established for the contact. The third order polynomials for the controlled current sources present in the model were extracted from (3.1) for an oxide film with a work function $\varphi_0 = 3$ eV.

A set of 1000 roughness profiles were generated and used for our simulations. Each equivalent circuit is driven by a voltage source V_{in} with input signal

$$V_{in} = \sin(2\pi f_1 t) + \sin(2\pi f_2 t)\,. \tag{3.4}$$

The three pairs of frequencies used for the simulations were ($f_1 = 100$ MHz, $f_2 = 110$ MHz), ($f_1 = 300$ MHz, $f_2 = 330$ MHz), and ($f_1 = 1$ GHz, $f_2 = 1.05$ GHz). All transient simulations were carried out using SPICE. Plotted in Figures 3.4(a) - 3.4(c), are the spectra of the calculated current at the voltage source for the three pairs of frequencies for a single contact with random roughness profile. The spectra of the other samples differ according to the strength of their intermodulation frequencies (IMF). Around 19% of the samples show hardly any PIM due to the lack of thin oxide layers < 20 Å in their random profile. Table 3.1 quantifies the expectation value $\overline{\mu}_p = \langle P_{\mathrm{IMF}} \rangle$ and the standard deviation $\sigma_p = \sqrt{\langle (P_{\mathrm{IMF}} - \overline{\mu}_p)^2 \rangle}$ of the spectral power P_{IMF} at various IMFs for the remaining sets of contact roughness profiles [88]. The impact of the frequency-dependence on the skin effect at different frequencies is clearly evident. Correlating the intermodulation levels with various parameters by

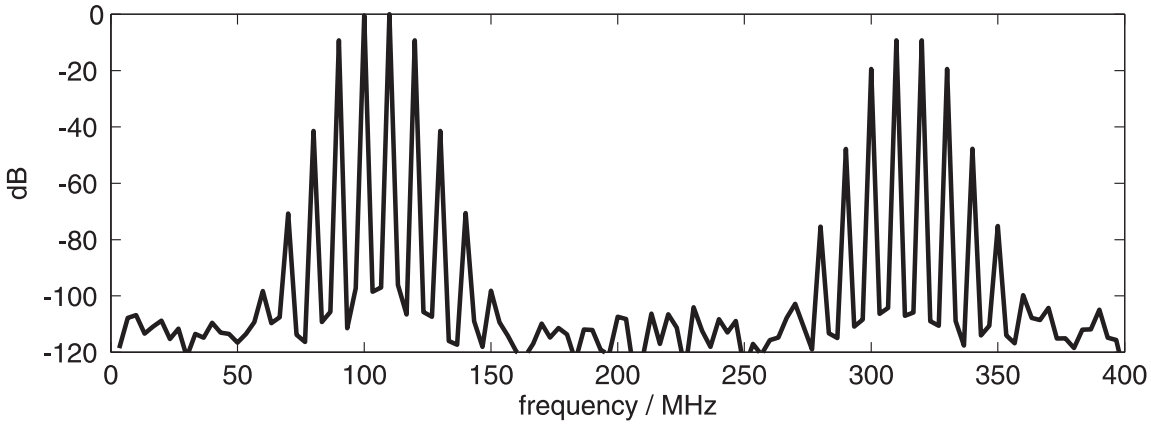

(a) $f_1 = 100$ MHz, $f_2 = 110$ MHz

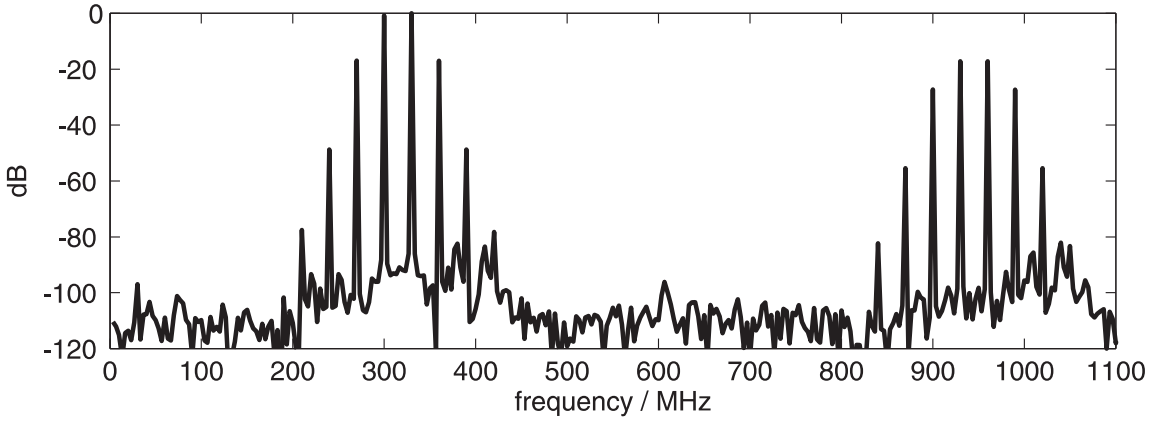

(b) $f_1 = 300$ MHz, $f_2 = 330$ MHz

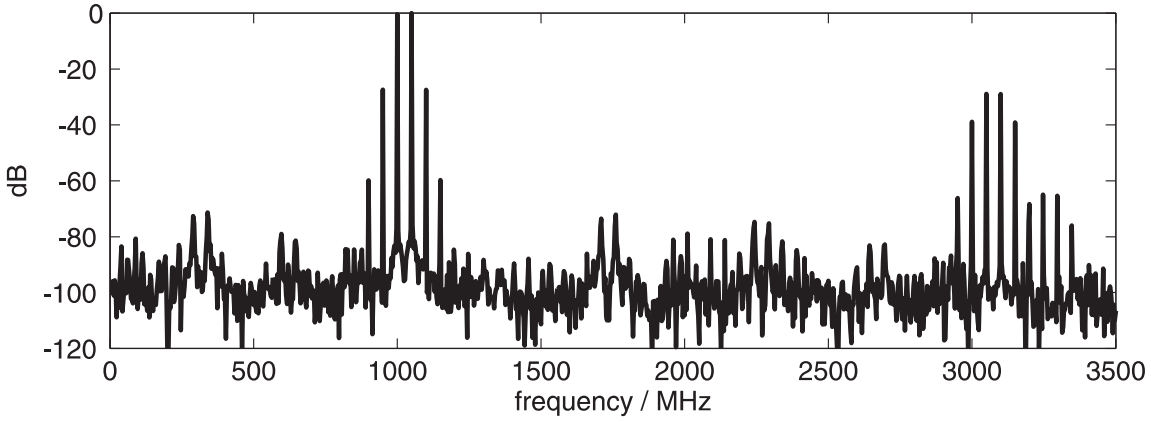

(c) $f_1 = 1$ GHz,$f_2 = 1.05$ GHz

Figure 3.4: Spectrum of the input current I_{in}.

Table 3.1: Average spectral power $\overline{\mu}_p$ and its standard deviation σ_p for the intermodulation products

IMF	$2f_1-f_2$	$2f_2-f_1$	$3f_1$	f_2+2f_1	f_1+2f_2	$3f_2$
	($f_1 = 100$ MHz, $f_2 = 110$ MHz)					
MHz	90	120	300	310	320	330
$\overline{\mu}_p$ / dB	-8.24	-7.74	-20.12	-6.64	-6.63	-20.11
σ_p / dB	2.25	2.20	3.77	3.37	3.40	3.90
	($f_1 = 300$ MHz, $f_2 = 330$ MHz)					
MHz	270	360	900	930	960	990
$\overline{\mu}_p$ / dB	-14.06	-13.86	-27.63	-14.14	-14.21	-27.88
σ_p / dB	3.94	3.98	4.13	4.15	4.16	4.17
	($f_1 = 1$ GHz, $f_2 = 1.05$ GHz)					
GHz	0.95	1.10	3.00	3.05	3.10	3.15
$\overline{\mu}_p$ / dB	-24.23	-24.58	-40.00	-28.60	-28.78	-40.46
σ_p / dB	4.98	5.02	4.98	5.51	5.54	5.14

[88, 89]

$$r = \frac{\langle P_{\mathrm{IMF}} X\rangle - \langle P_{\mathrm{IMF}}\rangle\langle X\rangle}{\sqrt{\langle P_{\mathrm{IMF}}^2\rangle - \langle P_{\mathrm{IMF}}\rangle^2}\sqrt{\langle X^2\rangle - \langle X\rangle^2}}\,, \tag{3.5}$$

where r is the correlation coefficient and X is the chosen parameter, allows for further investigation of dependencies. As shown in Figure 3.5, correlation between the intermodulation level (IML) and the percentage of the contact's gap filling with oxide is negligible. However, stronger correlation is found between the IML and the distance from the voltage source to the first oxide filled gap of size 10 Å as shown in Figure 3.6.

3.3 Conclusion

In summary, a modeling methodology has been presented for the phenomenological and quantitative analysis of electron tunneling at metallic contacts as a source of passive intermodulation. As demonstrated by the studies presented above, the proposed model provides for the impact of contact surface roughness and the frequency dependence of the skin effect field distribution in the metallization to be taken into account in the quantification of the generated intermodulation interference. The PIM

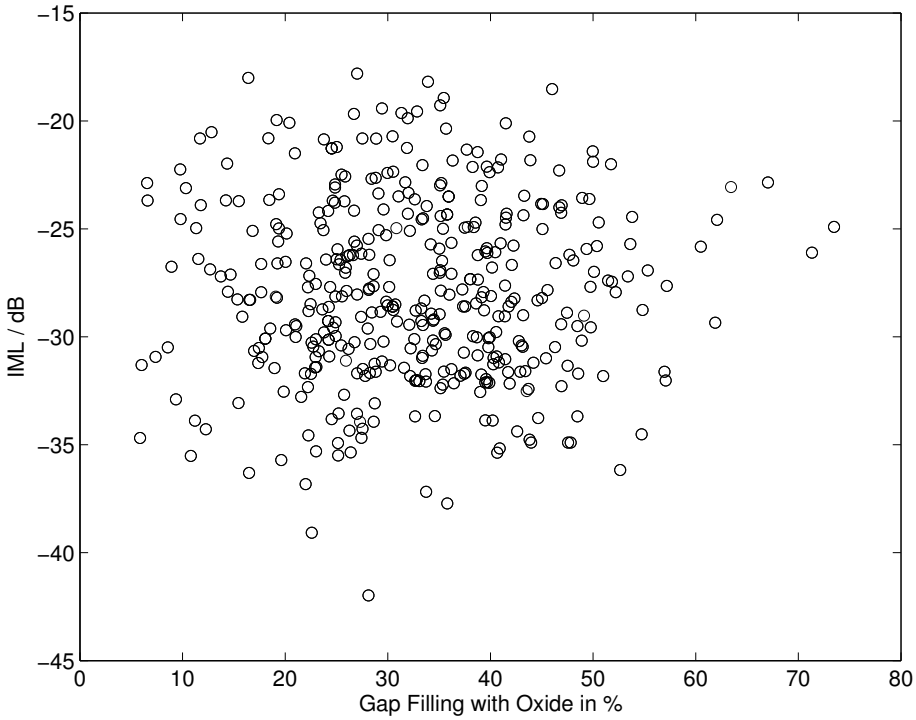

Figure 3.5: IML vs. filling of the gap with oxide, $f_1 = 300$ MHz, $f_2 = 330$ MHz, IMF: 990 MHz, $r = 0.015$

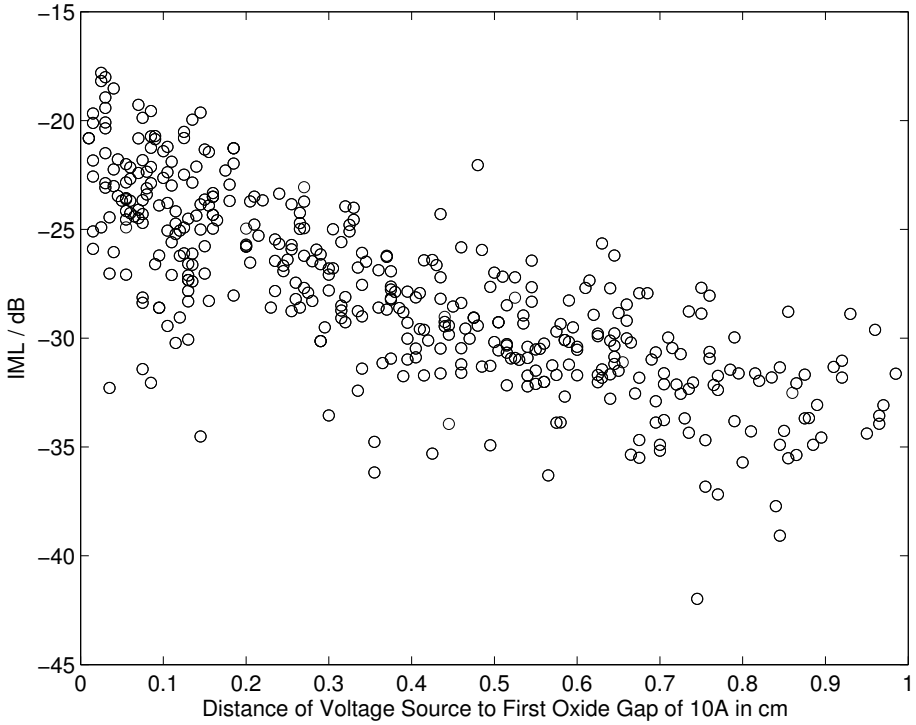

Figure 3.6: IML vs. distance of the first oxide gap of 10 Å measured from the input voltage source, $f_1 = 300$ MHz, $f_2 = 330$ MHz, IMF: 990 MHz, $r = 0.778$

dropped significantly when the smallest gap sizes were larger than 20 Å. Choosing samples with gaps < 20 Å, in which case we observe PIM, allows one to perform a predictive quantitative analysis of how other parameters of the structure impact the PIM levels.

The generated model is cast in terms of a distributed circuit netlist. Thus, it is compatible with both general-purpose, transient electromagnetic field solvers and network analysis-oriented, non-linear circuit simulators. This compatibility facilitates the incorporation of the model in system-level simulations aimed at intermodulation interference assessment at the system level.

Chapter 4

Modeling Curved and Moving Boundaries with a Lagrangian Mapping (LM) Method

The success of the FDTD method and its attractiveness are in major part due to the simplicity of the so-called Yee's scheme for the spatial discretization of the curl operators on two staggered Cartesian grids [20, 21]. It is because of its simplicity that the utilization of a Cartesian grid remains the most attractive in the application of the method to the modeling of electromagnetic field and wave propagation in domains involving arbitrarily shaped, non-Cartesian material boundaries. Despite significant advances in avoiding the modeling error resulting from the staircase approximation of a curved material boundary [90–95], the simplicity of the Yee's Cartesian lattice frequently leads to its adoption at the cost of utilizing a finer grid in order to minimize the modeling error [96].

The aforementioned advanced techniques for improving modeling fidelity without increasing the spatial sampling of the fields come at the cost of increased complexity in both mesh generation and in the development of the discrete forms of the curl operators.

A topic of significant interest for various engineering applications is electromagnetic wave interactions with moving objects. Important examples include electromagnetic wave scattering by moving and/or rotating objects and electromagnetic wave interactions with structures with time-varying boundaries. The latter class is of practical interest due to its relevance for the analysis of phenomena such as the motion-induced tuning of the pass-bands or stop-bands of electromagnetic filters. The

theory of electromagnetic waves interacting with moving objects is well-documented in the literature [97, 98], along with its application to the solution of a limited class of problems for which analytical solutions can be obtained [99, 100].

For the general case of structures and scatterers of arbitrary geometric shape and material composition, numerical techniques must be implemented for the solution of the governing equations. The FDTD method was one of the first methods used to model transient electromagnetic wave scattering by moving targets [101]. One of the problems in the application of the FDTD method for the modeling of electromagnetic wave interactions with geometries that involve moving boundaries is the need for on-the-fly re-meshing of the computational domain to accommodate the changing position of the moving boundary.

In this chapter we present an alternative to the above mentioned techniques, which is based on the application of Lagrangian techniques for solving problems in mechanics and coupled electro-mechanical problems [102, 103]. The basic idea of the method is to map the physical domain onto a reference domain with all its boundaries parallel to the planes of a reference Cartesian coordinate system. Once such a domain can be defined, the mapped version of Maxwell's curl equations are cast in a form that lends itself to their direct discretization using Yee's staggered Cartesian grids on the reference domain. The mapping is time dependent and accommodates moving boundaries. The attributes of such an approach were demonstrated in [104–106].

Use of coordinate transformation for the numerical solution of Maxwell's equations on non-orthogonal grids has been explored in the past, most recently in the context of metamaterials [107]. The approach proposed here attempts to relax the complexity of [107] in order to provide for an efficient means for handling time-varying and/or moving boundaries in the electromagnetic boundary value problems of interest.

4.1 The LM Methodology

In this section we present the development of the equivalent boundary value problem over a domain with fixed boundaries, based on a Lagrangian approach. To introduce the concept of the Lagrangian approach it is useful to consider problems in mechanics where the Lagrangian concept is frequently used. Figure 4.1 depicts the reference

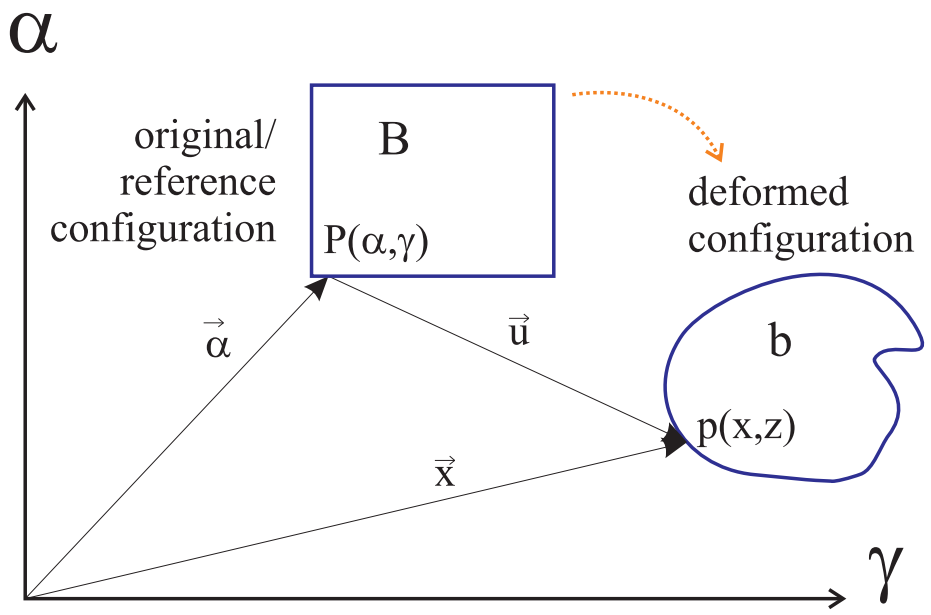

Figure 4.1: Reference and deformed configuration.

configuration B and the deformed configuration b of one body. We find the particle $P(\alpha, \gamma)$ displaced to $p(x, z)$ where $\boldsymbol{x} = \boldsymbol{\alpha} + \boldsymbol{u}$ and $\boldsymbol{u}$ is the displacement vector. There are two different approaches that are commonly taken in mechanics to formulate a mathematical model describing moving particles [102, 108]. The first approach describes a particle position as a function of its position at an initial reference configuration and its time evolution. The second approach focuses on a fixed position in space and the evolution of physical quantities at this point. The latter suggests a Lagrangian approach, as we find it, for example, in fluid dynamics, where the knowledge of the pressure at some point tends to be more valuable than the actual position of each of the fluid's particles. The Lagrangian approach allows for a mapping such that

we solve for the quantities of interest at fixed locations in the reference configuration.

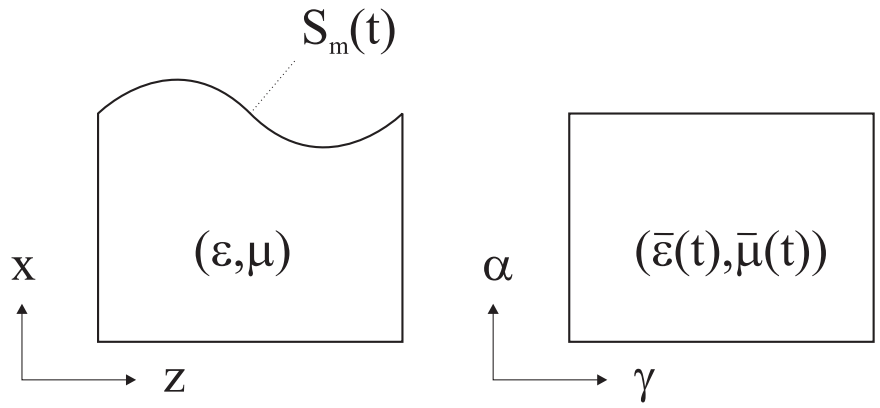

(a) Deformed configuration. (b) Reference configuration.

Figure 4.2: Non-uniform (deformed) domain at time t and uniform (Cartesian) reference domain.

Toward this, use is made of the computational domain depicted in Figure 4.2(a). While Figure 4.2(a) depicts a two-dimensional domain, we assume that the actual domain is three-dimensional with $x - z$ cross-sectional geometry as depicted in the figure. Furthermore, for the sake of simplicity and without loss of generality it is assumed that only the top boundary is moving and, thus, it is changing with time, as depicted in the figure.

Figure 4.2(b) denotes a rectangular domain (parallelepiped) that will be referred to in the following as the reference domain. Let $(\hat{\alpha}, \hat{\beta}, \hat{\gamma})$ denote the unit vectors along the three axes of the Cartesian coordinate system in the reference domain. We can consider the physical domain of Figure 4.2(a) at time t as the map of the reference domain. The map between the two domains is effected numerically through a quasi-elastic finite element solver [109]. Under such a mapping, every grid point $P(\alpha, \beta, \gamma)$ on a rectangular grid over the reference domain is mapped onto a point $p(x, y, z)$ of

the physical domain at time t. This relationship is cast in the form

$$d \begin{pmatrix} x \\ y \\ z \end{pmatrix} = \mathcal{F}(t) d \begin{pmatrix} \alpha \\ \beta \\ \gamma \end{pmatrix}, \tag{4.1}$$

where the deformation gradient matrix, $\mathcal{F}(t)$, is given by

$$\mathcal{F}(t) = \begin{bmatrix} \frac{\partial x}{\partial \alpha} & \frac{\partial x}{\partial \beta} & \frac{\partial x}{\partial \gamma} \\ \frac{\partial y}{\partial \alpha} & \frac{\partial y}{\partial \beta} & \frac{\partial y}{\partial \gamma} \\ \frac{\partial z}{\partial \alpha} & \frac{\partial z}{\partial \beta} & \frac{\partial z}{\partial \gamma} \end{bmatrix}. \tag{4.2}$$

Furthermore, the mapping between vector quantities in the two domains is given by

$$\begin{pmatrix} A_x \\ A_y \\ A_z \end{pmatrix} = \mathcal{G}(t) \begin{pmatrix} A_\alpha \\ A_\beta \\ A_\gamma \end{pmatrix}, \tag{4.3}$$

where the matrix $\mathcal{G}(t)$ is given by

$$\mathcal{G}(t) = \begin{bmatrix} \frac{\partial \alpha}{\partial x(t)} & \frac{\partial \beta}{\partial x(t)} & \frac{\partial \gamma}{\partial x(t)} \\ \frac{\partial \alpha}{\partial y(t)} & \frac{\partial \beta}{\partial y(t)} & \frac{\partial \gamma}{\partial y(t)} \\ \frac{\partial \alpha}{\partial z(t)} & \frac{\partial \beta}{\partial z(t)} & \frac{\partial \gamma}{\partial z(t)} \end{bmatrix}. \tag{4.4}$$

In addition, we need to derive the pertinent equations for the mapping of the first-order spatial derivatives present in the curl operator. Toward this, it is useful to

define the following Jacobian determinant:

$$\begin{aligned} D_{x_1x_2}^{\alpha_1\alpha_2}(t) &:= \frac{\partial(\alpha_1,\alpha_2)}{\partial(x_1(t),x_2(t))} \\ &:= \det \begin{bmatrix} \frac{\partial \alpha_1}{\partial x_1(t)} & \frac{\partial \alpha_1}{\partial x_2(t)} \\ \frac{\partial \alpha_2}{\partial x_1(t)} & \frac{\partial \alpha_2}{\partial x_2(t)} \end{bmatrix}, \end{aligned} \tag{4.5}$$

where α_1, α_2 assume values from the set $\{\alpha, \beta, \gamma\}$, while x_1, x_2 assume values from the set $\{x, y, z\}$. We define the matrix $\tilde{\mathcal{D}}$ as

$$\tilde{\mathcal{D}}(t) = \begin{bmatrix} D_{yz}^{\beta\gamma}(t) & -D_{yz}^{\alpha\gamma}(t) & D_{yz}^{\alpha\beta}(t) \\ -D_{xz}^{\beta\gamma}(t) & D_{xz}^{\alpha\gamma}(t) & -D_{xz}^{\alpha\beta}(t) \\ D_{xy}^{\beta\gamma}(t) & -D_{xy}^{\alpha\gamma}(t) & D_{xy}^{\alpha\beta}(t) \end{bmatrix}. \tag{4.6}$$

Using the above definitions the mapped form of Faraday's law from the deformed (physical) domain

$$\frac{\partial}{\partial t}\boldsymbol{E} = \frac{1}{\epsilon}\nabla \times \boldsymbol{H} \tag{4.7}$$

onto the reference Cartesian domain is given by

$$\frac{\partial}{\partial t}\tilde{\boldsymbol{E}} = \frac{1}{\epsilon}\mathcal{G}^{-1}(t)\tilde{\mathcal{D}}(t)\nabla \times \tilde{\boldsymbol{H}}\,, \tag{4.8}$$

where the $\tilde{}$ is used to denote the vector in the reference domain, i.e. $\tilde{\boldsymbol{E}} \equiv \tilde{\boldsymbol{E}}(\alpha, \beta, \gamma, t)$, $\tilde{\boldsymbol{H}} \equiv \tilde{\boldsymbol{H}}(\alpha, \beta, \gamma, t)$. The mapped form of Ampère's law in a source-free region is given by

$$\frac{\partial}{\partial t}\tilde{\boldsymbol{H}} = -\frac{1}{\mu}\mathcal{G}^{-1}(t)\tilde{\mathcal{D}}(t)\nabla \times \tilde{\boldsymbol{E}}\,. \tag{4.9}$$

Thus, Maxwell's equations in the reference domain can be written

$$\frac{\partial}{\partial t}\tilde{\boldsymbol{E}} = \frac{1}{\epsilon}\tilde{\nabla}(t) \times \tilde{\boldsymbol{H}}\,, \tag{4.10}$$

$$\frac{\partial}{\partial t}\tilde{\boldsymbol{H}} = -\frac{1}{\mu}\tilde{\nabla}(t) \times \tilde{\boldsymbol{E}}\,, \tag{4.11}$$

where the modified operator $\tilde{\nabla}$ is defined as

$$\tilde{\nabla}(t)\times \equiv \mathcal{G}^{-1}(t)\tilde{\mathcal{D}}(t)\nabla \times\ . \tag{4.12}$$

For the case of a curved but static boundary, i.e. if there is no time dependence for $\mathcal{G}$ and $\tilde{\mathcal{D}}$, the modified system of Maxwell's equations on the reference domain with fixed boundaries can be interpreted in terms of an anisotropic medium with the following electric permittivity and magnetic permeability tensors:

$$\bar{\epsilon} = \tilde{\mathcal{D}}^{-1}\mathcal{G}\epsilon\,, \tag{4.13}$$

$$\bar{\mu} = \tilde{\mathcal{D}}^{-1}\mathcal{G}\mu\,. \tag{4.14}$$

In this case no modifications are done to the nabla operator. A brief derivation of the mapped form of Maxwell's equations is given in Appendix A.

4.2 Implementation of the LM Method in FDTD

Since we are interested in utilizing the standard Yee's lattice for the discretization of the curl operators in Maxwell's equations, the preferred choice for the reference domain is one with its boundaries parallel to the planes of the reference Cartesian coordinate system. Let us assume that a reference Cartesian domain has been established and a uniform Cartesian grid is used to provide for its discretization. With

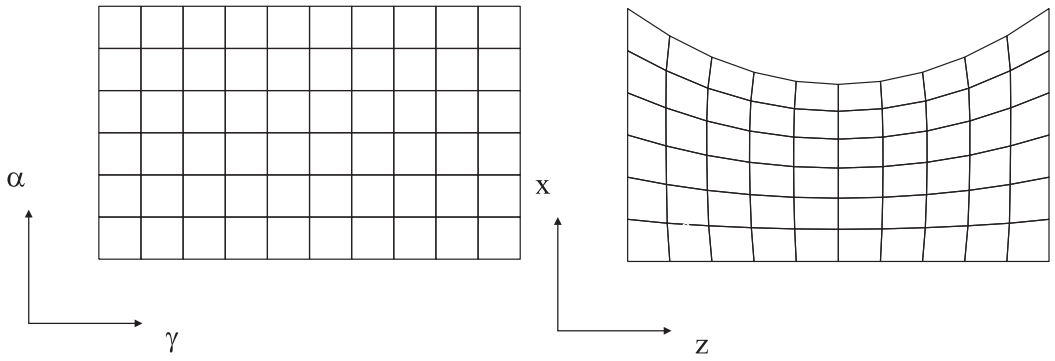

(a) Reference configuration. (b) Deformed configuration.

Figure 4.3: Uniform (Cartesian) and non-uniform (deformed) grids for reference and deformed configuration, respectively.

reference to Figure 4.3, in the spirit of the Lagrangian approach, in order to simplify the modeling of electromagnetic wave interactions inside the domain with the curved top boundary on the right we displace, by analogy to the moving particle problem in mechanics, the grid points on the boundaries of the uniform grid in the reference domain until they coincide with the curved boundary on the domain on the right. Thinking of the reference domain as an elastic membrane, the displacement of the boundary grid points will result in displacement of the remaining grid points of the uniform grid. Thus, a deformed grid results over the deformed domain. The definition of a mapping between the deformed grid and the reference grid allows us, through the use of the Lagrangian formulation, to apply the spatial discretization of the curl operators in Maxwell's equations over the Cartesian grid of the reference domain. The key difference is that the discretization is applied to a modified version of Maxwell's equations, the form of which is governed by the mapping between the two domains. Furthermore, all boundary conditions at the material boundaries on the physical (deformed) domain can be enforced in a much simpler manner on the corresponding maps of the curved boundaries on the reference domain.

4.2.1 The two-dimensional case

To demonstrate the discrete form of the Lagrangian form of Maxwell's equations in the context of the FDTD method, we first consider the two-dimensional case where the geometry and the field excitation are invariant in the $\hat{y}$ direction; hence, $\hat{\beta} \equiv \hat{y}$. This results in two possible field polarizations, namely, the transverse electric (TE) and the transverse magnetic (TM). For the TM polarization it is $E_y = 0$, $H_x = 0$ and $H_z = 0$. Furthermore, because of the two-dimensional nature of the problem, it is $\frac{\partial \alpha}{\partial y} = \frac{\partial \gamma}{\partial y} = 0$ and $\frac{\partial \beta}{\partial y} = 1$. Making use of these relations in (4.4) and (4.6) results in the following reduced forms of (4.8)–(4.9):

$$\frac{\partial H_\beta}{\partial t} = -\frac{1}{\mu} \det \begin{bmatrix} \frac{\partial \alpha}{\partial x(t)} & \frac{\partial \gamma}{\partial x(t)} \\ \frac{\partial \alpha}{\partial z(t)} & \frac{\partial \gamma}{\partial z(t)} \end{bmatrix} \left(\frac{\partial E_\alpha}{\partial \gamma} - \frac{\partial E_\gamma}{\partial \alpha} \right) := \frac{1}{\mu} \mathcal{H}(t) \left(\frac{\partial E_\alpha}{\partial \gamma} - \frac{\partial E_\gamma}{\partial \alpha} \right), \tag{4.15}$$

$$\frac{\partial}{\partial t} \begin{pmatrix} E_\alpha \\ E_\gamma \end{pmatrix} = \frac{1}{\epsilon} \begin{bmatrix} \frac{\partial \alpha}{\partial x(t)} & \frac{\partial \gamma}{\partial x(t)} \\ \frac{\partial \alpha}{\partial z(t)} & \frac{\partial \gamma}{\partial z(t)} \end{bmatrix}^{-1} \begin{bmatrix} \frac{\partial \gamma}{\partial z(t)} & -\frac{\partial \alpha}{\partial z(t)} \\ -\frac{\partial \gamma}{\partial x(t)} & \frac{\partial \alpha}{\partial x(t)} \end{bmatrix} \begin{pmatrix} -\frac{\partial H_\beta}{\partial \gamma} \\ \frac{\partial H_\beta}{\alpha} \end{pmatrix} := \frac{1}{\epsilon} \mathcal{I}(t) \begin{pmatrix} -\frac{\partial H_\beta}{\partial \gamma} \\ \frac{\partial H_\beta}{\alpha} \end{pmatrix}. \tag{4.16}$$

The above equations are discretized on Yee's staggered grid as shown in Figure 4.4 where the electric field quantities E_α and E_γ are shown as arrows and the H_β field, which is protruding out of the plane, is depicted by dotted circles. More specifically, we denote $E_\alpha|^n_{i,k} = E_\alpha((i - \frac{1}{2})\Delta\alpha, (k-1)\Delta\gamma, n\Delta t)$, $E_\gamma|^n_{i,k} = E_\gamma((i-1)\Delta\alpha, (k - \frac{1}{2})\Delta\gamma, n\Delta t)$ and $H_\beta|^n_{i,k} = H_\beta((i - \frac{1}{2})\Delta\alpha, (k - \frac{1}{2})\Delta\gamma, n\Delta t)$. $\Delta\alpha$ and $\Delta\gamma$ represent the grid spacing, while Δt represents the discrete time step. Furthermore, $\mathcal{H}|_{i,k}$ denotes the determinant of (4.15) evaluated at the position of the E field component associated with it in the same equation. In a similar manner, $\mathcal{I}|_{i,k}$ denotes the matrix of (4.16) evaluated at the position of $H_\beta|_{i,k}$, with $\mathcal{I}|_{i,k}(q,r)$ specifying the (q,r) element of

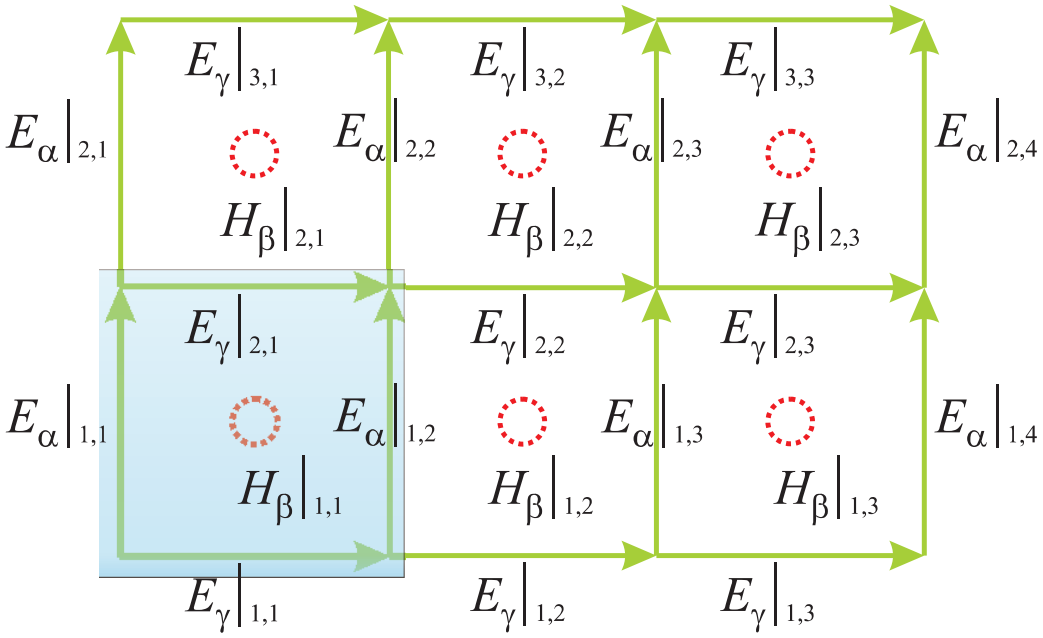

Figure 4.4: Yee's staggered grid on the Cartesian reference domain.

the matrix. This yields the following discrete form of the Lagrangian formulation of Maxwell's curl equations:

$$H_\beta|_{i,k}^{n+1/2} = H_\beta|_{i,k}^{n-1/2} + \frac{\Delta t}{\mu}\mathcal{H}|_{i,k}^{n+1/2}\left(\frac{E_\gamma|_{i+1,k}^{n} - E_\gamma|_{i,k}^{n}}{\Delta\alpha} - \frac{E_\alpha|_{i,k+1}^{n} - E_\alpha|_{i,k}^{n}}{\Delta\gamma}\right), \tag{4.17}$$

$$\begin{aligned} E_\alpha|_{i,k}^{n+1} = E_\alpha|_{i,k}^{n} + \frac{\Delta t}{\epsilon}\Bigg(&- \mathcal{I}|_{i,k}^{n+1}(1,1)\frac{H_\beta|_{i,k}^{n+1/2} - H_\beta|_{i,k-1}^{n+1/2}}{\Delta\gamma} + \mathcal{I}|_{i,k}^{n+1}(1,2)\times \\ &\times \frac{H_\beta|_{i+1,k-1}^{n+1/2} - H_\beta|_{i-1,k-1}^{n+1/2} + H_\beta|_{i+1,k}^{n+1/2} - H_\beta|_{i-1,k}^{n+1/2}}{4\Delta\alpha}\Bigg) \end{aligned}, \tag{4.18}$$

$$\begin{aligned} E_\gamma|_{i,k}^{n+1} = E_\gamma|_{i,k}^{n} + \frac{\Delta t}{\epsilon}\Bigg(&- \mathcal{I}|_{i,k}^{n+1}(2,1)\Bigg(\frac{H_\beta|_{i-1,k+1}^{n+1/2} - H_\beta|_{i-1,k-1}^{n+1/2}}{4\Delta\gamma} + \\ &+ \frac{H_\beta|_{i,k+1}^{n+1/2} - H_\beta|_{i,k-1}^{n+1/2}}{4\Delta\gamma}\Bigg) + \mathcal{I}|_{i,k}^{n+1}(2,2)\frac{H_\beta|_{i,k}^{n+1/2} - H_\beta|_{i-1,k}^{n+1/2}}{\Delta\alpha}\Bigg). \end{aligned} \tag{4.19}$$

4.2.2 The three-dimensional case

For the three-dimensional case we denote the field quantities, following Figure 2.1, as

$$E_\alpha|^n_{i,j,k} = E_\alpha((i-\frac{1}{2})\Delta\alpha, (j-1)\Delta\beta, (k-1)\Delta\gamma, n\Delta t)\,, \tag{4.20}$$

$$E_\beta|^n_{i,j,k} = E_\beta((i-1)\Delta\alpha, (j-\frac{1}{2})\Delta\beta, (k-1)\Delta\gamma, n\Delta t)\,, \tag{4.21}$$

$$E_\gamma|^n_{i,j,k} = E_\gamma((i-1)\Delta\alpha, (j-1)\Delta\beta, (k-\frac{1}{2})\Delta\gamma, n\Delta t)\,, \tag{4.22}$$

$$H_\alpha|^n_{i,j,k} = H_\alpha((i-1)\Delta\alpha, (j-\frac{1}{2})\Delta\beta, (k-\frac{1}{2})\Delta\gamma, n\Delta t)\,, \tag{4.23}$$

$$H_\beta|^n_{i,j,k} = H_\beta((i-\frac{1}{2})\Delta\alpha, (j-1)\Delta\beta, (k-\frac{1}{2})\Delta\gamma, n\Delta t)\,, \tag{4.24}$$

$$H_\gamma|^n_{i,j,k} = H_\gamma((i-\frac{1}{2})\Delta\alpha, (j-\frac{1}{2})\Delta\beta, (k-1)\Delta\gamma, n\Delta t)\,. \tag{4.25}$$

Furthermore, we redefine $\mathcal{H}$ of (4.15), using (4.4) and (4.6), as

$$\mathcal{H}(t) = \mathcal{G}^{-1}(t)\tilde{\mathcal{D}}(t)\,. \tag{4.26}$$

For using $\mathcal{H}$ on the discrete mesh we use the index convention of the respective field quantity to be updated, given in (4.20)-(4.25), and indicate this by annotating this quantity as a subscript to $\mathcal{H}$. This yields the following update equations for the H-field of the reference domain, given in (4.11) while assuming $\Delta\alpha = \Delta\beta = \Delta\gamma$:

$$H_\alpha|^{n+1/2}_{i,j,k} = H_\alpha|^{n-1/2}_{i,j,k} - \frac{\Delta t}{\epsilon\Delta\alpha} \begin{pmatrix} \mathcal{H}_{H_\alpha}|^n_{i,j,k}(1,1) \\ \mathcal{H}_{H_\alpha}|^n_{i,j,k}(1,2) \\ \mathcal{H}_{H_\alpha}|^n_{i,j,k}(1,3) \end{pmatrix}^T \boldsymbol{C}_{H\alpha}|^{n+1/2}_{i,j,k}\,, \tag{4.27}$$

$$H_\beta|^{n+1/2}_{i,j,k} = H_\beta|^{n-1/2}_{i,j,k} - \frac{\Delta t}{\epsilon\Delta\alpha} \begin{pmatrix} \mathcal{H}_{H_\beta}|^n_{i,j,k}(2,1) \\ \mathcal{H}_{H_\beta}|^n_{i,j,k}(2,2) \\ \mathcal{H}_{H_\beta}|^n_{i,j,k}(2,3) \end{pmatrix}^T \boldsymbol{C}_{H\beta}|^{n+1/2}_{i,j,k}\,, \tag{4.28}$$

$$H_\gamma|_{i,j,k}^{n+1/2} = H_\gamma|_{i,j,k}^{n-1/2} - \frac{\Delta t}{\epsilon \Delta \alpha} \begin{pmatrix} \mathcal{H}_{H_\gamma}|_{i,j,k}^{n}(3,1) \\ \mathcal{H}_{H_\gamma}|_{i,j,k}^{n}(3,2) \\ \mathcal{H}_{H_\gamma}|_{i,j,k}^{n}(3,3) \end{pmatrix}^T \boldsymbol{C}_{H\gamma}|_{i,j,k}^{n+1/2}. \tag{4.29}$$

For the related E-field of (4.10) the update equations are found as

$$E_\alpha|_{i,j,k}^{n+1} = E_\alpha|_{i,j,k}^{n} + \frac{\Delta t}{\epsilon \Delta \alpha} \begin{pmatrix} \mathcal{H}_{E_\alpha}|_{i,j,k}^{n+1/2}(1,1) \\ \mathcal{H}_{E_\alpha}|_{i,j,k}^{n+1/2}(1,2) \\ \mathcal{H}_{E_\alpha}|_{i,j,k}^{n+1/2}(1,3) \end{pmatrix}^T \boldsymbol{C}_{E\alpha}|_{i,j,k}^{n+1/2}, \tag{4.30}$$

$$E_\beta|_{i,j,k}^{n+1} = E_\beta|_{i,j,k}^{n} + \frac{\Delta t}{\epsilon \Delta \alpha} \begin{pmatrix} \mathcal{H}_{E_\beta}|_{i,j,k}^{n+1/2}(2,1) \\ \mathcal{H}_{E_\beta}|_{i,j,k}^{n+1/2}(2,2) \\ \mathcal{H}_{E_\beta}|_{i,j,k}^{n+1/2}(2,3) \end{pmatrix}^T \boldsymbol{C}_{E\beta}|_{i,j,k}^{n+1/2}, \tag{4.31}$$

$$E_\gamma|_{i,j,k}^{n+1} = E_\gamma|_{i,j,k}^{n} + \frac{\Delta t}{\epsilon \Delta \alpha} \begin{pmatrix} \mathcal{H}_{E_\gamma}|_{i,j,k}^{n+1/2}(3,1) \\ \mathcal{H}_{E_\gamma}|_{i,j,k}^{n+1/2}(3,2) \\ \mathcal{H}_{E_\gamma}|_{i,j,k}^{n+1/2}(3,3) \end{pmatrix}^T \boldsymbol{C}_{E\gamma}|_{i,j,k}^{n+1/2}. \tag{4.32}$$

The above vectors $\boldsymbol{C}_{H\alpha}, \ldots, \boldsymbol{C}_{E\gamma}$ provide for an averaging of the curl operation in the reference domain and are defined as

$$\boldsymbol{C}_{E\alpha}|_{i,j,k}^{n+1/2} = \begin{pmatrix} H_\gamma|_{i,j,k}^{n+1/2} - H_\gamma|_{i,j-1,k}^{n+1/2} - (H_\beta|_{i,j,k}^{n+1/2} - H_\beta|_{i,j,k-1}^{n+1/2}) \\ \hdashline \frac{1}{4}(H_\alpha|_{i,j-1,k}^{n+1/2} + H_\alpha|_{i,j,k}^{n+1/2} - H_\alpha|_{i,j-1,k-1}^{n+1/2} - H_\alpha|_{i,j,k-1}^{n+1/2} + \ldots \\ \ldots H_\alpha|_{i+1,j-1,k}^{n+1/2} + H_\alpha|_{i+1,j,k}^{n+1/2} - H_\alpha|_{i+1,j-1,k-1}^{n+1/2} - H_\alpha|_{i+1,j,k-1}^{n+1/2}) - \ldots \\ \ldots \frac{1}{4}(H_\gamma|_{i+1,j-1,k}^{n+1/2} + H_\gamma|_{i+1,j,k}^{n+1/2} - H_\gamma|_{i-1,j-1,k}^{n+1/2} - H_\gamma|_{i-1,j,k}^{n+1/2}) \\ \hdashline \frac{1}{4}(H_\beta|_{i+1,j,k-1}^{n+1/2} + H_\beta|_{i+1,j,k}^{n+1/2} - H_\beta|_{i-1,j,k-1}^{n+1/2} - H_\beta|_{i-1,j,k}^{n+1/2}) - \ldots \\ \ldots \frac{1}{4}(H_\alpha|_{i,j,k-1}^{n+1/2} + H_\alpha|_{i,j,k}^{n+1/2} - H_\alpha|_{i,j-1,k-1}^{n+1/2} - H_\alpha|_{i,j-1,k}^{n+1/2} + \ldots \\ \ldots H_\alpha|_{i+1,j,k-1}^{n+1/2} + H_\alpha|_{i+1,j,k}^{n+1/2} - H_\alpha|_{i+1,j-1,k-1}^{n+1/2} - H_\alpha|_{i+1,j-1,k}^{n+1/2}) \end{pmatrix}, \tag{4.33}$$

$$\boldsymbol{C}_{E\beta}|_{i,j,k}^{n+1/2} = \begin{pmatrix} \frac{1}{4}(H_\gamma|_{i-1,j+1,k}^{n+1/2} + H_\gamma|_{i,j+1,k}^{n+1/2} - H_\gamma|_{i-1,j-1,k}^{n+1/2} - H_\gamma|_{i,j-1,k}^{n+1/2}) - \dots \\ \dots \frac{1}{4}(H_\beta|_{i-1,j,k}^{n+1/2} + H_\beta|_{i,j,k}^{n+1/2} - H_\beta|_{i-1,j,k-1}^{n+1/2} - H_\beta|_{i,j,k-1}^{n+1/2} + \dots \\ \dots H_\beta|_{i-1,j+1,k}^{n+1/2} + H_\beta|_{i,j+1,k}^{n+1/2} - H_\beta|_{i-1,j+1,k-1}^{n+1/2} - H_\beta|_{i,j+1,k-1}^{n+1/2}) \\ \hline H_\alpha|_{i,j,k}^{n+1/2} - H_\alpha|_{i,j,k-1}^{n+1/2} - (H_\gamma|_{i,j,k}^{n+1/2} - H_\gamma|_{i-1,j,k}^{n+1/2}) \\ \hline \frac{1}{4}(H_\beta|_{i,j,k-1}^{n+1/2} + H_\beta|_{i,j,k}^{n+1/2} - H_\beta|_{i-1,j,k-1}^{n+1/2} - H_\beta|_{i-1,j,k}^{n+1/2} + \dots \\ \dots H_\beta|_{i,j+1,k-1}^{n+1/2} + H_\beta|_{i,j+1,k}^{n+1/2} - H_\beta|_{i-1,j+1,k-1}^{n+1/2} - H_\beta|_{i-1,j+1,k}^{n+1/2}) - \dots \\ \dots \frac{1}{4}(H_\alpha|_{i,j+1,k-1}^{n+1/2} + H_\alpha|_{i,j+1,k}^{n+1/2} - H_\alpha|_{i,j-1,k-1}^{n+1/2} - H_\alpha|_{i,j-1,k}^{n+1/2}) \end{pmatrix}, \tag{4.34}$$

$$\boldsymbol{C}_{E\gamma}|_{i,j,k}^{n+1/2} = \begin{pmatrix} \frac{1}{4}(H_\gamma|_{i-1,j,k}^{n+1/2} + H_\gamma|_{i,j,k}^{n+1/2} - H_\gamma|_{i-1,j-1,k}^{n+1/2} - H_\gamma|_{i,j-1,k}^{n+1/2} + \dots \\ \dots H_\gamma|_{i-1,j,k+1}^{n+1/2} + H_\gamma|_{i,j,k+1}^{n+1/2} - H_\gamma|_{i-1,j-1,k+1}^{n+1/2} - H_\gamma|_{i,j-1,k+1}^{n+1/2}) - \dots \\ \dots \frac{1}{4}(H_\beta|_{i-1,j,k+1}^{n+1/2} + H_\beta|_{i,j,k+1}^{n+1/2} - H_\beta|_{i-1,j,k-1}^{n+1/2} - H_\beta|_{i,j,k-1}^{n+1/2}) \\ \hline \frac{1}{4}(H_\alpha|_{i,j-1,k+1}^{n+1/2} + H_\alpha|_{i,j,k+1}^{n+1/2} - H_\alpha|_{i,j-1,k-1}^{n+1/2} - H_\alpha|_{i,j,k-1}^{n+1/2}) - \dots \\ \dots \frac{1}{4}(H_\gamma|_{i,j-1,k}^{n+1/2} + H_\gamma|_{i,j,k}^{n+1/2} - H_\gamma|_{i-1,j-1,k}^{n+1/2} - H_\gamma|_{i-1,j,k}^{n+1/2} + \dots \\ \dots H_\gamma|_{i,j-1,k+1}^{n+1/2} + H_\gamma|_{i,j,k+1}^{n+1/2} - H_\gamma|_{i-1,j-1,k+1}^{n+1/2} - H_\gamma|_{i-1,j,k+1}^{n+1/2}) \\ \hline H_\beta|_{i,j,k}^{n+1/2} - H_\beta|_{i-1,j,k}^{n+1/2} - (H_\alpha|_{i,j,k}^{n+1/2} - H_\alpha|_{i,j-1,k}^{n+1/2}) \end{pmatrix} \tag{4.35}$$

for the mapped electric field vector and as

$$\boldsymbol{C}_{H\alpha}|_{i,j,k}^{n} = \begin{pmatrix} E_\gamma|_{i,j+1,k}^{n} - E_\gamma|_{i,j,k}^{n} - (E_\beta|_{i,j,k+1}^{n} - E_\beta|_{i,j,k}^{n}) \\ \hline \frac{1}{4}(E_\alpha|_{i-1,j,k+1}^{n} + E_\alpha|_{i-1,j+1,k+1}^{n} - E_\alpha|_{i-1,j,k}^{n} - E_\alpha|_{i-1,j+1,k}^{n} + \dots \\ \dots E_\alpha|_{i,j,k+1}^{n} + E_\alpha|_{i,j+1,k+1}^{n} - E_\alpha|_{i,j,k}^{n} - E_\alpha|_{i,j+1,k}^{n}) - \dots \\ \dots \frac{1}{4}(E_\gamma|_{i+1,j,k}^{n} + E_\gamma|_{i+1,j+1,k}^{n} - E_\gamma|_{i-1,j,k}^{n} - E_\gamma|_{i-1,j+1,k}^{n}) \\ \hline \frac{1}{4}(E_\beta|_{i+1,j,k}^{n} + E_\beta|_{i+1,j,k+1}^{n} - E_\beta|_{i-1,j,k}^{n} - E_\beta|_{i-1,j,k+1}^{n}) - \dots \\ \frac{1}{4}(E_\alpha|_{i-1,j+1,k}^{n} + E_\alpha|_{i-1,j+1,k+1}^{n} - E_\alpha|_{i-1,j,k}^{n} - E_\alpha|_{i-1,j,k+1}^{n} + \dots \\ \dots E_\alpha|_{i,j+1,k}^{n} + E_\alpha|_{i,j+1,k+1}^{n} - E_\alpha|_{i,j,k}^{n} - E_\alpha|_{i,j,k+1}^{n}) \end{pmatrix}, \tag{4.36}$$

$$\boldsymbol{C}_{H\beta}|^n_{i,j,k} = \begin{pmatrix} \frac{1}{4}(E_\gamma|^n_{i,j+1,k} + E_\gamma|^n_{i+1,j+1,k} - E_\gamma|^n_{i,j-1,k} - E_\gamma|^n_{i+1,j-1,k}) - \dots \\ \frac{1}{4}(E_\beta|^n_{i,j-1,k+1} + E_\beta|^n_{i+1,j-1,k+1} - E_\beta|^n_{i,j-1,k} - E_\beta|^n_{i+1,j-1,k} + \dots \\ \dots E_\beta|^n_{i,j,k+1} + E_\beta|^n_{i+1,j,k+1} - E_\beta|^n_{i,j,k} - E_\beta|^n_{i+1,j,k}) \\ \hdashline E_\alpha|^n_{i,j,k+1} - E_\alpha|^n_{i,j,k} - (E_\gamma|^n_{i+1,j,k} - E_\gamma|^n_{i,j,k}) \\ \hdashline \frac{1}{4}(E_\beta|^n_{i+1,j-1,k} + E_\beta|^n_{i+1,j-1,k+1} - E_\beta|^n_{i,j-1,k} - E_\beta|^n_{i,j-1,k+1} + \dots \\ \dots E_\beta|^n_{i+1,j,k} + E_\beta|^n_{i+1,j,k+1} - E_\beta|^n_{i,j,k} - E_\beta|^n_{i,j,k+1}) - \dots \\ \dots \frac{1}{4}(E_\alpha|^n_{i,j+1,k} + E_\alpha|^n_{i,j+1,k+1} - E_\alpha|^n_{i,j-1,k} - E_\alpha|^n_{i,j-1,k+1}) \end{pmatrix}, \tag{4.37}$$

$$\boldsymbol{C}_{H\gamma}|^n_{i,j,k} = \begin{pmatrix} \frac{1}{4}(E_\gamma|^n_{i,j+1,k-1} + E_\gamma|^n_{i+1,j+1,k-1} - E_\gamma|^n_{i,j,k-1} - E_\gamma|^n_{i+1,j,k-1} + \dots \\ \dots E_\gamma|^n_{i,j+1,k} + E_\gamma|^n_{i+1,j+1,k} - E_\gamma|^n_{i,j,k} - E_\gamma|^n_{i+1,j,k}) - \dots \\ \dots \frac{1}{4}(E_\beta|^n_{i,j,k+1} + E_\beta|^n_{i+1,j,k+1} - E_\beta|^n_{i,j,k-1} - E_\beta|^n_{i+1,j,k-1}) \\ \hdashline \frac{1}{4}(E_\alpha|^n_{i,j,k+1} + E_\alpha|^n_{i+1,j,k+1} - E_\alpha|^n_{i,j,k-1} - E_\alpha|^n_{i,j+1,k-1}) - \dots \\ \hdashline \frac{1}{4}(E_\gamma|^n_{i+1,j,k-1} + E_\gamma|^n_{i+1,j+1,k-1} - E_\gamma|^n_{i,j,k-1} - E_\gamma|^n_{i,j+1,k-1} + \dots \\ E_\gamma|^n_{i+1,j,k} + E_\gamma|^n_{i+1,j+1,k} - E_\gamma|^n_{i,j,k} - E_\gamma|^n_{i,j+1,k}) \\ \hdashline E_\beta|^n_{i+1,j,k} - E_\beta|^n_{i,j,k} - (E_\alpha|^n_{i,j+1,k} - E_\alpha|^n_{i,j,k}) \end{pmatrix} \tag{4.38}$$

for the mapped magnetic field vector.

4.3 Boundary Conditions for Fast Moving Structures

For boundaries moving at speeds not negligible compared to the speed of light, c_0, we must take relativistic boundary conditions into account. Maxwell's equations are invariant with respect to their inertial frame. We consider the two inertial frames K and K' that are in relative motion, described by the velocity vector $\boldsymbol{v}$, to each other as depicted in Figure 4.5. The field quantities in K' can be obtained from the field

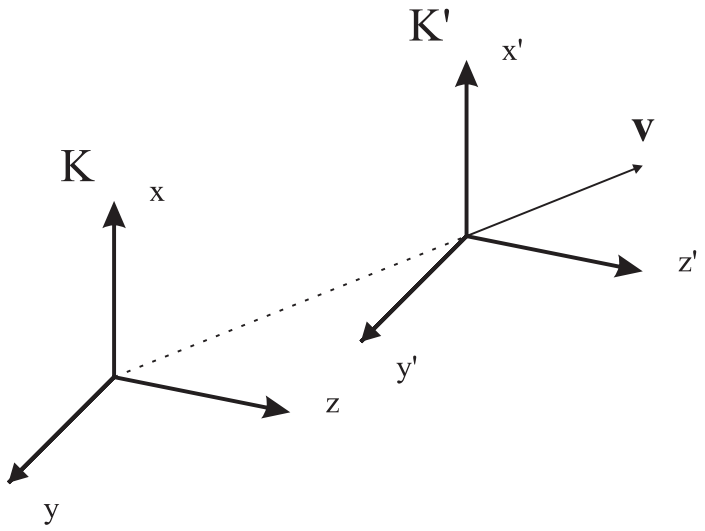

Figure 4.5: Two inertial frames K and K' in relative motion to each other.

quantities in K by means of the Lorentz transformation, yielding [98]

$$\boldsymbol{E}' = \boldsymbol{E}_{\parallel} + \frac{1}{\sqrt{1-\beta^2}}\left(\boldsymbol{E}_{\perp} + \boldsymbol{v}\times\boldsymbol{B}\right), \tag{4.39}$$

$$\boldsymbol{B}' = \boldsymbol{B}_{\parallel} + \frac{1}{\sqrt{1-\beta^2}}\left(\boldsymbol{B}_{\perp} - \frac{\boldsymbol{v}\times\boldsymbol{E}}{c_0^2}\right), \tag{4.40}$$

$$\boldsymbol{D}' = \boldsymbol{D}_{\parallel} + \frac{1}{\sqrt{1-\beta^2}}\left(\boldsymbol{D}_{\perp} + \frac{\boldsymbol{v}\times\boldsymbol{H}}{c_0^2}\right), \tag{4.41}$$

$$\boldsymbol{H}' = \boldsymbol{H}_{\parallel} + \frac{1}{\sqrt{1-\beta^2}}\left(\boldsymbol{H}_{\perp} - \boldsymbol{v}\times\boldsymbol{D}\right), \tag{4.42}$$

where $\parallel$ and $\perp$ denote the field quantities parallel and perpendicular to the velocity $\boldsymbol{v}$. For a moving perfectly electrically conducting (PEC) surface, the total tangential electric field component $E_{||,\mathrm{tot}}$ is given by [21, 101]

$$E_{||,\mathrm{tot}} = \frac{2\beta_v}{1+\beta_v} E_{||,\mathrm{inc}}\,, \tag{4.43}$$

where $E_{||,\mathrm{inc}}$ denotes the incident tangential electric field, and

$$\beta_v = -\frac{1}{c_0}\hat{n}\cdot\boldsymbol{v}\,, \tag{4.44}$$

where $\hat{n}$ is the boundary's surface normal. The terms $\boldsymbol{v}$ and $\hat{n}$ are evaluated for the deformed configuration either directly in the deformed domain or after a map in the reference domain.

4.4 Numerical Stability Considerations

The LM FDTD method is suitable, as we will demonstrate in the next chapter, to model modest curvatures and smooth deformations, of the static or time-varying type, in a medium. The stability criteria discussed in Section 2.2.2 will not hold true in general for the mapped FDTD. One aspect we have to consider is that the CFL condition has to be satisfied for the deformed grid, and thus the minimum grid spacing in the deformed grid will be relevant for determining a suitable time step. Moreover, considering the equivalence of the governing equations of the static LM method to Maxwell's equations for a general anisotropic material, as we have seen in (4.13)-(4.14), we see that the FDTD implementation is equivalent to that for a general anisotropic problem. The implementation of an anisotropic FDTD scheme is not trivial and is often conflicted by long-term instabilities. The stability of anisotropic FDTD schemes has been discussed in [110–113]. For the Yee scheme the electric and magnetic field components are spatially separated on the grid, requiring spatial interpolation over electric or magnetic field values exposed to different material parameters in order to obtain the respective flux densities. Thus, errors are easily introduced. These stability issues are not inherent to the LM method; rather, they are caused by the way the method is implemented numerically. Strong deformations of the grid in the LM method are reflected in the tensor matrices equivalent to strong anisotropy. The limitations on the grid deformation are thus directly related to the robustness of the implemented anisotropic FDTD scheme.

Chapter 5

Numerical Validation of the LM Method

In order to validate the proposed method we have chosen to apply it to the electromagnetic modeling of four structures: a two-dimensional, stationary rectangular cavity with an indentation in one of its four metallic walls; a three-dimensional metallic resonator shaped like a truncated cylinder; a parallel-plate waveguide with a non-rectangular, stationary periodic corrugation in one of its two walls; and a parallel-plate waveguide with a moving, periodic corrugation.

5.1 Eigenanalysis of a Two-Dimensional Deformed Rectangular Metallic Resonator

The resonator we consider has the dimensions $a = 3$ cm $\times$ $b = 4$ cm and is filled with air. The walls are perfect electric conductors (PEC) and we are interested in calculating the eigenfrequencies of the TM modes of the resonator in the presence of an indentation in the top wall. In the absence of any indentation the resonant frequencies of the modes are given by

$$f_{m,n} = \frac{1}{2\pi\sqrt{\mu\epsilon}}\sqrt{\left(\frac{m\pi}{a}\right)^2 + \left(\frac{n\pi}{b}\right)^2}, \tag{5.1}$$

where the indices m, n define the mode number. The deformed resonator is shown in Figure 5.1. The indentation of the top plate is defined mathematically in terms of

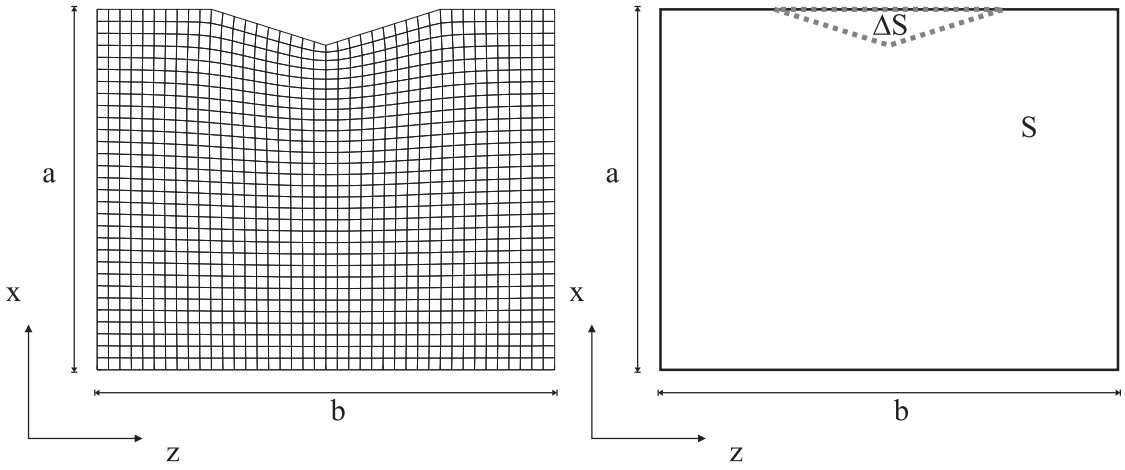

(a) Deformed resonator mesh.

(b) Areas used for the calculation of the eigenfrequencies using perturbational techniques.

Figure 5.1: Geometry and gridding of the deformed resonator.

the function

$$\mathrm{a}'(z) = \begin{cases} \mathrm{a} & |z - \mathrm{b}/2| \geq \mathrm{b}/4 \\ (1 - 0.1(\frac{4z}{\mathrm{b}} - 1))\mathrm{a} & \mathrm{b}/4 < z \leq \mathrm{b}/2 \\ (1 - 0.1(3 - \frac{4z}{\mathrm{b}}))\mathrm{a} & \mathrm{b}/2 < z < 3/4\mathrm{b} \end{cases}, \tag{5.2}$$

with $0 \leq z \leq \mathrm{b}$, yielding a triangular shaped dent. For an analytic means of approximating the resonant frequencies of the deformed resonator, we use a perturbational technique [114]. The shift $\Delta\omega_r$ in the resonant frequency ω_r is calculated through the expression

$$\frac{\Delta\omega_r}{\omega_r} \approx \frac{\iint_{\Delta S}(\mu|H_0|^2 - \epsilon|E_0|^2)ds}{\iint_S(\mu|H_0|^2 + \epsilon|E_0|^2)ds}\,. \tag{5.3}$$

Referring to Figure 5.1(b), S is the area of the non-deformed rectangular box, whereas ΔS denotes the area of the indentation. H_0 and E_0 are the fields of the mode for the unperturbed resonator. We expect the analytic result obtained using the above equation to serve as a good indicator of the shift in the resonant frequencies of the cavity caused by the indentation.

Our calculation of the resonant frequencies of the perturbed resonator relies on its

Table 5.1: Resonant frequencies of the two-dimensional metallic resonator depicted in Figure 5.1

	mode order				
m	0	1	1	0	1
n	1	0	1	2	2
Unperturbed resonator	Resonant frequency (GHz)				
Analytic solution (5.1)	3.74	4.99	6.24	7.49	9.00
Equation (5.2) perturbed resonator					
Equation (5.3) perturbational technique	3.59	5.23	6.17	7.64	9.22
Lagrangian FDTD (1 mm grid spacing)	3.67	5.11	6.18	7.53	9.15
Lagrangian FDTD (2 mm grid spacing)	3.67	5.11	6.18	7.51	9.14
TLM (1 mm grid spacing)	3.62	5.11	6.14	7.56	9.16
TLM (2 mm grid spacing)	3.66	5.42	6.44	7.55	9.37

excitation by a pulse and the subsequent Fourier transform of the transient response obtained from the Lagrangian FDTD simulation. In addition, we have computed the resonant frequencies using the TLM field solver MEFiSTo[1] [22], which utilizes a rectangular grid.

The results obtained from the three approaches are listed in Table 5.1, along with the values of the resonant frequencies of the unperturbed resonator. The results of the Lagrangian FDTD and the TLM solution follow closely the trend predicted by (5.3) and are in very good agreement with each other when the grid size in the reference Cartesian grid is 1 mm. As the grid becomes coarser, with its grid size assuming a value of 2 mm, the values for the resonant frequencies obtained by the Lagrangian FDTD method change only very little. Since the dent extends into the resonator by 3 mm, a grid resolution of 2 mm in a staircase approximation of the indentation will be too coarse to model the shape of the metallic wall accurately. However, the Lagrangian FDTD method enables us to obtain accurate results even when using a coarser grid.

[1]MEFiSTo: Multi-purpose Electromagnetic Field Simulation Tool, Faustus Scientific Corporation, 1256 Beach Dr., Victoria, BC, V8S 2N3 Canada, `http://www.faustcorp.com`

5.2 Analysis of the Eigenfrequencies of a Three-Dimensional Cylindrical Section

The following example studies the eigenfrequencies of a three-dimensional resonator. The studied structure has the shape of a truncated cylinder with PEC walls and is air-filled. The cylindrical resonator is based on a rectangular box of the dimensions $a \times b \times d$. The base of the cylinder lies in the xy-plane, the cylinder's axis is parallel

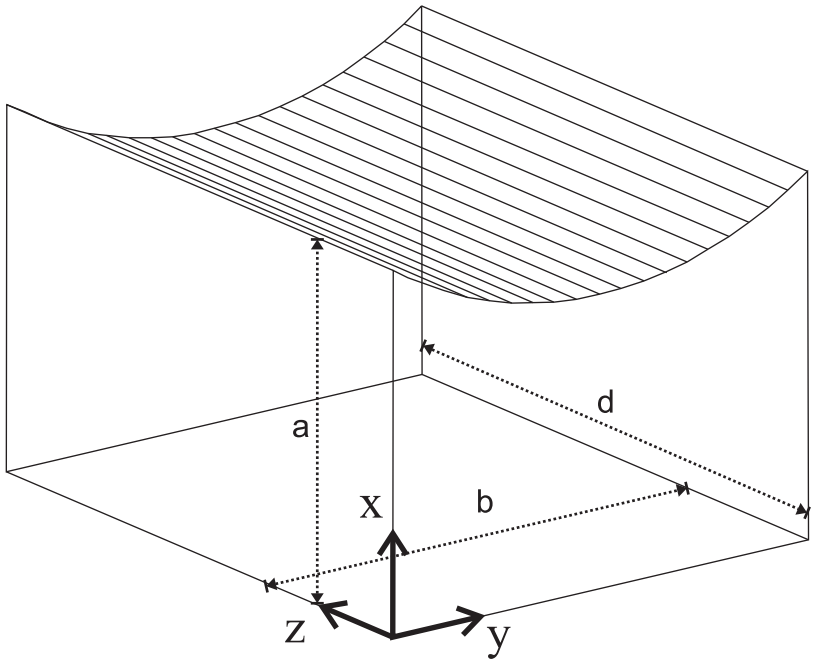

Figure 5.2: Geometry of the cylindrical resonator.

to the z-coordinate axis. The top plate of the resonator is deformed such that the cylinder's base in the xy-plane is described by a rectangle for which the top border has been replaced by a segment of a circle through the points $(a \cdot \hat{x}, 0 \cdot \hat{y})$, $(0.95a \cdot \hat{x}, b/2 \cdot \hat{y})$ and $(a \cdot \hat{x}, b \cdot \hat{y})$. The cylinder is sketched in Figure 5.2. The dimensions of the resonator are $a = 30$ mm, $b = 40$ mm, and $d = 50$ mm. For the undeformed resonator

the resonant frequencies are found to be

$$f_{m,n,p} = \frac{1}{2\pi\sqrt{\mu\epsilon}}\sqrt{\left(\frac{m\pi}{a}\right)^2 + \left(\frac{n\pi}{b}\right)^2 + \left(\frac{p\pi}{d}\right)^2}, \tag{5.4}$$

with

$$m = 0, 1, 2, \dots, \quad n = 0, 1, 2, \dots, \quad p = 1, 2, 3, \dots, \qquad m + n \neq 0\,, \tag{5.5}$$

for TE modes and

$$m = 1, 2, 3, \dots, \quad n = 1, 2, 3, \dots, \quad p = 0, 1, 2, \dots, \tag{5.6}$$

for TM modes. Hence, the dominant modes are the TE_{101}, TE_{011}, and TM_{110} modes. The eigenfrequencies are obtained using the LM method for the three-dimensional LM FDTD (4.27)-(4.32), and reference solutions are obtained from the FEM solver HFSS[2] and the TLM solver MEFiSTo. The computed eigenfrequencies are presented in Table 5.2. As for the two-dimensional example of the previous section, the LM method achieves good accuracy with a relatively coarse grid, which can be seen by comparing the results of the LM method to those of the TLM method with a rectangular grid.

5.3 Analysis of a Corrugated Parallel-Plate Waveguide

Electromagnetic wave propagation in periodic structures is an extensively studied phenomenon [115–124]. A comprehensive overview of wave propagation in active and passive periodic structures is given in [125]. The periodic structure can arise

[2]HFSS: High Frequency Structural Simulator, ANSOFT, LLC, 225 West Station Square Dr., Suite 200, Pittsburgh, PA 15219, U.S.A., `http://www.ansoft.com`

Table 5.2: Resonant frequencies of the three-dimensional metallic resonator sketched in Figure 5.2

	mode order		
m	0	1	1
n	1	0	1
p	1	1	0
Unperturbed resonator	Resonant frequency (GHz)		
Analytic solution (5.4)	4.80	5.83	6.25
Perturbed resonator (see Figure 5.2)			
HFSS FEM	4.77	5.97	6.43
LM FDTD (2.5 mm grid spacing)	4.76	6.00	6.43
TLM (2.5 mm grid spacing)	4.68	5.98	6.56
TLM (0.625 mm grid spacing)	4.77	5.99	6.45

from the crystalline structure of the medium, a thermal grating or acoustic waves propagating through the medium and deforming it. Due to the scattering of the wave by the periodic structure, the medium becomes dispersive and the dispersion diagram exhibits pass-bands alternating with stop-bands. In the case of a propagating periodic perturbation the scattered waves exhibit a Doppler shift, so the dispersion characteristic is shifted in frequency. The case of the propagating perturbation will be addressed in Section 5.4.

The objective of this study is to investigate and model the transmission properties of a corrugated, air-filled, parallel-plate waveguide under TM excitation. The periodic corrugation is due to indentations of the top wall as shown in Figure 5.3. We have cascaded 15 sections to form the periodically corrugated part of the waveguide that will serve as a filter structure. Figure 5.3 depicts the deformed grid of the parallel-plate waveguide for two cascaded sections.

The PEC walls of the waveguide have a maximum plate separation of $d = 1$ cm. At its narrowest, the distance between of the plates is reduced to 70% of the original separation. The distance from the top wall to the bottom wall versus z is described

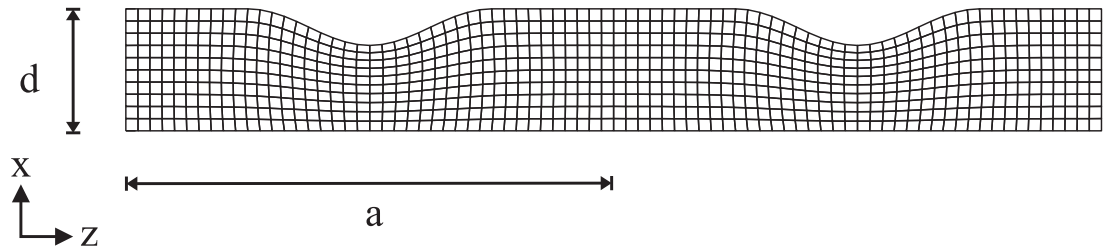

(a) Deformed grid for Lagrangian FDTD Approach.

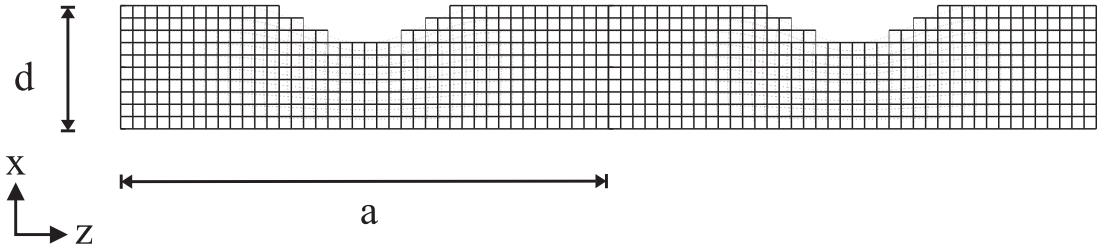

(b) Stair case approximation for standard FDTD (1 mm grid spacing).

Figure 5.3: Two sections of the corrugated parallel-plate waveguide.

by

$$d'(z) = \begin{cases} d & |z - a/2| \geq a/4 \\ \big(1 - 0.3\cos^2([2z/a - 1]\pi)\big)d & a/4 < z < 3a/4 \end{cases}, \tag{5.7}$$

with $0 \leq z \leq a$, as shown in Figure 5.3. The waveguide is excited in the fundamental mode with a modulated Gaussian pulse with its center frequency at 4.7 GHz and a 3 dB bandwidth of 2.5 GHz. Because the indentations serve as a periodic capacitive loading of the guide, we expect a stop-band at around 3.75 GHz and 7.5 GHz [126] for a periodic interval of $a = 4$ cm. The magnitude of the transmission coefficient, S_{21}, is plotted in Figure 5.4 with the solid line showing the results obtained from the Lagrangian FDTD method and the dashed lines those obtained using a standard FDTD method with staircase approximation of the corrugated boundary. Figures 5.4(a)-5.4(c) show $|S_{21}|$ obtained with grid spacings of 0.5 mm, 1 mm and 2 mm. The vertical lines in the figures mark the frequencies where the value of $|S_{21}|$ meets the -3 dB level. Numerical values for the -3 dB frequencies are given in Table 5.3.

As it is evident from the plots and the data, the Lagrangian FDTD method

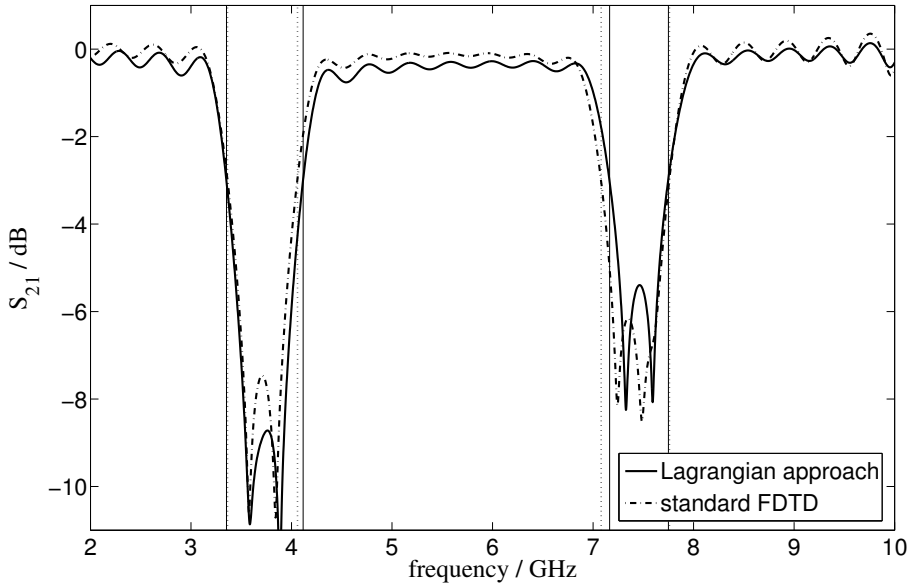

(a) Grid spacing 0.5 mm.

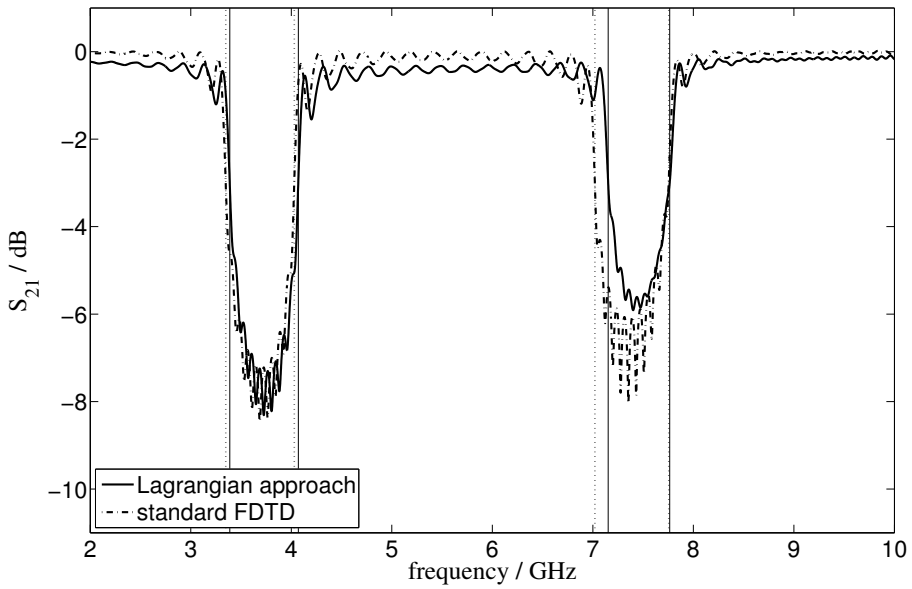

(b) Grid spacing 1 mm.

Figure 5.4: Magnitude of the transmission coefficient, $|S_{21}|$, of the corrugated waveguide for different grid resolutions. Vertical lines mark -3 dB frequency points for Lagrangian (solid line) and standard FDTD (dotted line) method.

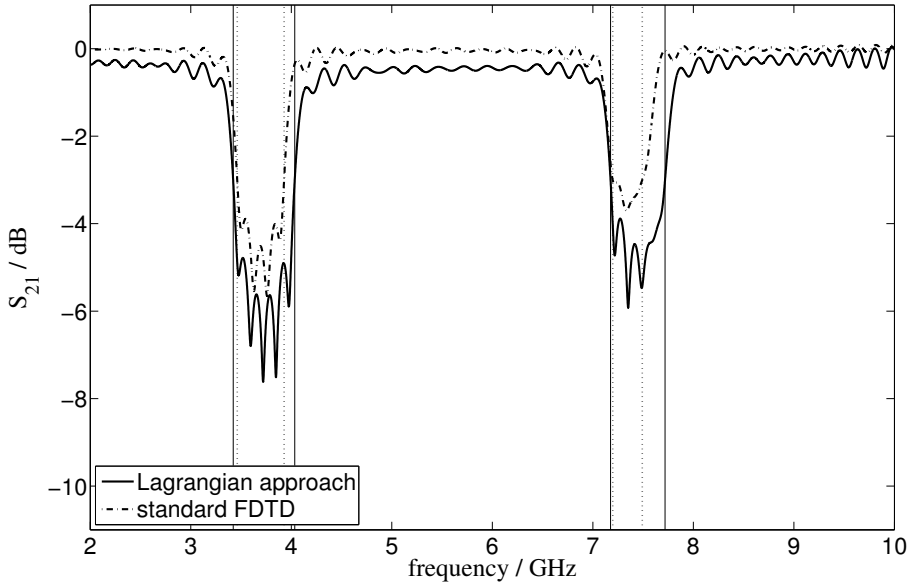

(c) Grid spacing 2 mm.

Figure 5.4: (cont.)

Table 5.3: −3 dB frequency points of the falling (F) and rising (R) edges of the $|S_{21}|$ graph.

method	grid spacing / mm	−3 dB frequency / GHz			
		lower		upper stop-band	
		F	R	F	R
Lagrangian FDTD	0.5	3.35	4.11	7.16	7.74
	1.0	3.38	4.07	7.15	7.76
	2.0	3.42	4.03	7.17	7.71
standard FDTD	0.5	3.36	4.05	7.08	7.76
	1.0	3.34	4.02	7.02	7.75
	2.0	3.46	3.92	7.19	7.49

sustains better accuracy as the grid becomes coarser. For the case of the finest grid resolution, with a grid size of 0.5 mm, the results obtained from Lagrangian FDTD and the standard FDTD method are in very good agreement. For coarser grids the accuracy of the standard FDTD method degrades, especially at higher frequencies, as expected. The staircase approximation of the standard FDTD in a grid with a spacing of 2 mm is too coarse to resolve accurately the 3 mm deep corrugation. However, the Lagrangian FDTD method is capable of predicting the -3 dB frequencies for the falling and rising edges of the upper stop-band with sustained accuracy even at a grid resolution of 2 mm.

5.4 Analysis of a Parallel-Plate Waveguide with a Moving Corrugation Profile

A periodically in time and space modulated medium gives rise to an electromagnetic bandgap structure. The band characteristic can be shifted by tuning the time modulation of the medium. We compare the effect of a sinusoidally modulated structure on the bandgap using an FDTD implementation for curved moving boundaries with an approximation to the analytic solution derived from Floquet's theorem. For the latter, we consider the mutual coupling of a finite set of time-space harmonics.

Analytic solutions to the wave equation in a medium changing periodically in space can be found with the help of Mathieu functions [127–129] and for the more general case of time- and space-periodic media by use of Floquet's theorem [130, 131]. For the latter case, energy transfer between the electromagnetic wave and the wave exhibited by the varying material parameters may occur in the form of a parametric amplification [132, 133]. The effect of the variation in time of the periodic structure on the bandgap characteristic can be utilized to create tunable filter structures.

5.4.1 Formulation of the problem

We consider a filter structure consisting of a parallel plate waveguide with perfectly electrically conducting (PEC) corrugated walls and filled by a dielectric with the permittivity ϵ_m. The variation of the plate separation is described by the function

$$d(t,z) = \frac{d_0}{\sqrt{1 + M\cos(\omega_p t - \beta_p z)}} \tag{5.8}$$

and depicted in Figure 5.5. The spatial period in (5.8) is given by a and thus $\beta_p = 2\pi/a$. The problem is two-dimensional hence we use the reduced formulation

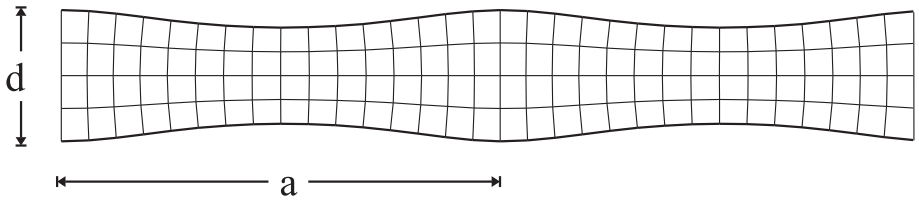

Figure 5.5: Two sections of the corrugated parallel-plate waveguide.

in the FDTD mapping approach. The variation of the plate separation modulates the capacitive loading of the waveguide and the impedance is proportional to the plate separation. The mapping method provides for a rigorous formulation for general boundary displacements. However, in this particular case the plate separation translates into an impedance modulation $Z = \sqrt{\frac{\mu}{\epsilon_m}}\frac{d}{w}$, where w is the waveguide's width, which is equivalent to a one-dimensional transmission line with

$$\epsilon(t,z) = \epsilon_m + \Delta\epsilon\cos(\omega_p t - \beta_p z)\,, \tag{5.9}$$

μ = const., and $M = \Delta\epsilon/\epsilon_m$. We will use this permittivity variation in the one-dimensional wave equation for our analytic reference solution.

5.4.2 Analytic approach

For a one-dimensional transmission line Maxwell's equations yield, using ϵ from (5.9),

$$\frac{\partial^2 E_x}{\partial z^2} = \mu_0 \frac{\partial^2}{\partial t^2}(\epsilon E_x)\,. \tag{5.10}$$

We follow [118–120] and choose the Floquet ansatz to solve (5.10)

$$E_x = E_0 \mathrm{e}^{-\jmath(\omega t - \kappa z)} \sum_{n=-\infty}^{+\infty} a_n \mathrm{e}^{-\jmath n(\omega_p t - k_p z)}\,. \tag{5.11}$$

This yields the following relation for neighboring Fourier coefficients of (5.11)

$$a_{n+1} + D_n a_n + a_{n-1} = 0\,, \tag{5.12}$$

with

$$D_n = \frac{2\epsilon_m}{\Delta\epsilon}\Big[1 - \Big(\frac{\kappa a + 2\pi n}{k a + 2\pi v n}\Big)^2\Big]\,, \tag{5.13}$$

$v = v_p/v_0$, $v_p = \omega_p/\beta_p$, $v_0 = \omega/k$ and $k = \omega\sqrt{\mu\epsilon_m}$. Finally, (5.12) is expanded into the recursive relation using continued fraction expansions

$$D_n - \cfrac{1}{D_{n-1} - \cfrac{1}{D_{n-2} - \cfrac{1}{\ddots}}} - \cfrac{1}{D_{n+1} - \cfrac{1}{D_{n+2} - \cfrac{1}{\ddots}}} = 0\,, \tag{5.14}$$

which is truncated for the numerical computation after a chosen value for n. Equation (5.14) is solved using a nonlinear Newton method [134] and yields a relation for $\kappa(\omega)$ respectively $\omega(\kappa)$. To ensure convergence of the above method v should be outside

the interval specified by [119, 120]

$$\frac{1}{\sqrt{1+\Delta\epsilon/\epsilon_m}} \leq v \leq \frac{1}{\sqrt{1-\Delta\epsilon/\epsilon_m}}\,. \tag{5.15}$$

5.4.3 Results

We have computed the bandpass characteristic using the analytic method and the mapping approach for a transmission line with $\epsilon_m = 2\epsilon_0$, $\Delta\epsilon_m = 0.6\epsilon_0$ for (5.9) and hence $M = 0.3$ in (5.8). The period length is chosen $a = 4$ cm and the constant for the plate separation $d_0 = 1$ cm; thus, we find the plate separation varying between $d_{min} = 0.88d_0$ and $d_{max} = 1.2d_0$. The waveguide is excited below higher order cut-off frequencies, exciting only the fundamental, transverse electromagnetic (TEM) mode. The frequency f_{bg} of the stop-band can be estimated from the condition for the Bragg reflection [135] yielding maximum reflection for

$$f_{bg,n} = \frac{n}{2a\sqrt{\mu\epsilon_m}}\,, \tag{5.16}$$

where n is the order of the stop-band, and hence $f_{bg,1} = 2.65$ GHz, $f_{bg,2} = 5.30$ GHz.

The frequency f' observed by a moving corrugation profile deviates from the actual frequency f according to the Doppler effect

$$f' = f\sqrt{\frac{1-v_p/c}{1+v_p/c}}\,, \tag{5.17}$$

with $c = 1/\sqrt{\mu\epsilon_m}$. Hence, for the case where the propagation vector of the TEM wave and of the corrugation profile point in the same direction, the observed frequency f' is reduced. The Bragg condition will apply to the observed frequency f' and occur at a frequency f, which increases along with v_p. Thus the stop-bands shift upward in frequency. Conversely, it will shift to lower frequencies for an opposite directed

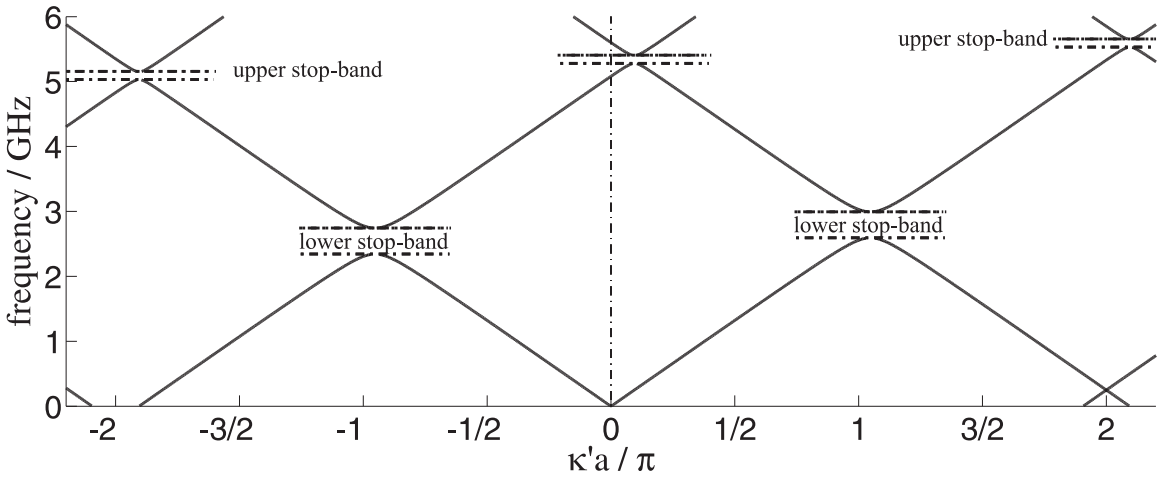

Figure 5.6: Dispersion diagram.

motion of the corrugation profile.

Due to the difference in the velocity of the moving boundary and the guided electromagnetic wave and hence a phase mismatch, we do not consider parametric amplification an issue. Approximating the analytic solution in (5.14) numerically yields the dispersion relation graphed in Figure 5.6 for $v_p = 1 \times 10^7$ m/s and $v_p = -1 \times 10^7$ m/s, with $\kappa = \kappa' - \jmath\kappa''$. Whereas this solution is for an infinite structure, we consider for the mapped FDTD method a waveguide section with 30 periods (see Figure 5.5). The waveguide is excited at one side of the moving corrugated section with a modulated Gaussian pulse and sampled at the other side. The power spectrum of the input signal is centered at 4.7 GHz and the full-width at half-maximum (FWHM) bandwidth is given as 2.9 GHz. The mesh spacing in the numerical reference grid is 2.5 mm. We have computed the lower and upper edge of the first stop-band of the fundamental mode, and the center frequencies of the first two stop-bands. For the FDTD method the lower and upper edge for the stop-band are specified as the frequency points where the energy transfer drops to $S_{21}(f) = -3$ dB. The S_{21} parameter of the waveguide for $v_p = -1 \times 10^7$ m/s, $v_p = 0$ m/s, and $v_p = 1 \times 10^7$ m/s is shown in Figures 5.7 and 5.8. For the solution of (5.14) at $v_p = 0$ we find κ'' at the

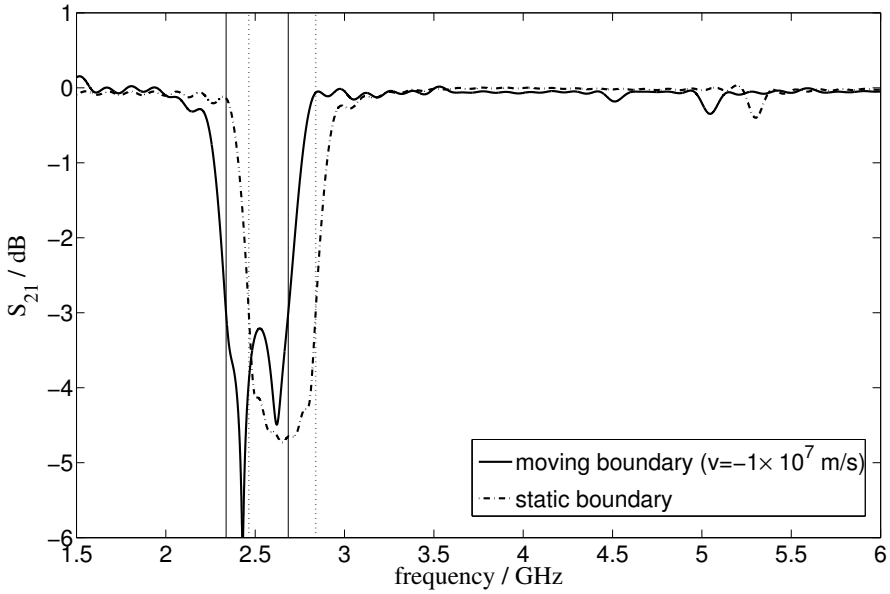

Figure 5.7: Transmission coefficient $|S_{21}|$ for moving boundary with $v_p = -1 \times 10^7$ m/s and $v_p = 0$ m/s. Vertical lines mark the -3 dB frequency points.

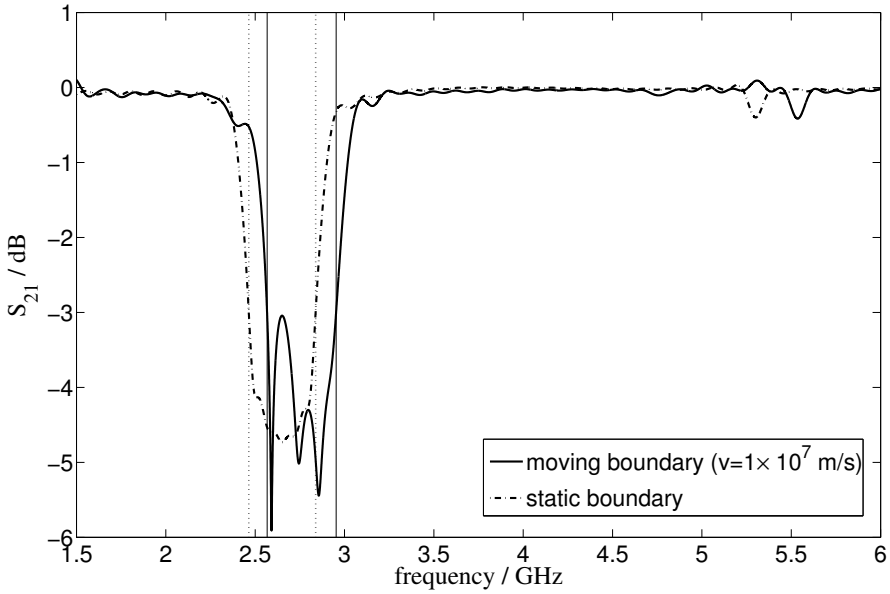

Figure 5.8: Transmission coefficient $|S_{21}|$ for a moving boundary with $v_p = 1 \times 10^7$ m/s and $v_p = 0$ m/s. Vertical lines mark the -3 dB frequency points.

Table 5.4: Stop-band frequencies of a time-space periodic waveguide with its profile depicted in Figure 5.5, with results obtained from the Doppler shift approximation, analytic solution and LM FDTD method.

	frequency **lower stop-band** / GHz						
v	Doppler	analytic			LM FDTD		
/ ms^{-1}	approx.	lower edge	upper edge	center	lower edge	upper edge	center
-1×10^7	2.53	2.34	2.74	2.54	2.34	2.69	2.51
0	2.65	2.47	2.87	2.67	2.46	2.84	2.65
1×10^7	2.78	2.59	2.99	2.79	2.57	2.95	2.76

	frequency **upper stop-band** / GHz						
v	Doppler	analytic			LM FDTD		
/ ms^{-1}	approx.	lower edge	upper edge	center	lower edge	upper edge	center
-1×10^7	5.06	5.03	5.16	5.09	-	-	5.04
0	5.30	5.29	5.41	5.35	-	-	5.30
1×10^7	5.56	5.53	5.66	5.59	-	-	5.54

center of the lower and upper stop-band to be $\kappa''_{bg,1} = 1.78\ \mathrm{m}^{-1}$ and $\kappa''_{bg,2} = 5.9\ \mathrm{m}^{-1}$. The difference in κ'' is reflected in different attenuation levels of the two stop-bands in the plots of Figures 5.7 and 5.8. However, these values for κ'' are applicable to an infinite structure. The frequencies for the stop-band are presented in Table 5.4 with results obtained from an approximation using the Bragg condition (5.16) and the Doppler effect (5.17), using the analytic approach for TEM waves of (5.14), and the FDTD implementation of the mapped equations in (4.9). The values obtained for the stop-band frequencies are in good agreement for the different methods.

We have excited the waveguide with a sinusoidal in the spectrum of the pass-band and we have computed the S_{21} parameter using the mapping FDTD. The results for the input signal at $f = 4.2$ GHz are plotted in Figure 5.9. For the corrugation profile moving with $v_p = 1 \times 10^7$ m/s we observe intermodulation products at very low power levels at frequencies separated by integer multiples of $f_p = \omega_p/(2\pi) = \beta_p v_p/(2\pi) = 250$ MHz away from the excitation frequency, as suggested in Floquet's ansatz (5.11).

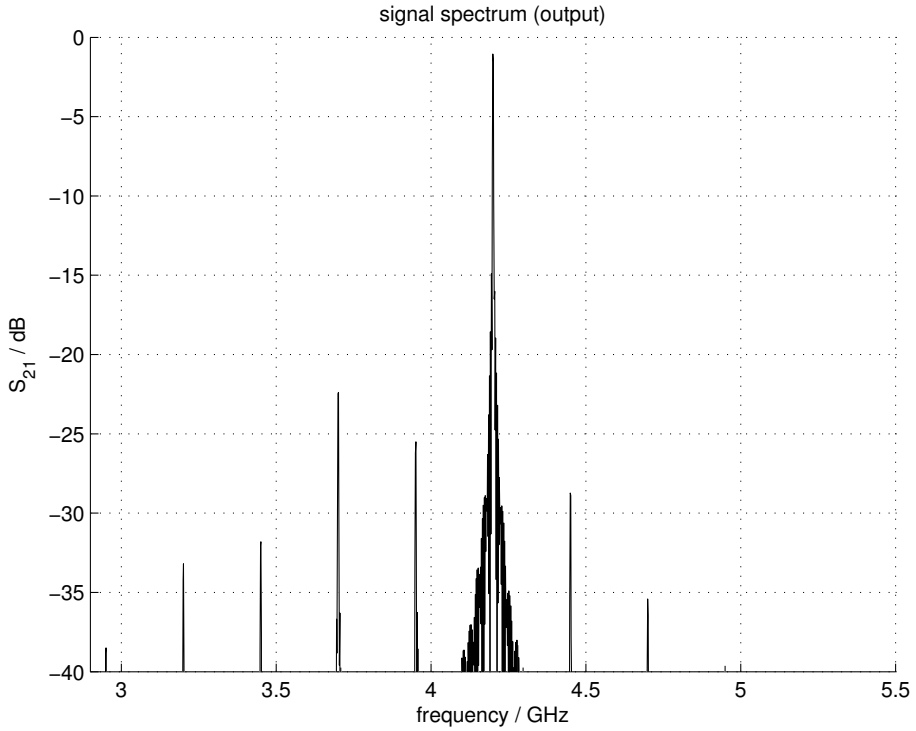

Figure 5.9: Transmission coefficient $|S_{21}|$ for a moving boundary with $v_p = 1 \times 10^7$ m/s, excited at $f = 4.2$ GHz.

5.5 Conclusion

An FDTD method based on a Lagrangian mapping approach has been developed for a computationally efficient numerical modeling of electromagnetic structures with curved moving boundaries. In this method the physical domain is mapped by a time-dependent mapping on a reference domain such that the boundary surfaces are fixed coordinate surfaces in the reference domain and conform with Yee's grid. The map of Maxwell's equations on the reference domain is interpreted in terms of a Maxwellian equation system describing wave propagation with a modified nabla operator inside a domain with boundaries parallel to the planes of the Cartesian reference coordinate system. This allows a straightforward application of Yee's FDTD scheme and yields high numerical efficiency and low computational effort together

with high accuracy. The staircase approximation of the curved boundaries is avoided and boundary conditions are applied accurately. This results in enhanced accuracy in the numerical solution without the need for finer grid resolution.

Numerical studies in two and three dimensions were used to demonstrate the accuracy of the proposed Lagrangian FDTD method. For the static case we have presented the example of a perturbed resonator in two and three dimensions, and of a two-dimensional space periodic filter. Furthermore, a time-space periodic filter structure has been analyzed for the tunability of its band-gaps to validate the time-dependent mapping approach. We have compared the results to an analytic solution existing for the infinite extended time-space periodic structure. The moving boundaries in this numerical example move with very high velocity. When choosing a velocity of the periodic boundary motion that could be attributed to acoustic phenomena, for example, the disparity between the temporal scale of the electromagnetic wave, which we will refer to as $T_1 = 1/f_1$, on the one hand, and the temporal scale at which the periodic motion of the boundary takes place, denoted as $T_2 = 1/f_2$, on the other hand, will increase tremendously. As a result the computational cost will increase significantly and long-term instabilities in the numerical simulation will be of great concern. To compute the interaction between the EM wave and the boundary motion in our example, the computational cost scales as $O(f_1/f_2 = 16)$, with $f_1 \approx 4.0$ GHz and $f_2 \approx 1 \times 10^7$ ms^{-1}/$(4 \times 10^{-2}$ m$) = 0.25$ GHz. If we consider a periodic boundary motion at $v = 400$ ms^{-1}, a value that could very well be attributed to some acoustic wave phenomena, the complexity scales as $O(f_1/f_2 = 4 \times 10^5)$. This scaling in complexity, which is tied to the ratio of the temporal scales involved, is a challenge frequently encountered in the modeling of multi-domain physical interactions. We will address this problem in the next chapter, through the development of a method that makes use of multiple time variables to relax the significant computational overhead

stemming from temporal oversampling.

Chapter 6

A Multi-Time Solution Approach to Problems of Electromagnetic Wave-Propagation Exhibiting Widely Separated Time Scales

Widely separated time scales in EM circuit and EM wave propagation problems pose significant computational challenges to their numerical solution. Large disparity between governing time scales leads to increased computational cost manifested in terms of increased processing time for obtaining the response and increased memory requirements. This is due to the necessity to choose a long time interval in order to capture the slow time scale and at the same time choose a fine temporal resolution to accommodate the fast time scale. In addition to the increase in the computational cost, we may face further problems like long-term instabilities. Different time scales in circuit simulations are often handled by the technique of harmonic balance or by use of shooting methods [136]. Harmonic balance is preferable if there are no or only weak nonlinearities present, and it is very efficient for sinusoidal excitations. The shooting method, on the other hand, handles nonlinearities well. However, it is not well suited for distributed problems such as transmission lines. The demand for a fine temporal resolution in order to fulfill the CFL condition can be avoided, if an unconditionally stable alternate direction implicit (ADI) scheme is used [137]. However, an increased time step in the ADI scheme compromises the numerical accuracy rapidly [138, 139]. The envelope ADI-FDTD, presented in [140], has significantly improved the numerical accuracy for large time steps and is applicable for problems with harmonic carrier frequencies [141].

The approach pursued subsequently makes use of the multi-rate behavior of certain problems. A methodology that has been proven successful in multi-rate simulation of lumped circuits exhibiting strong nonlinearity is the multi-time partial differential equation (MPDE) method [142–146]. The reported success of the method makes it a promising candidate for use in multi-rate electromagnetic field simulations. To date no efforts have been reported on applying the method to the numerical simulation of distributed wave phenomena. This is examined for the first time in this work.

We will continue with an introduction to the MPDE method followed by a brief discussion of spectral methods which we will use for our MPDE problem. We will then discuss the MPDE for a one-dimensional EM problem. Next we will develop an MPDE formulation for the relevant problem, perform some numerical studies, and discuss the obtained results.

6.1 The Multi-Time Partial Differential Equation Solution Approach

As stated above, the numerical integration of differential algebraic equations for problems with widely separated time scales is computationally costly and possibly problematic due to numerical long-term instabilities. To demonstrate the benefits of the multi-time method we consider the two-tone problem

$$b(t) = \sin\left(\frac{2\pi}{T_1}t\right)\sin\left(\frac{2\pi}{T_2}t\right), \tag{6.1}$$

which contains one temporal scale at the frequency $f_1 = 1/T_1 = 1$ GHz and a second temporal scale at $f_2 = 1/T_2 = 10$ MHz. Hence, we have to choose a time step for our numerical integration small enough to resolve T_1 and yet an integration interval long

enough to capture T_2. The computational cost will scale according to

$$O\Big(N\frac{T_2}{T_1}\Big)\,, \tag{6.2}$$

where N is the number of sample points to resolve one period T_1. For the MPDE formulation (6.1) is reformulated as

$$\hat{b}(t_1,t_2) = \sin\Big(\frac{2\pi}{T_1}t_1\Big)\sin\Big(\frac{2\pi}{T_2}t_2\Big)\,, \tag{6.3}$$

where we use $\hat{}$ to denote a multi-time variable. The conversion from the representation by the time t to the multivariate representation by t_i, $i = \{1,2\}$, is obtained with help of the modulo-operator

$$t_i = t \bmod T_i\,, \tag{6.4}$$

hence $b(t) = \hat{b}(t \bmod T_1, t \bmod T_2)$. The multi-time function $\hat{b}$ is graphed in Figure 6.1. To recover the univariate representation we use (6.4) to follow a trace in the t_1-t_2 plane of Figure 6.1, as depicted in Figure 6.2. The recovered univariate function b is plotted in Figure 6.3. While the multivariate function, sampled with $N = 20$ points per time scale, is represented by a total of $N^2 = 400$ sample points, $N\,T_2/T_1 = 2000$ sample points are required for the univariate representation. Herein lies the advantage of the MPDE method. The relation between the MPDE method and the univariate PDE formulation will be discussed in more detail below following the discussion of the MPDE method in [144].

The MPDE method is applicable to problems with multirate behavior. A function

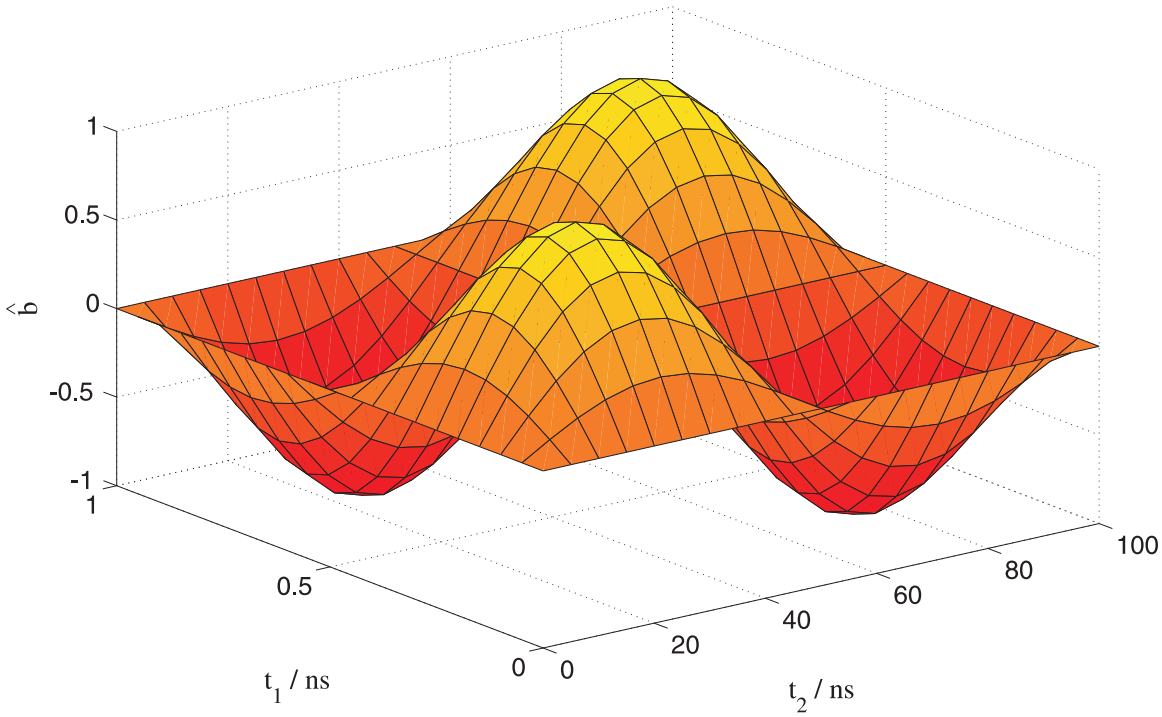

Figure 6.1: Multi-time function $\hat{b}$.

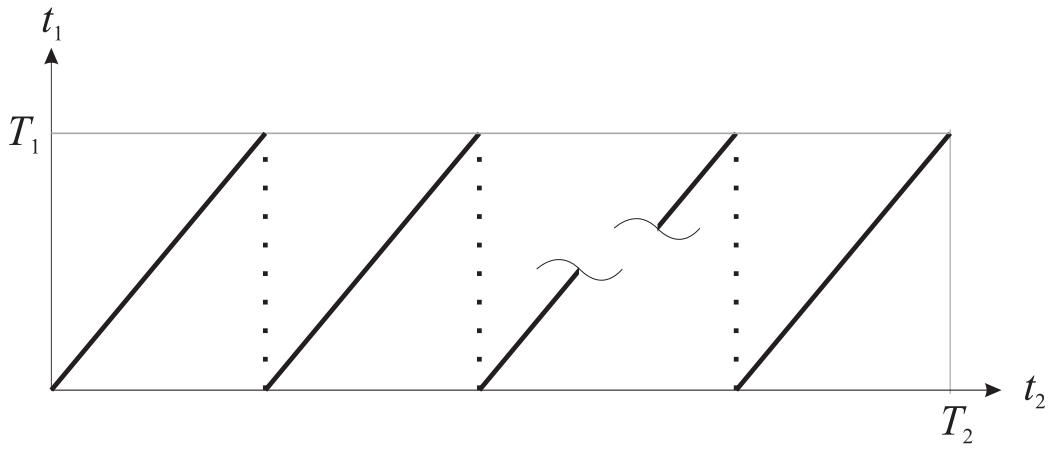

Figure 6.2: $t_1 - t_2$ plane.

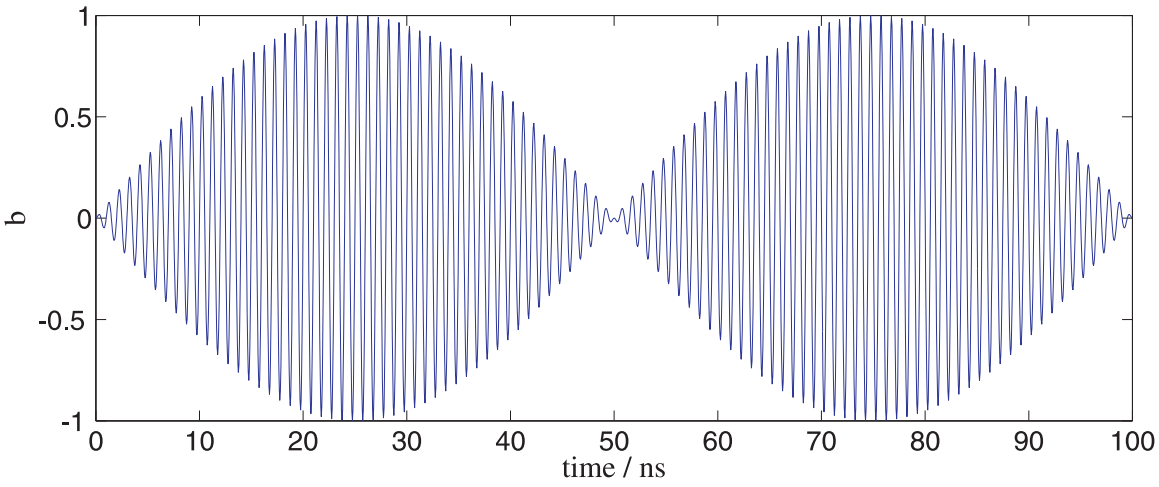

Figure 6.3: Univariate function b.

$x(t)$ is considered quasi-periodic if it can be expressed in the form

$$x(t) = \sum_{i_1=-\infty}^{+\infty} \cdots \sum_{i_m=-\infty}^{+\infty} X_{i_1,\ldots,i_m} e^{j2\pi(\frac{i_1}{T_1}+\cdots+\frac{i_m}{T_m})t}, \tag{6.5}$$

where $X_{i_1,\ldots,i_m}$ are real or complex valued constants. The multivariate function $\hat{x}(t_1,\ldots,t_m)$ is said to be m-periodic if real constants $T_1,\ldots,T_m$ exist such that

$$\hat{x}(t_1 + k_1T_1,\ldots,t_m + k_mT_m) = \hat{x}(t_1,\ldots,t_m) \tag{6.6}$$

for all integers $k_1,\ldots,k_m$ and all real $t_1,\ldots,t_m$. Furthermore, if any m-periodic function $\hat{x}(t_1,\ldots,t_m)$ is given, a quasi-periodic function x is obtained by

$$x(t) = \hat{x}(t + c_1,\ldots,t + c_m) \tag{6.7}$$

for any $c_1,\ldots,c_m$. This can be shown by expanding the multi-time function into a Fourier series

$$\hat{x}(t_1,\ldots,t_m) = \sum_{i_1=-\infty}^{+\infty} \cdots \sum_{i_m=-\infty}^{+\infty} X_{i_1,\ldots,i_m} e^{j2\pi(\frac{i_1t_1}{T_1}+\cdots+\frac{i_mt_m}{T_m})} \tag{6.8}$$

and then substituting $t_i = t + c_i$ within the Fourier series. Hence, $x(t)$ is obtained in the quasi-periodic form of (6.5)

$$x(t) = \sum_{i_1=-\infty}^{+\infty} \cdots \sum_{i_m=-\infty}^{+\infty} \left(X_{i_1,\ldots,i_m} e^{j2\pi(\frac{i_1 c_1}{T_1} + \cdots + \frac{i_m c_m}{T_m})} \right) e^{j2\pi(\frac{i_1}{T_1} + \cdots + \frac{i_m}{T_m})t} . \tag{6.9}$$

Above, we had an m-periodic function $\hat{x}$ and obtained the quasi-periodic function x. In reverse, an m-periodic function can be found that satisfies (6.7), given any m-tone quasi-periodic function x and any constants $c_1, \ldots, c_m$. This can be seen by the expansion of the quasi-periodic function x as in (6.5) and by the definition

$$\hat{x}(t_1, \ldots, t_m) = \sum_{i_1=-\infty}^{+\infty} \cdots \sum_{i_m=-\infty}^{+\infty} \left(X_{i_1,\ldots,i_m} e^{-j2\pi(\frac{i_1 c_1}{T_1} + \cdots + \frac{i_m c_m}{T_m})} \right) e^{j2\pi(\frac{i_1 t_1}{T_1} + \cdots + \frac{i_m t_m}{T_m})} , \tag{6.10}$$

which will satisfy (6.7).

With the above definitions and established relations in mind, we consider the univariate PDE of the form

$$\frac{\partial q(x(t))}{\partial t} = f(x(t)) + b(t) , \tag{6.11}$$

where all variables may be vector valued, except the time t. The related MPDE equation will be defined as

$$\frac{\partial q(\hat{x})}{\partial t_1} + \cdots + \frac{\partial q(\hat{x})}{\partial t_m} = f(\hat{x}) + \hat{b}(t_1, \ldots, t_m) . \tag{6.12}$$

If $\hat{x}(t_1, \ldots, t_m)$ and $\hat{b}(t_1, \ldots, t_m)$ satisfy (6.12), then $x(t) = \hat{x}(t + c_1, \ldots, t + c_m)$ and $b(t) = \hat{b}(t + c_1, \ldots, t + c_m)$ satisfy (6.11) for any fixed $c_1, \ldots, c_m$. This relation between

the PDE and the MPDE can be proven by

$$q(x(t)) = q(\hat{x}(t + c_1, \ldots, t + c_m)) \,, \tag{6.13}$$

$$\begin{aligned} \frac{\partial q(x(t))}{\partial t} &= \frac{\partial q(\hat{x}(t + c_1, \ldots, t + c_m))}{\partial t_1} + \cdots + \frac{\partial q(\hat{x}(t + c_1, \ldots, t + c_m))}{\partial t_m} \\ &= f(\hat{x}(t + c_1, \ldots, t + c_m)) + \hat{b}(\hat{x}(t + c_1, \ldots, t + c_m)) \\ &= f(x(t)) + b(t) \,. \end{aligned} \tag{6.14}$$

Hence, the solution to the PDE can be obtained from the solution to the MPDE by following certain straight lines in the solution domain spanned by the variables of dependence.

Furthermore, it can be shown that any periodic solution of the MPDE generates a quasi-periodic solution to the univariate PDE. This is termed the *MPDE sufficiency condition* and it states that if $\hat{x}$ is an m-periodic solution to (6.12) under the m-periodic excitation $\hat{b}$, then $x(t) = \hat{x}(t + c_1, \ldots, t + c_m)$ is an m-tone quasi-periodic solution to (6.11) under the m-tone quasi-periodic function $b(t) = \hat{b}(t+c_1, \ldots, t+c_m)$.

The *MPDE necessity condition*, on the other hand, states that if there is a quasi-periodic solution x to (6.11) for a quasi-periodic excitation b, then there is an m-periodic solution $\hat{x}$ for an m-periodic $\hat{b}$ for (6.12) such that $x(t) = \hat{x}(t+c_1, \ldots, t+c_m)$ and $b(t) = \hat{b}(t + c_1, \ldots, t + c_m)$ for any $c_1, \ldots, c_m$. Proofs for the MPDE sufficiency condition and the MPDE necessity condition can be found in [144].

The function $\hat{x}(t_1, \ldots, t_m)$ does not have to be m-periodic but may have only a $m - 1$ periodicity. In this case we have an envelope function of the form

$$\hat{x}(t_1, \ldots, t_m) = \sum_{i_2=-\infty}^{+\infty} \cdots \sum_{i_m=-\infty}^{+\infty} \left(X_{i_2,\ldots,i_m}(t_1) e^{j2\pi(\frac{i_2 t_2}{T_2} + \cdots + \frac{i_m t_m}{T_m})} \right) , \tag{6.15}$$

for which the MPDE method provides a unique solution, if periodic and initial bound-

ary conditions are enforced [144]. The periodic boundary conditions demand

$$\hat{x}(t_1, t_2 + T_2, \ldots, t_m + T_m) = \hat{x}(t_1, t_2, \ldots, t_m)\,, \tag{6.16}$$

and h defines the initial boundary condition

$$\hat{x}(0, t_2 + T_2, \ldots, t_m + T_m) = h(t_2, \ldots, t_m)\,. \tag{6.17}$$

6.2 Spectral Methods

Spectral methods provide the means to solve PDEs with high accuracy by transforming the function into the spectral domain and applying differential operators in this domain [147–150]. The spectral expansion functions, like Fourier series or Chebyshev expansion functions, achieve very good convergence of the finite approximation of the PDE solution to the actual solution for smooth problems. The high accuracy of spectral methods is a salient feature and it is referred to as *spectral accuracy*.

For the solution of PDEs by means of a spectral method we consider the periodic function $u(x)$, defined on $x = (0, 2\pi)$, and its spectral representation using the Fourier coefficients $\hat{u}_k$. The Fourier coefficients are obtained by the Fourier transform

$$\hat{u}_k = \frac{1}{2\pi} \int_0^{2\pi} u(x) e^{-jkx} dx\,, \qquad k = 0, \pm 1, \pm 2, \ldots\,, \tag{6.18}$$

and $u(x)$ is recovered from the Fourier series expansion

$$u(x) = \sum_{k=-\infty}^{+\infty} \hat{u}_k e^{jkx}\,. \tag{6.19}$$

In the spectral domain the n-th order partial derivative is found by

$$\frac{\partial^n u(x)}{\partial x^n} = \sum_{k=-\infty}^{+\infty} (jk)^n \hat{u}_k e^{jkx} \,. \tag{6.20}$$

For a continuously differentiable u we find for $k \neq 0$, using integration by parts

$$2\pi\hat{u}_k = \int_0^{2\pi} u(x) e^{-jkx} dx = \frac{-1}{jk}(u(2\pi^-) - u(0^+)) + \frac{1}{jk}\int_0^{2\pi} \frac{\partial u(x)}{\partial x} e^{-jkx} dx \,. \tag{6.21}$$

The decay of the Fourier coefficients $\hat{u}_k$ with growing k can be seen from the above equation for a one-time continuously differentiable function u. For an m-time continuously differentiable function u, where $\partial^n u/\partial x^n$ is periodic for all $n \leq m-2$, the decay is

$$\hat{u}_k = O(k^{-m}) \,, \qquad k = \pm 1, \pm 2, \dots \,, \tag{6.22}$$

where we use the Landau notation [151] to estimate the decay. *Spectral accuracy* refers to the fact that the k-th Fourier coefficient decays faster than any negative power of k for an infinitely differentiable function for which all its derivatives are periodic [148].

For comparison we consider the approximation error of the finite difference obtained by truncating the Taylor series expansion

$$u(x_i + \Delta x) = u(x_i) + \Delta x \frac{\partial u|_i}{\partial x} + \frac{(\Delta x)^2}{2!}\frac{\partial^2 u|_i}{\partial x^2} + \frac{(\Delta x)^3}{3!}\frac{\partial^3 u|_i}{\partial x^3} + \cdots \,. \tag{6.23}$$

Discretizing $u(x)$ on the interval $x = (0, 2\pi)$ with N points yields $\Delta x = 2\pi/N$ and

$$x_i = \frac{2\pi i}{N} \,, \qquad i = 0, ..., N-1 \,. \tag{6.24}$$

Hence the approximation error for $\partial u/\partial x$ will be $O(N^{-1})$. Using local interpolation

one can derive higher order finite difference schemes and hence, this error can be reduced to $O(N^{-m})$, where m is some constant which represents the order of approximation [149]. However, the decay of the spectral coefficients given in (6.22) is achieved for every m. Hence, the convergence of the numerical solution with the actual solution for the spectral method is outstanding provided the Fourier series expansion has not been truncated below an acceptable limit for k [148].

Upon discretizing the function u, the transformations of (6.18)-(6.19) between the physical and the spectral domain are found by the discrete Fourier transform (DFT)

$$\tilde{u}_k = \frac{1}{N} \sum_{j=0}^{N-1} u(x_i) e^{-jkx_i} \,, \qquad k = -N/2, ..., N/2 - 1 \,, \tag{6.25}$$

and the inverse discrete Fourier transform (IDFT)

$$u(x_i) = \sum_{k=-N/2}^{N/2-1} \tilde{u}_k e^{jkx_i} \,, \tag{6.26}$$

where N is assumed to be an even number here and in the following. To perform a differential operation on u in the physical domain a matrix operator can be introduced [148]. For this purpose we need an interpolant

$$I_N u(x) = \sum_{i=0}^{N-1} u(x_i) \psi_i(x) \,, \tag{6.27}$$

with

$$\psi_i(x) = \frac{1}{N} \sum_{i=-N/2}^{N/2} e^{jk(x-x_i)} \,. \tag{6.28}$$

The Fourier interpolation derivative $\mathcal{D}_N u$ is introduced as

$$\mathcal{D}_N u = \frac{\partial I_N u(x)}{\partial x} \tag{6.29}$$

along with the Fourier interpolation derivative matrix D_N, yielding

$$(\mathcal{D}_N u)_i = \sum_{l=0}^{N-1} (D_N)_{il} u_l \,. \tag{6.30}$$

The elements of D_N are derived as

$$(D_N)_{il} = \begin{cases} \frac{1}{2}(-1)^{j+l} \cot\left(\frac{(i-l)\pi}{N}\right) & i \neq l \\ 0 & i = l \end{cases}, \tag{6.31}$$

and for the second order derivative $D_N^{(2)}$ as

$$(D_N^{(2)})_{il} = \begin{cases} \frac{1}{4}(-1)^{i+l} N + \frac{(-1)^{i+l+1}}{2\sin^2\left(\frac{(i-l)\pi}{N}\right)} & i \neq l \\ -\frac{(N-1)(N-2)}{12} & i = l \end{cases}. \tag{6.32}$$

6.3 The MPDE Formulation for the One-Dimensional EM Wave Equation

In the following we consider a one-dimensional electromagnetic wave in a medium with time- and space-dependent variation of the electric permittivity and constant magnetic permeability. The reduced form of Maxwell's equations for the one-dimensional wave equation shall be

$$-\mu \frac{\partial H_y}{\partial t} = \frac{\partial E_x}{\partial z} \,, \tag{6.33}$$

$$\frac{\partial (\epsilon E_x)}{\partial t} = -\frac{\partial H_y}{\partial z} \,, \tag{6.34}$$

in the well known univariate formulation. For the following problem we will assume that the carrier frequency of the EM wave is high and hence its time scale is fast

compared to the time scale of the time-varying permittivity. We establish two time variables t_1 and t_2 following the MPDE method introduced in 6.1. The multivariate formulation of (6.33)-(6.34) is found to be

$$-\mu \frac{\partial \hat{H}_y}{\partial t_1} = \frac{\partial \hat{E}_x}{\partial z}\,, \tag{6.35}$$

$$\frac{\partial (\epsilon \hat{E}_x)}{\partial (t_1, t_2)} = -\frac{\partial \hat{H}_y}{\partial z}\,, \tag{6.36}$$

with $t_1 = m\Delta t_1$, $T_1 = M\Delta t_1$, $t_2 = n\Delta t_2$, and $T_2 = N\Delta t_2$. Since the permittivity ϵ has no variation with t_1, (6.36) can be written as

$$\epsilon \frac{\partial \hat{E}_x}{\partial t_1} + \frac{\partial \epsilon}{\partial t_2}\hat{E}_x + \epsilon \frac{\partial \hat{E}_x}{\partial t_2} = -\frac{\partial \hat{H}_y}{\partial z}\,. \tag{6.37}$$

6.4 A TD Envelope Integration Scheme for the MPDE

A numerical scheme to solve the one-dimensional multi-time EM wave equation with time- and space-varying permittivity is developed in this section. We use a time domain envelope scheme as discussed in Section 6.1. For the electric and magnetic field values we use the notation

$$\hat{E}_{x,j}^{m,n} = \hat{E}_x(m\Delta t_1, n\Delta t_2, j\Delta z + 1/2)\,, \tag{6.38}$$

$$\hat{H}_{y,j}^{m,n} = \hat{H}_y(m\Delta t_1, (n+1/2)\Delta t_2, j\Delta z)\,, \tag{6.39}$$

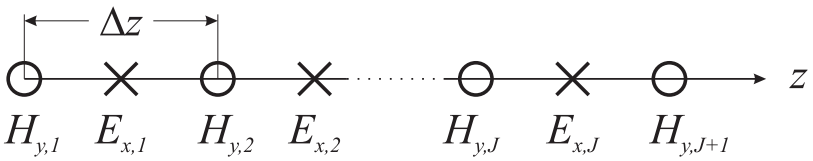

Figure 6.4: Spatial discretization of 1D EM wave.

and

$$\hat{\boldsymbol{E}}_x^{m,n} = \left[\hat{E}_{x,1}^{m,n} \cdots \hat{E}_{x,J}^{m,n}\right]^T, \tag{6.40}$$

$$\hat{\boldsymbol{H}}_y^{m,n} = \left[\hat{H}_{y,1}^{m,n} \cdots \hat{H}_{y,J+1}^{m,n}\right]^T. \tag{6.41}$$

The wave equation is solved for $z = [0, L]$, with $L = (J+1)\Delta z$, where Δz is the space increment and J the number of spatial sample points for the electric field. The spatial sampling scheme is depicted in Figure 6.4. For the spatiotemporally varying permittivity we assume a harmonic variation of the form

$$\epsilon(t_2, z) = \epsilon_0(\epsilon_m + \epsilon_v \sin(2\pi t_2/T_2 - z\kappa)). \tag{6.42}$$

The short notation for its discretization will be

$$\epsilon_j^n = \epsilon(n\Delta t_2, (j+1/2)\Delta z). \tag{6.43}$$

Using these definitions and the spectral differentiation scheme of (6.31), we discretize (6.35) and (6.37), applying an implicit backward Euler scheme,

$$\frac{\partial \epsilon}{\partial t_2}\hat{E}_x^{m,n+1} + \epsilon\frac{2\pi}{T_1}(\mathcal{D}_M)_{mm}\hat{E}_x^{m,n+1} + \frac{\epsilon\hat{E}_x^{m,n+1} - \epsilon\hat{E}_x^{m,n}}{\Delta t_2} = -\frac{\hat{H}_{y,j+1}^{m,n+1} - \hat{H}_{y,j}^{m,n+1}}{\Delta z}, \tag{6.44}$$

$$-\mu\Big(\frac{2\pi}{T_1}(\mathcal{D}_M)_{mm}\hat{H}_y^{m,n+1} + \frac{\hat{H}_y^{m,n+1} - \hat{H}_y^{m,n}}{\Delta t_2}\Big) = \frac{\hat{E}_{x,j}^{m,n+1} - \hat{E}_{x,j-1}^{m,n+1}}{\Delta z}. \tag{6.45}$$

Upon rearranging the finite MPDEs we obtain

$$\hat{E}_{x,j}^{m,n} = (1 + \frac{\Delta t_2}{\epsilon_j^n}(\frac{\partial \epsilon_j^n}{\partial t_2} + \epsilon_j^n \frac{2\pi}{T_1}(\mathcal{D}_M)_{mm}))\hat{E}_{x,j}^{m,n+1} + \frac{\Delta t_2}{\epsilon_j^n \Delta z}(\hat{H}_{y,j+1}^{m,n+1} - \hat{H}_{y,j}^{m,n+1}), \quad (6.46)$$

$$\hat{H}_{y,j}^{m,n} = (1 + \Delta t_2 \frac{2\pi}{T_1}(\mathcal{D}_M)_{mm})\hat{H}_{y,j}^{m,n+1} + \frac{\Delta t_2}{\mu \Delta z}(\hat{E}_{x,j}^{m,n+1} - \hat{E}_{x,j-1}^{m,n+1}). \quad (6.47)$$

The wave is excited at $z = 0$ and terminated with a fixed resistive load at $z = L$. Thus we implement the following boundary conditions:

$$\hat{H}_{y,1}^{m,n} = (1 + \Delta t_2 \frac{2\pi}{T_1}(\mathcal{D}_M)_{mm})\hat{H}_{y,1}^{m,n+1} + \frac{\Delta t_2}{\mu \Delta z}(\hat{E}_{x,1}^{m,n+1} - \hat{E}_{src}^{m,n+1}), \quad (6.48)$$

$$\hat{H}_{y,J+1}^{m,n} = (1 + \Delta t_2 \frac{2\pi}{T_1}(\mathcal{D}_M)_{mm})\hat{H}_{y,J+1}^{m,n+1} + \frac{2\Delta t_2}{\mu \Delta z}(Z\hat{H}_{y,J+1}^{m,n+1} - \hat{E}_{x,J}^{m,n+1}), \quad (6.49)$$

where $\hat{E}_{src}^{m,n}$ is the source term and Z is the impedance

$$Z = \sqrt{\frac{\mu}{\epsilon_0 \epsilon_m}}. \quad (6.50)$$

We define the vector $\boldsymbol{X}^n$ containing all the electric and magnetic field samples in $z = [0, L]$, $t_1 = [0, T_1]$ at the time $t_2 = n\Delta t_2$ as

$$\boldsymbol{X}^n = \begin{pmatrix} \begin{bmatrix} \hat{\boldsymbol{E}}_x^{1,n} \\ \vdots \\ \hat{\boldsymbol{E}}_x^{M,n} \end{bmatrix}^{[J \cdot M]} \\ \begin{bmatrix} \hat{\boldsymbol{H}}_y^{1,n} \\ \vdots \\ \hat{\boldsymbol{H}}_y^{M,n} \end{bmatrix}^{[(J+1) \cdot M]} \end{pmatrix}. \quad (6.51)$$

The MPDE in the discretized form of (6.46)-(6.49) yields the time marching update equation

$$\boldsymbol{X}^{n+1} = (\boldsymbol{\Lambda}^{n+1})^{-1}\boldsymbol{X}^{n} + \boldsymbol{G}^{n+1}\,. \tag{6.52}$$

$\boldsymbol{G}^{n}$ is the source term described by

$$\boldsymbol{G}^{n} = \frac{\Delta t_2}{\mu\Delta z}\big[\underbrace{0\cdots0}_{J\cdot M}\big|\underbrace{\hat{E}^{1,n}_{src}\,0\cdots0}_{J+1}\big|\underbrace{\hat{E}^{2,n}_{src}\,0\cdots0}_{J+1}\big|\cdots\big|\underbrace{\hat{E}^{M,n}_{src}\,0\cdots0}_{J+1}\big]^{T}. \tag{6.53}$$

For establishing $\boldsymbol{\Lambda}^{n}$ in (6.52) we define

$$\mathbf{A}^{n} = \begin{bmatrix} 1+\frac{\Delta t_2}{\epsilon_1^n}\frac{\partial\epsilon_1^n}{\partial t_2} & 0 & 0 \\ 0 & \ddots & 0 \\ 0 & 0 & 1+\frac{\Delta t_2}{\epsilon_J^n}\frac{\partial\epsilon_J^n}{\partial t_2} \end{bmatrix}^{J\times J}, \tag{6.54}$$

$$\mathbf{B}^{n} = \frac{\Delta t_2}{\Delta z}\begin{bmatrix} -1/\epsilon_1^n & 1/\epsilon_1^n & 0 & 0 \\ 0 & \ddots & \ddots & 0 \\ 0 & 0 & -1/\epsilon_J^n & 1/\epsilon_J^n \end{bmatrix}^{J\times(J+1)}, \tag{6.55}$$

$$\mathbf{C} = \frac{\Delta t_2}{\mu\Delta z}\begin{bmatrix} 1 & 0 & 0 & 0 \\ -1 & 1 & \ddots & 0 \\ 0 & \ddots & \ddots & 0 \\ 0 & \ddots & -1 & 1 \\ 0 & 0 & 0 & -2 \end{bmatrix}^{(J+1)\times J}, \tag{6.56}$$

and

$$\mathbf{D} = \begin{bmatrix} 1 & 0 & 0 & 0 \\ 0 & 1 & \ddots & 0 \\ 0 & \ddots & \ddots & 0 \\ 0 & 0 & 0 & (1+\frac{2\Delta t_2}{\mu \Delta z} Z) \end{bmatrix}^{(J+1)\times(J+1)} . \tag{6.57}$$

Hence, we find $\mathbf{\Lambda}^n$ to be

$$\mathbf{\Lambda}^n = \left(\begin{bmatrix} \mathbf{A}^n & 0 & 0 \\ 0 & \ddots & 0 \\ 0 & 0 & \mathbf{A}^n \end{bmatrix} \begin{bmatrix} \mathbf{B}^n & 0 & 0 \\ 0 & \ddots & 0 \\ 0 & 0 & \mathbf{B}^n \end{bmatrix} \right) + \left(\begin{bmatrix} \mathbf{C} & 0 & 0 \\ 0 & \ddots & 0 \\ 0 & 0 & \mathbf{C} \end{bmatrix} \begin{bmatrix} \mathbf{D} & 0 & 0 \\ 0 & \ddots & 0 \\ 0 & 0 & \mathbf{D} \end{bmatrix} \right) +$$

$$+ \Delta t_2 \left(\begin{bmatrix} (\mathcal{D}_M)_{11}\mathbf{I} & \cdots & (\mathcal{D}_M)_{1M}\mathbf{I} \\ \vdots & \ddots & \vdots \\ (\mathcal{D}_M)_{M1}\mathbf{I} & \cdots & (\mathcal{D}_M)_{MM}\mathbf{I} \end{bmatrix} \begin{bmatrix} 0 & 0 & 0 \\ 0 & \ddots & 0 \\ 0 & 0 & 0 \end{bmatrix} \right) \left(\begin{bmatrix} 0 & 0 & 0 \\ 0 & \ddots & 0 \\ 0 & 0 & 0 \end{bmatrix} \begin{bmatrix} (\mathcal{D}_M)_{11}\mathbf{I} & \cdots & (\mathcal{D}_M)_{1M}\mathbf{I} \\ \vdots & \ddots & \vdots \\ (\mathcal{D}_M)_{M1}\mathbf{I} & \cdots & (\mathcal{D}_M)_{MM}\mathbf{I} \end{bmatrix} \right) . \tag{6.58}$$

6.5 Numerical Results

In this section we present numerical studies of the formulation developed in Section 6.4. We will consider the one-dimensional problem of (6.35)-(6.37) with a spatiotemporal dependence of the permittivity with traveling-wave-like behavior as in (6.42) and

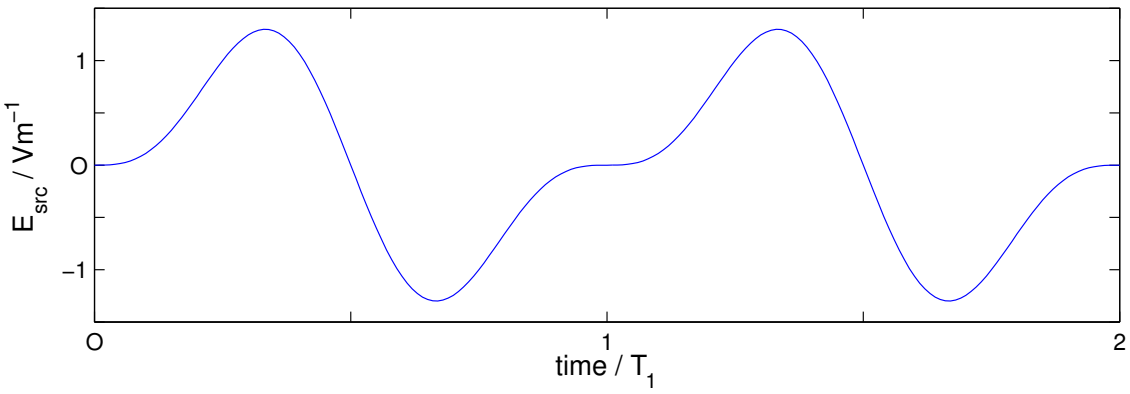

Figure 6.5: Excitation signal with $E_0 = 1$.

with standing-wave-like behavior, and we consider a problem with a time-dependent load impedance while the permittivity will be constant.

6.5.1 Case study (I)

In our first example we assume a permittivity $\epsilon = \epsilon_0 \epsilon_m$ which is constant over space and time. The relative permittivity is $\epsilon_m = 4.5$. We will consider a time-dependent termination of the form

$$Z_L(t_2) = (6 + 5\sin(2\pi t_2/T_2))\sqrt{\frac{\mu}{\epsilon_0 \epsilon_m}} \tag{6.59}$$

at $z = L$. The domain has a matched termination at $z = 0$. The excitation signal, plotted in Figure 6.5 for $E_0 = 1$, is described by

$$E_{src}(t) = E_0\Big(\sin(2\pi f_1 t) - \frac{1}{2}\sin(4\pi f_1 t)\Big)\,\mathrm{Vm}^{-1}\,. \tag{6.60}$$

The domain is excited at $z = \Delta z$ by the input signal E_{src} with $E_0 = 2$. Furthermore $f_1 = 10$ MHz, $f_2 = 100$ kHz, $L = 20$ m, and $M = 18$, with $M = T_1/\Delta t_1$. The parameters are summarized in Table 6.1. The boundary conditions and source implementation previously defined in (6.48)-(6.49) are modified, for this example only,

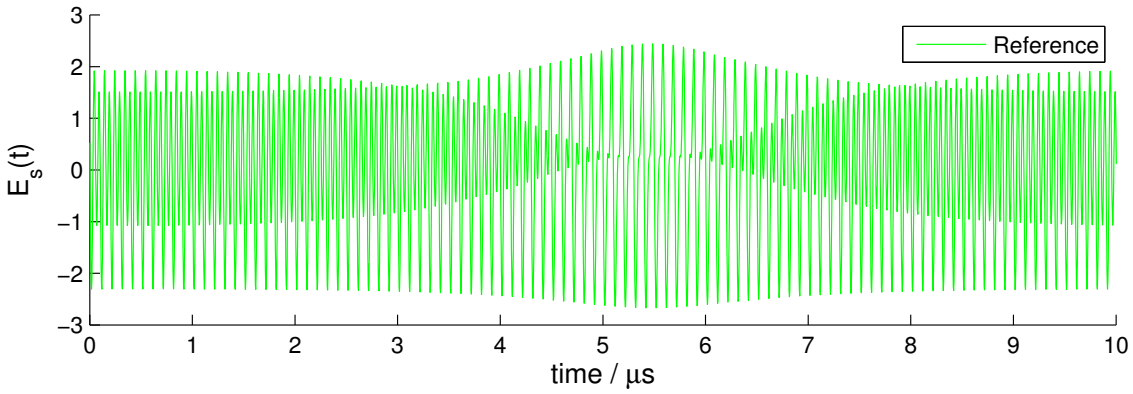

Figure 6.6: Reference solution for E_s for Case (I).

Table 6.1: Summary of the parameters of the MPDE case studies.

Case	f_1	f_2	f_1/f_2	ϵ	Z_L	L	L_m	v_{ph}	Δz
(I)	10 MHz	100 kHz	10^2	const.	$Z_L(t)$	20 m	–	–	~ 0.7 m
(II)	10 MHz	100 kHz	10^2	$\epsilon(t,z)$	const.	20 m	4 m	–	~ 0.6 m
(III)	10 MHz	100 kHz	10^2	$\epsilon(t,z)$	const.	20 m	4 m	10^5 m/s	~ 0.6 m
(IV)	10 MHz	1 kHz	10^4	$\epsilon(t,z)$	const.	20 m	10 m	10^4 m/s	1.0 m

to be

$$\hat{H}_{y,1}^{m,n} = (1 + \Delta t_2 \frac{2\pi}{T_1}(\mathcal{D}_M)_{mm})\hat{H}_{y,1}^{m,n+1} + \frac{2\Delta t_2}{\mu \Delta z}(\hat{E}_{x,1}^{m,n+1} + \hat{E}_{src}^{m,n+1} + Z\hat{H}_{y,1}^{m,n+1}), \tag{6.61}$$

$$\hat{H}_{y,2}^{m,n} = (1 + \Delta t_2 \frac{2\pi}{T_1}(\mathcal{D}_M)_{mm})\hat{H}_{y,2}^{m,n+1} + \frac{\Delta t_2}{\mu \Delta z}(\hat{E}_{x,2}^{m,n+1} + \hat{E}_{src}^{m,n+1} - \hat{E}_{x,1}^{m,n+1}), \tag{6.62}$$

$$\hat{H}_{y,J+1}^{m,n} = (1 + \Delta t_2 \frac{2\pi}{T_1}(\mathcal{D}_M)_{mm})\hat{H}_{y,J+1}^{m,n+1} + \frac{2\Delta t_2}{\mu \Delta z}(Z_L^n \hat{H}_{y,J+1}^{m,n+1} - \hat{E}_{x,J}^{m,n+1}), \tag{6.63}$$

where Z is defined in (6.50) and $Z_L^n = Z_L(n\Delta t_2)$ in (6.59). Using these source and boundary conditions, the definitions of (6.53), (6.56), and (6.57) are updated accordingly for our MPDE scheme. The signal is sampled close to $z = L$. This sampled signal is denoted as $\hat{E}_s(t_1, t_2)$. A reference solution is computed for the univariate problem using the Yee FDTD scheme. The reference solution is graphed in Figure 6.6. The time resolution Δt_1 in the MPDE scheme is approximately twice

the time step Δt of the reference solution. For the non-periodic, slow time scale t_2, the solution of the MPDE is propagated with a time step which is an integer multiple of Δt_1, hence $\Delta t_2 = q\Delta t_1$, $q = \{1, 2, 3, \dots\}$. Figure 6.7 shows the results computed with the MPDE scheme for $q = 100$. The solutions of the MPDE scheme are in very good agreement with the reference solution. The computation time for the MPDE scheme is reduced to 14% of that of the reference solution for the configuration stated above. Hence, we can achieve significant speedup in the computation time while maintaining good accuracy of the results.

6.5.2 Case study (II)

In our next example we assume a permittivity which has a space and time dependence described by

$$\epsilon(t_2, z) = \epsilon_0(\epsilon_m + \epsilon_v \sin(2\pi t_2/T_2)\sin(z\kappa))\,. \tag{6.64}$$

The relative permittivity is $\epsilon_m = 4.5$. While we had time-dependent termination of the simulation domain in the previous case, we now have a constant termination of $Z = \sqrt{\mu/(\epsilon\epsilon_m)}$ at $z = L$. The excitation signal is that of (6.60) with $E_0 = 1$. Furthermore $f_1 = 10$ MHz, $f_2 = 100$ kHz, $L = 20$ m, $\kappa = 2\pi/L_m$, $L_m = 4$ m, and $M = 34$. The parameters are summarized in Table 6.1 under Case (II).

The explicit Yee FDTD reference solution is graphed in Figure 6.8. The time resolution Δt_1 in the MPDE scheme is the same as the time step Δt of the reference solution. Figure 6.9 shows the results computed with the MPDE scheme for $\Delta t_2 = q\Delta t_1$, with $q = 100$. Again, the solutions of the MPDE scheme are in very good agreement with the reference solution. The computation time is reduced to 33% compared to the computation time of the reference solution.

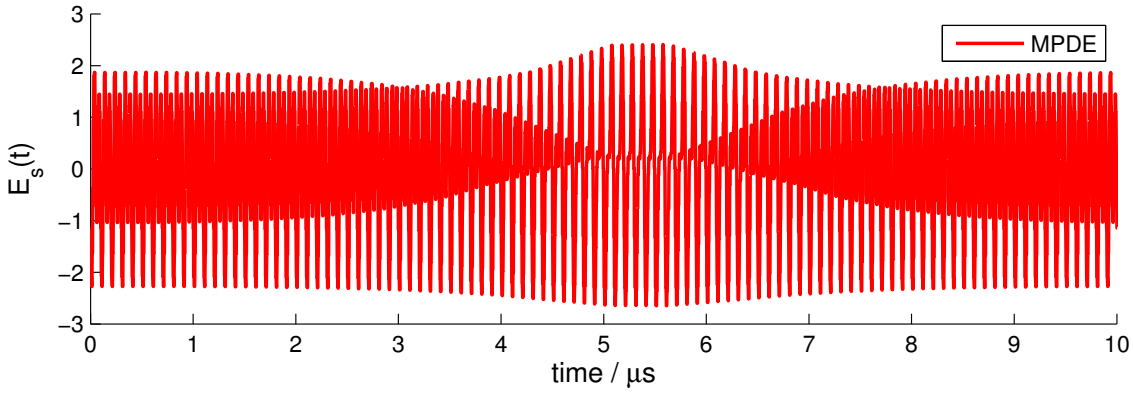

(a) $E_s(t)$ signal amplitude of MPDE solution

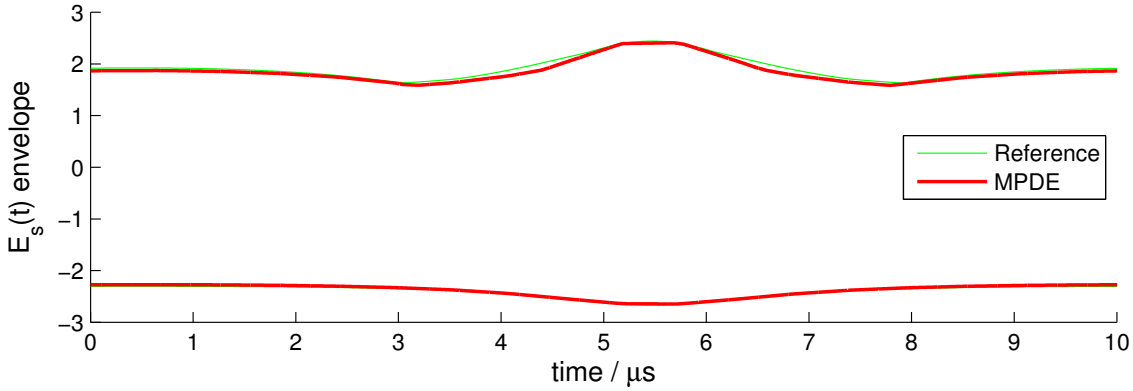

(b) $E_s(t)$ envelope for MPDE and reference FDTD solution

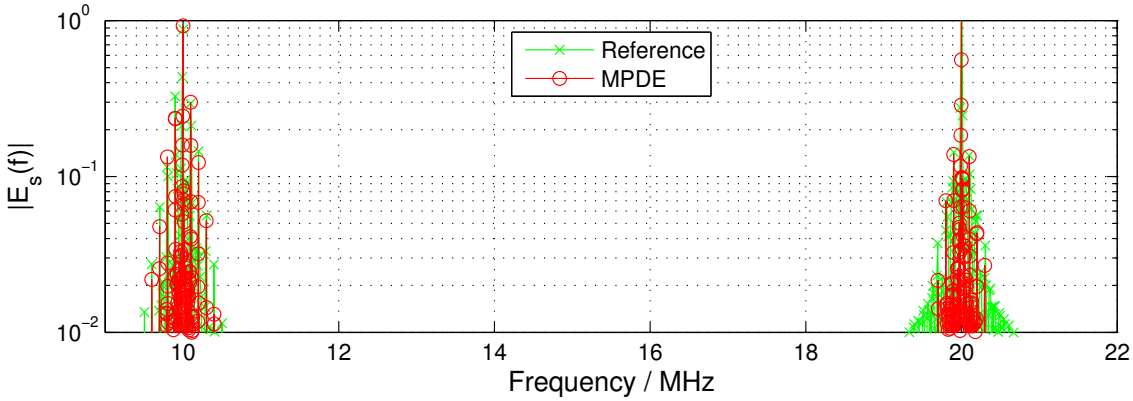

(c) $|E_s(f)|$ amplitude spectra

Figure 6.7: MPDE solution for Case (I) with time-dependent termination Z_L^n and constant permittivity, with $\Delta t_2 = 100\Delta t_1$, $M = 18$.

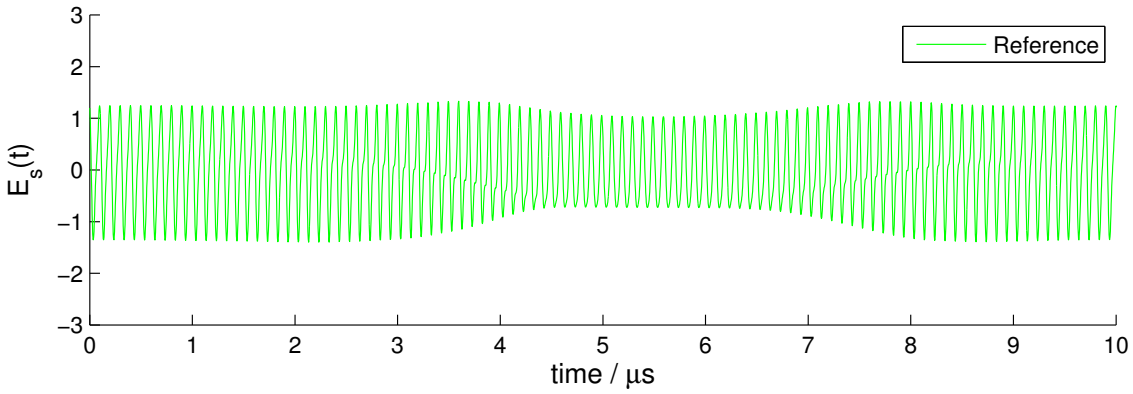

Figure 6.8: Reference solution for E_s for Case (II).

6.5.3 Case study (III)

For the permittivity variation of (6.42) we choose $\epsilon_m = 4.5$, $\epsilon_v = 2$, and $\kappa = 2\pi/L_m$. While these parameters will be the same for the case studies (III) and (IV), the remaining parameters will vary. The fast and the slow time scale have the frequencies $f_1 = 10$ MHz and $f_2 = 100$ kHz respectively. The length L of the line is 20 m and the wave length for the permittivity variation is $L_m = 20$ m. The spatial resolution is $\Delta z \approx 0.6$ m. The excitation signal is the one of (6.60) with $E_0 = 1$. The reference solution is computed for the univariate problem using the Yee FDTD scheme. The time step Δt for this solution is selected such that it satisfies the CFL condition (2.19). For the multi-time PDE we choose Δt_1 to be equal the time increment Δt of the univariate case. We have $T_1 = M\Delta t_1$ and for our case $M = 34$. These parameters are summarized in Table 6.1 under Case (III). The permittivity variation is described by a traveling wave with the phase velocity $v_{ph} = 10^5$ ms^{-1}. The amplitude of the sampled signal of the reference solution is graphed in Figure 6.10. The bivariate sampling signal $\hat{E}_s$ in the $t_1 - t_2$ plane, obtained from the solution to the MPDE equation with $\Delta t_2 = q\Delta t_1$ and $q = 20$, is shown in Figure 6.11. Subsequently, E_s in its univariate form is obtained along diagonal lines in the two-dimensional time plane, using linear interpolation for the values off the node points. We have solved the MPDE

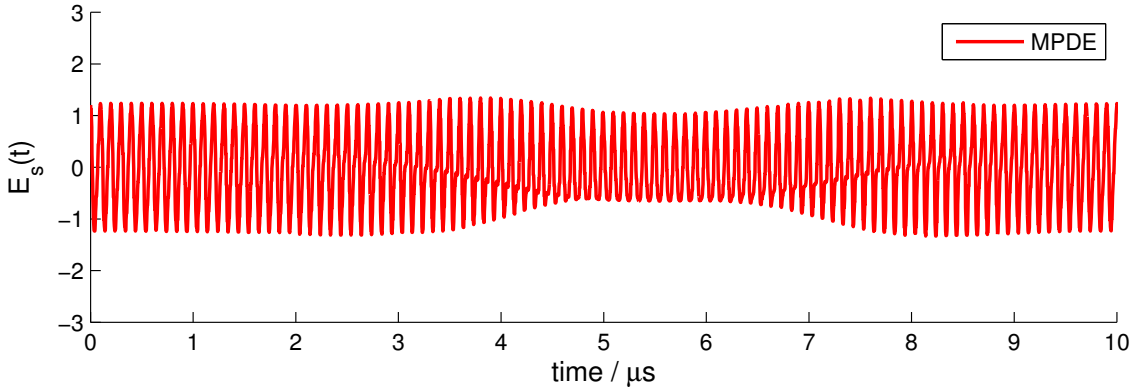

(a) $E_s(t)$ signal amplitude of MPDE solution

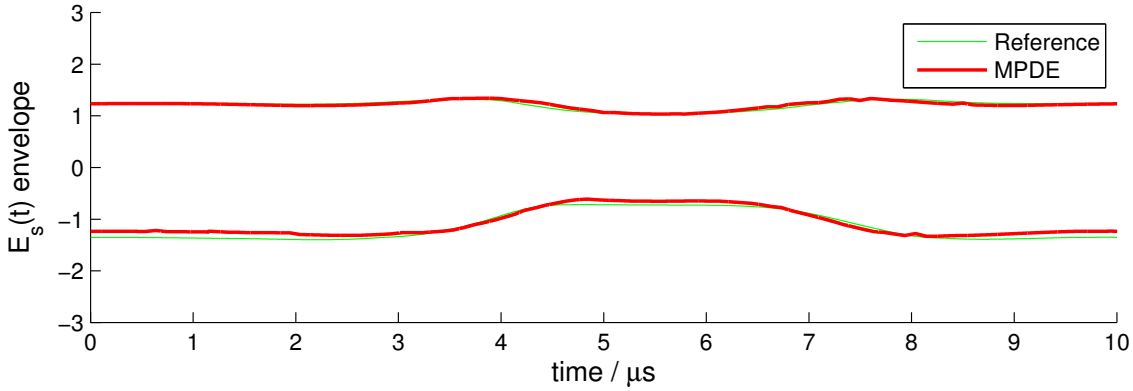

(b) $E_s(t)$ envelope for MPDE and reference FDTD solution

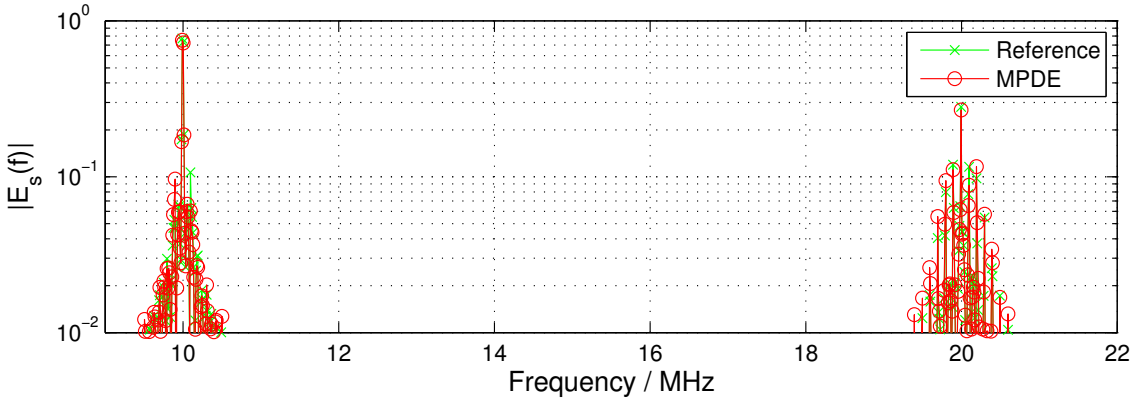

(c) $|E_s(f)|$ amplitude spectra

Figure 6.9: MPDE solution for Case (II) with $\Delta t_2 = 100\Delta t_1$, $M = 34$.

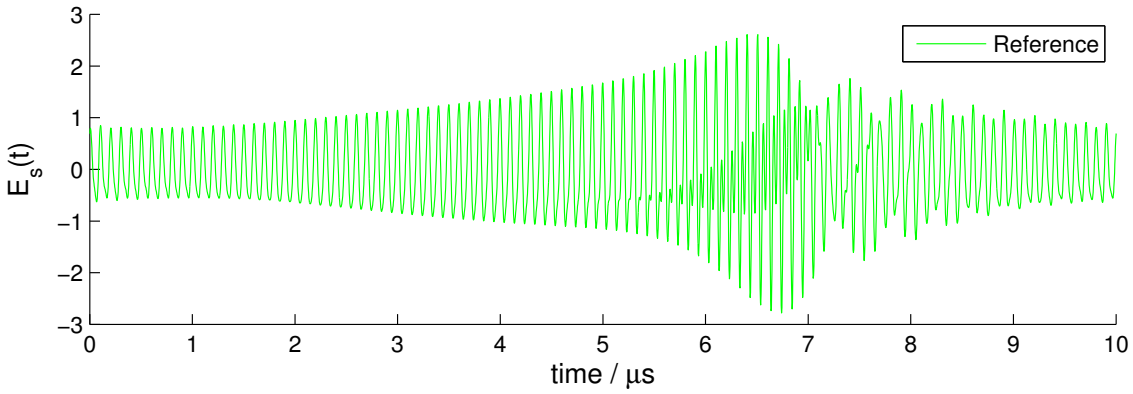

Figure 6.10: Reference solution for E_s for Case (III).

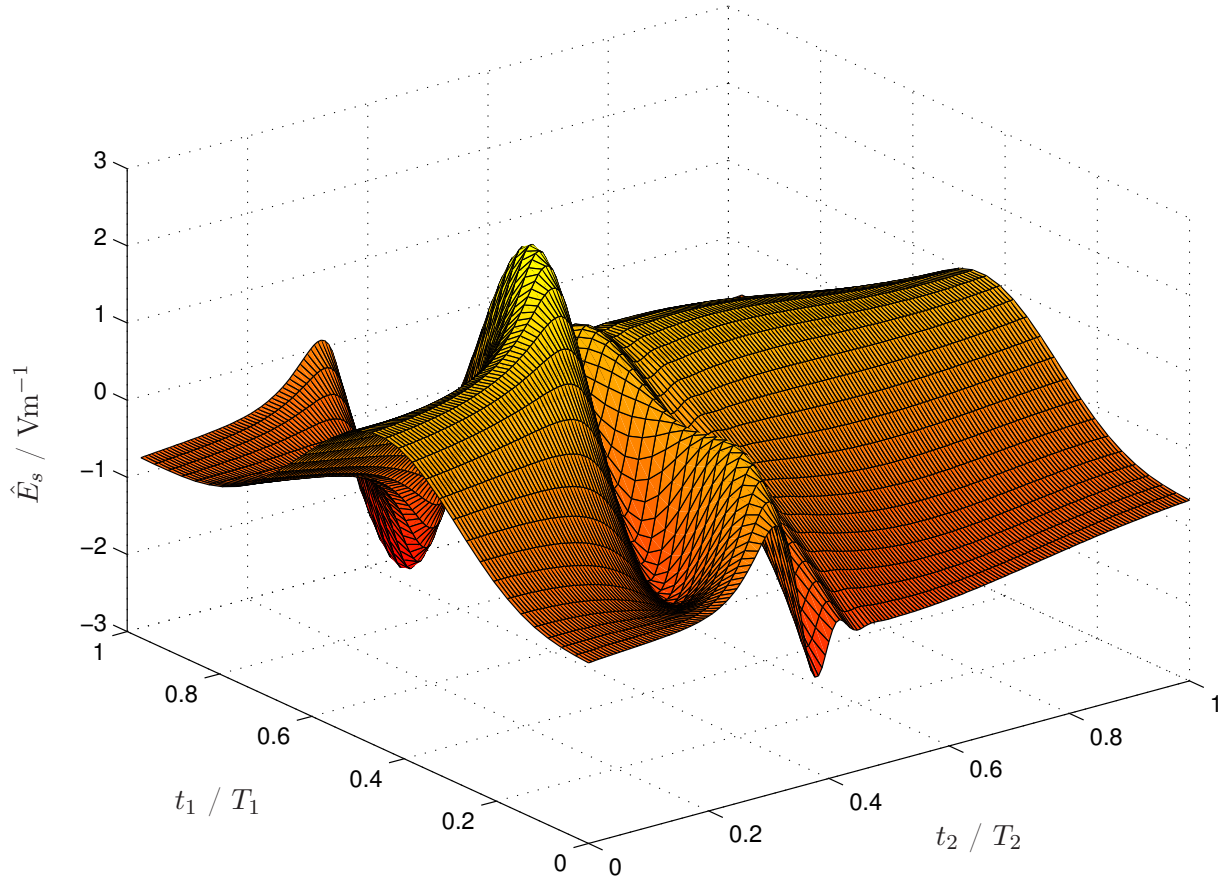

Figure 6.11: Sampled signal $\hat{E}_s$ in the $t_1 - t_2$ plane, with $q = 20$, $M = 34$ for Case (III).

scheme for several values of q. The results for $q = 4$, $q = 10$, $q = 50$, and $q = 100$ are plotted in Figures 6.12-6.15. The figures show the recovered univariate amplitude of E_s, the envelope of E_s for the respective MPDE solution compared to the envelope of the reference solution, and the amplitude spectrum of E_s of the MPDE and reference solution. We can observe good agreement of the MPDE result to the univariate PDE reference solution for small values of q and a slow degradation of the agreement as q is increased. A comparison of the spectra shows good agreement, too. The spectral spacing Δf of the intermodulation frequencies is found to be 100 kHz, hence in agreement with the permittivity variation at f_2. For higher q, the intermodulation products attenuate faster. The imbalance of the intermodulation levels around the base frequencies f_1 and $2f_1$, i.e. the fact that the intermodulation levels are higher for frequencies smaller than f_1 and $2f_1$ respectively, is due to the propagation direction of the wave describing the permittivity variation. For the permittivity variation

$$\epsilon(t_2, z) = \epsilon_0(\epsilon_m + \epsilon_v \sin(2\pi t_2/T_2 + z\kappa)) \tag{6.65}$$

this will reverse, as shown in Figure 6.16, for a simulation with $q = 50$ and parameters otherwise identical to the previous simulation.

The computation of the MPDE scheme and of the reference solution has been performed using MATLAB.[1] The ratio of the computation time on our computer for the MPDE solution to that for the reference solution is plotted in Figure 6.17. A gain in speed for the MPDE method is achieved with increasing q. For the above example the MPDE is faster than the univariate reference method for $q \geq 42$. However, for this comparison the time step Δt_1 was chosen to be the same in the MPDE method and in the reference solution. Since our MPDE scheme is, unlike the scheme used

[1]MATLAB, The MathWorks, Inc., 3 Apple Hill Dr., Natick, MA 01760-2098, U.S.A., `http://www.mathworks.com`

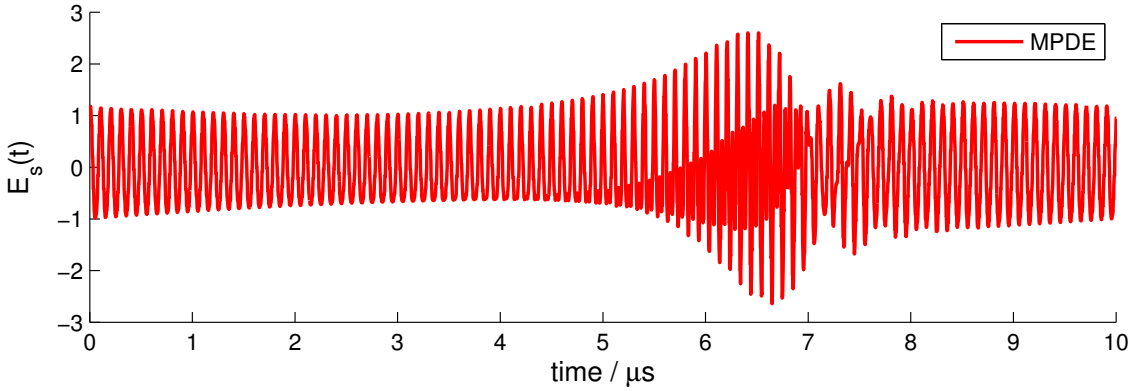

(a) $E_s(t)$ signal amplitude of MPDE solution

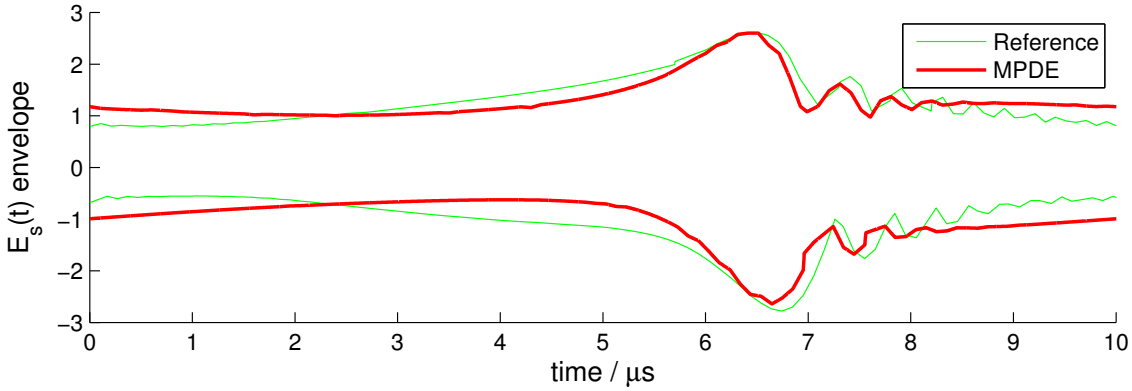

(b) $E_s(t)$ envelope for MPDE and reference FDTD solution

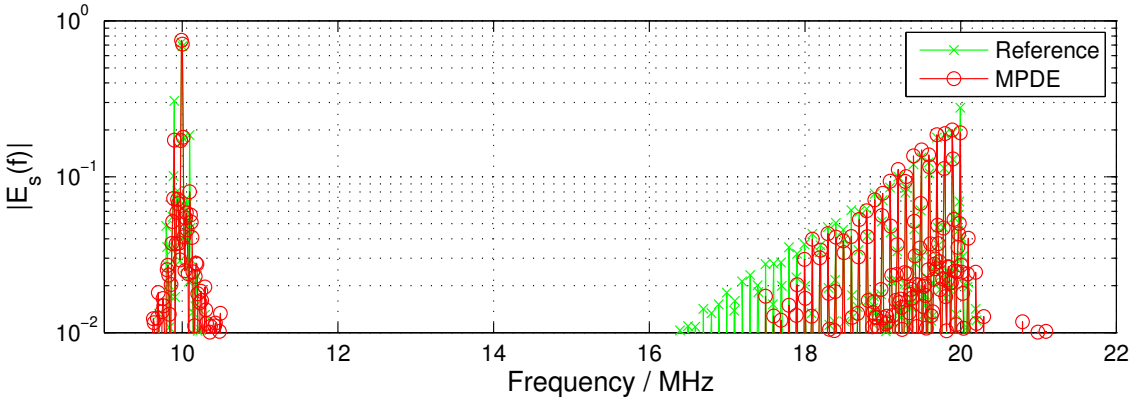

(c) $|E_s(f)|$ amplitude spectra

Figure 6.12: MPDE solution for Case (III) with $\Delta t_2 = 4\Delta t_1$, $M = 34$.

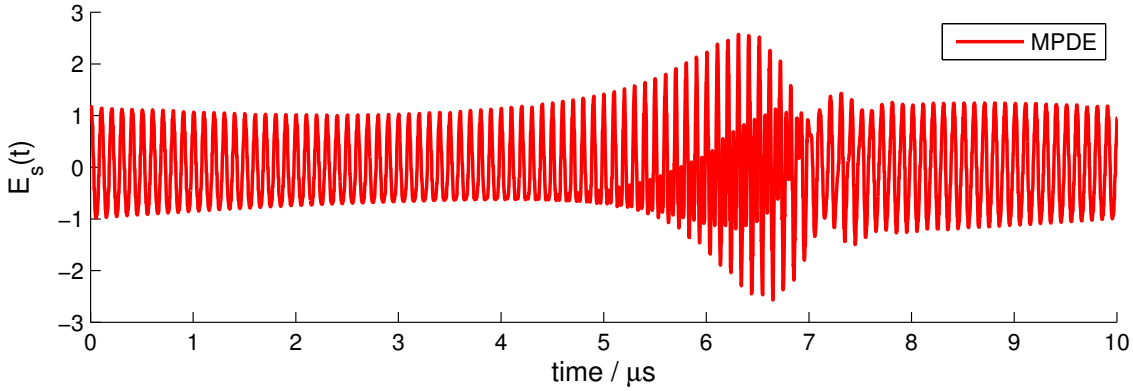

(a) $E_s(t)$ signal amplitude of MPDE solution

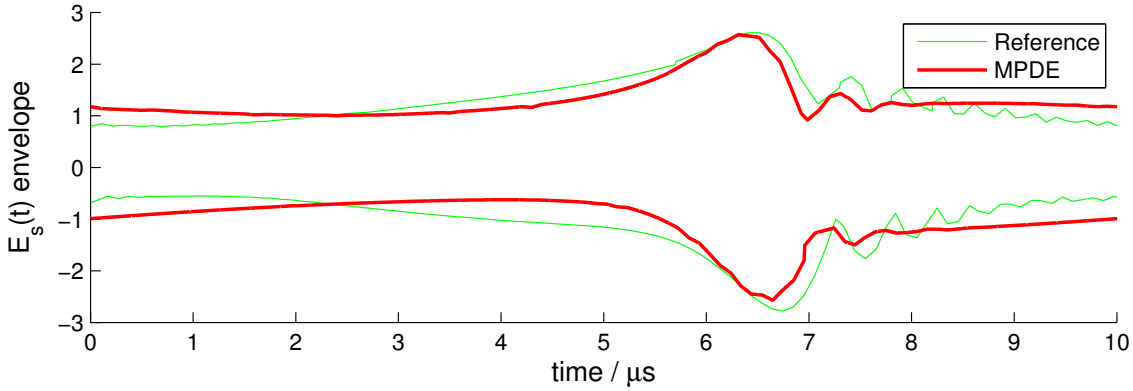

(b) $E_s(t)$ envelope for MPDE and reference FDTD solution

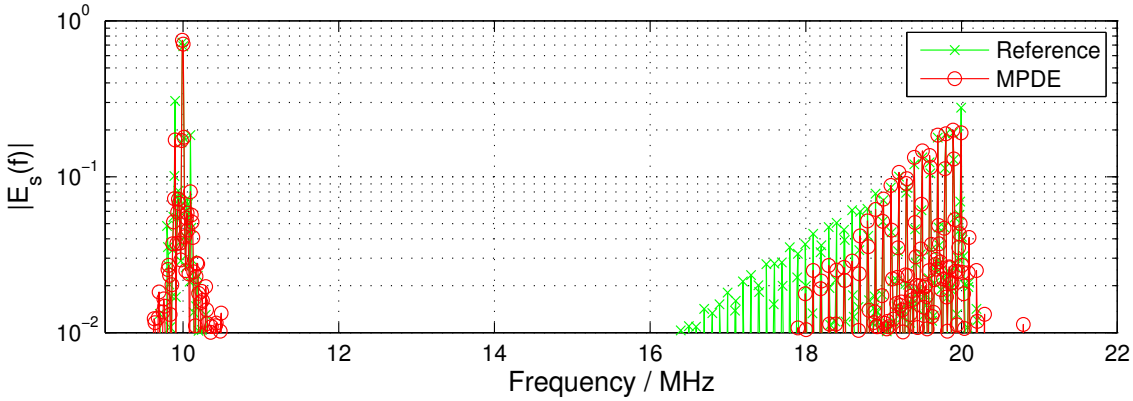

(c) $|E_s(f)|$ amplitude spectra

Figure 6.13: MPDE solution for Case (III) with $\Delta t_2 = 10\Delta t_1$, $M = 34$.

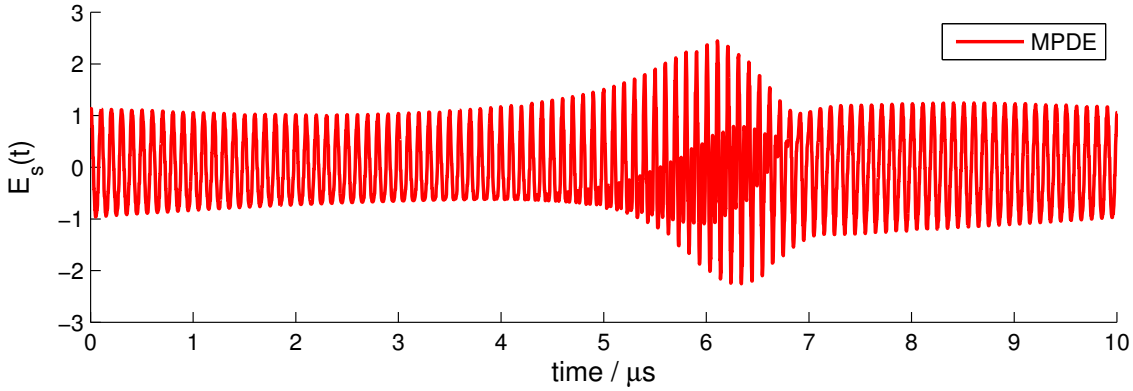

(a) $E_s(t)$ signal amplitude of MPDE solution

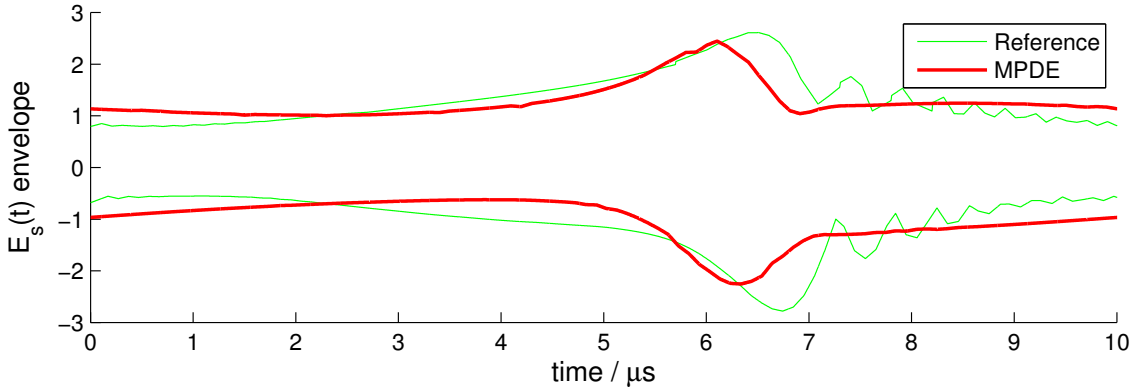

(b) $E_s(t)$ envelope for MPDE and reference FDTD solution

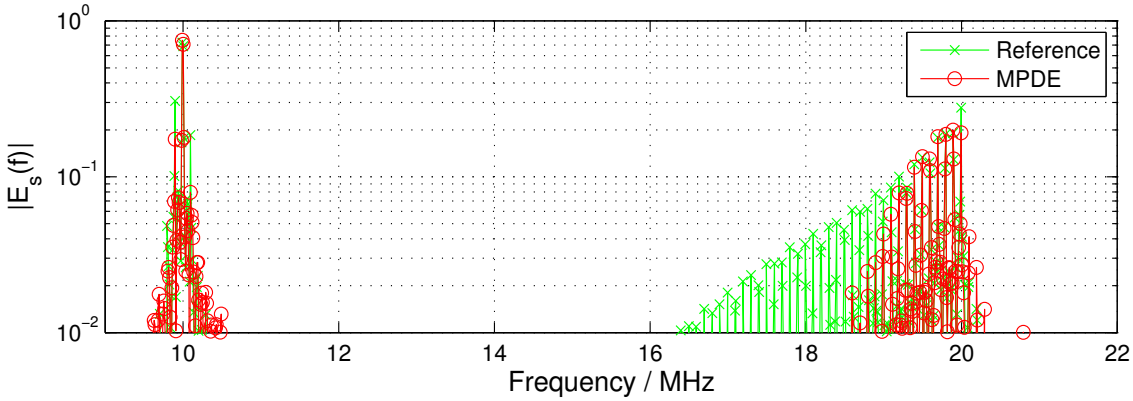

(c) $|E_s(f)|$ amplitude spectra

Figure 6.14: MPDE solution for Case (III) with $\Delta t_2 = 50\Delta t_1$, $M = 34$.

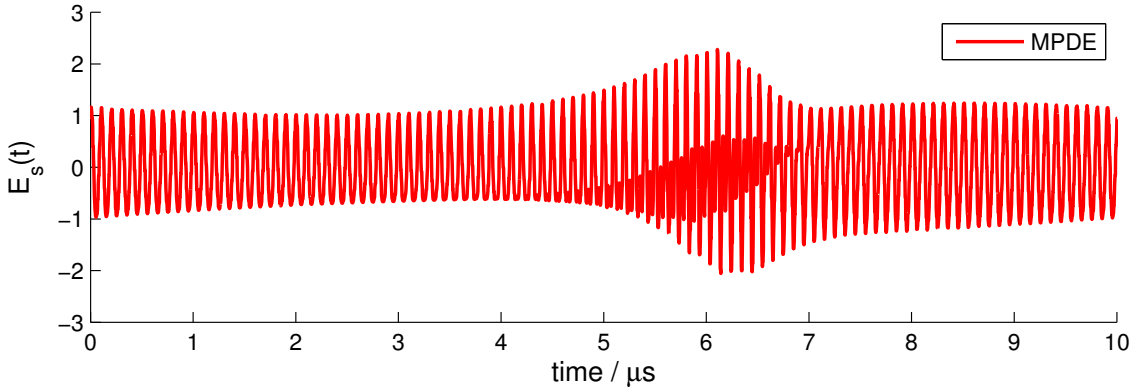

(a) $E_s(t)$ signal amplitude of MPDE solution

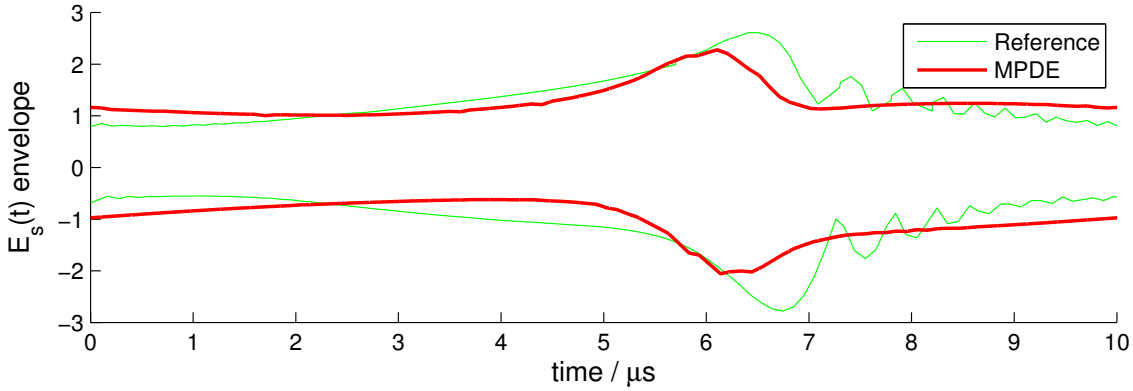

(b) $E_s(t)$ envelope for MPDE and reference FDTD solution

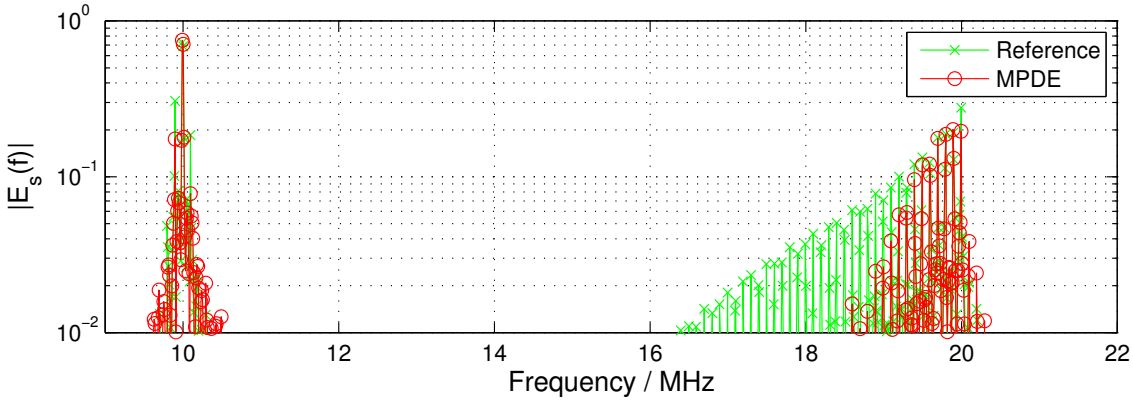

(c) $|E_s(f)|$ amplitude spectra

Figure 6.15: MPDE solution for Case (III) with $\Delta t_2 = 100\Delta t_1$, $M = 34$.

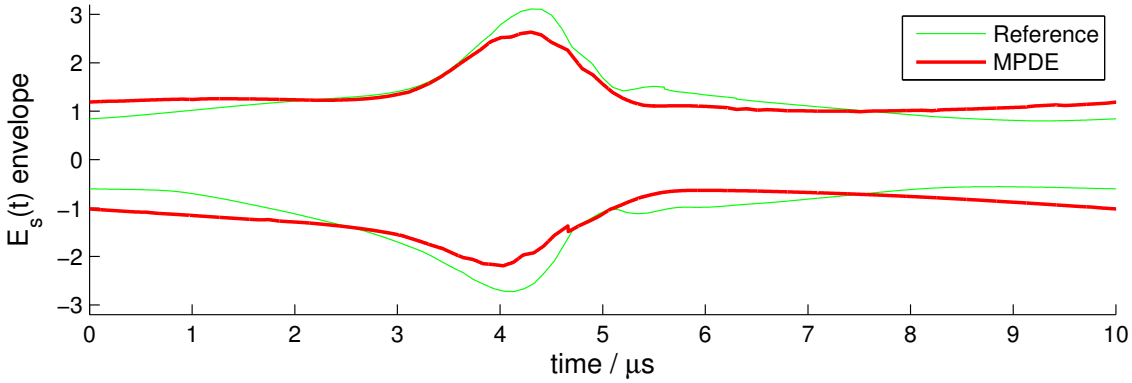

(a) $E_s(t)$ envelope for MPDE and reference FDTD solution

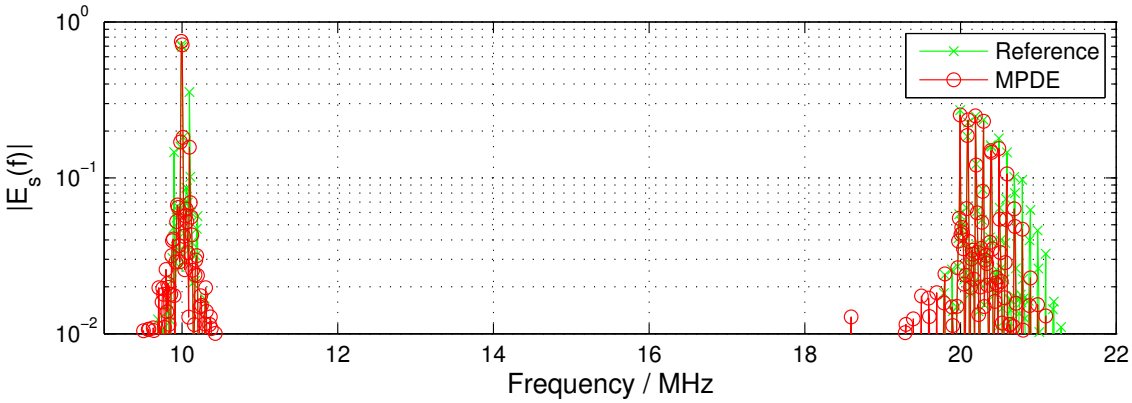

(b) $|E_s(f)|$ amplitude spectra

Figure 6.16: MPDE solution for Case (III) with $\Delta t_2 = 50\Delta t_1$, $M = 34$, and reversed propagation direction of the wave-like permittivity variation, according to (6.65).

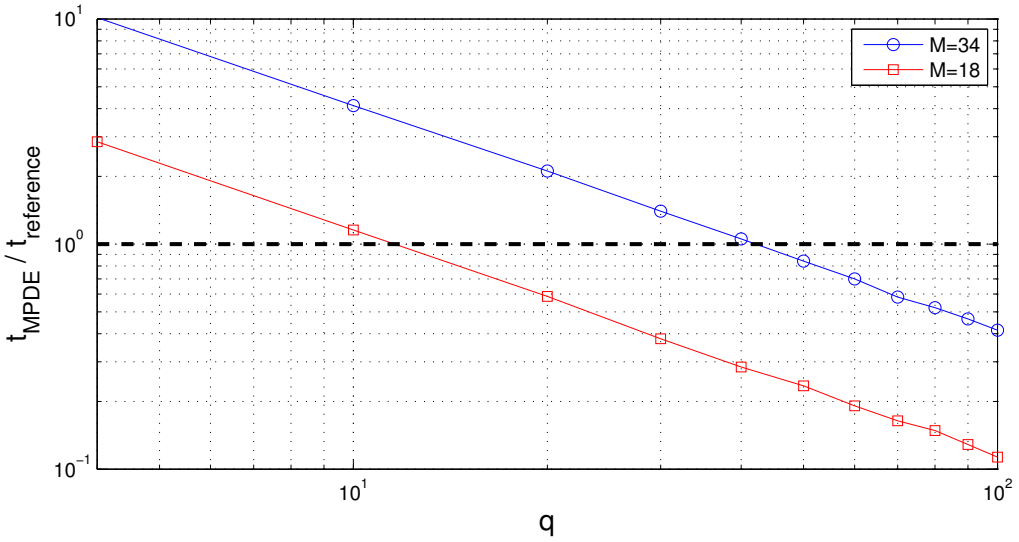

Figure 6.17: Ratio of the computation time for the MPDE scheme (t_{MPDE}) to that for the univariate PDE ($t_{\mathrm{reference}}$), with $q = \Delta t_2/\Delta t_1$ and $M = T_1/\Delta t_1$.

for the reference solution, an implicit scheme, we are not constrained by the CFL stability condition and hence may enlarge Δt_1. We have repeated the computation for $M = 18$. The computation time is reduced by a factor ~ 3.6 compared to the previously used $M = 34$. As a consequence the MPDE scheme performs faster than the reference solution for $q \geq 12$. The results for $M = 18$ and $q = 20$ are shown in Figure 6.18. These results are in good agreement with the reference solution and our simulation is completed in 59% of the time needed to compute the reference solution.

6.5.4 Case study (IV)

For our forth case study the following parameters have been changed from Case (III) to the values stated: $f_1 = 10$ MHz, $f_2 = 1$ kHz, $L_m = 10$ m, $L = 20$ m, and $M = 68$. For comparison to the other cases, these values are listed in Table 6.1 under Case (IV). The values for ϵ_m and ϵ_v remain unchanged. The time scales are separated by a factor 10^4. The phase velocity for the permittivity is $v_{ph} = 10^4$ ms^{-1}. Hence, the phase velocity is in the range of acoustic phase velocities achieved in SAW devices

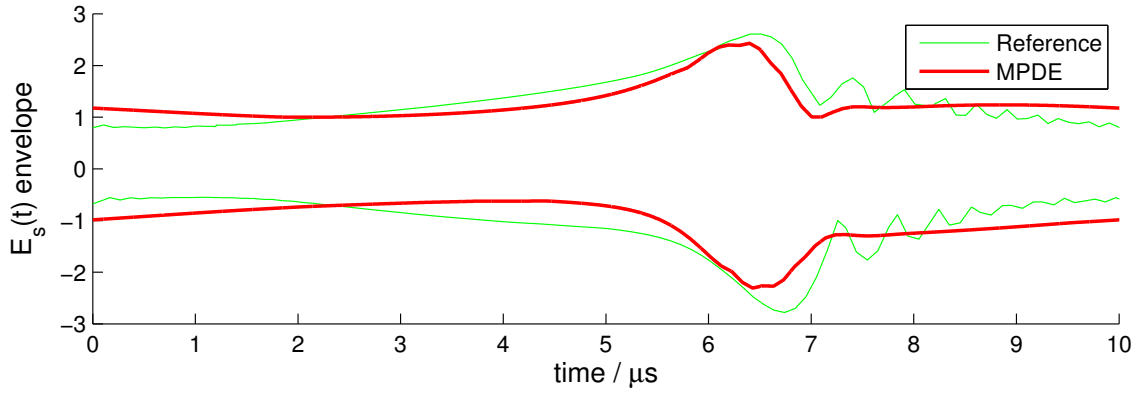

(a) $E_s(t)$ envelope for MPDE and reference FDTD solution

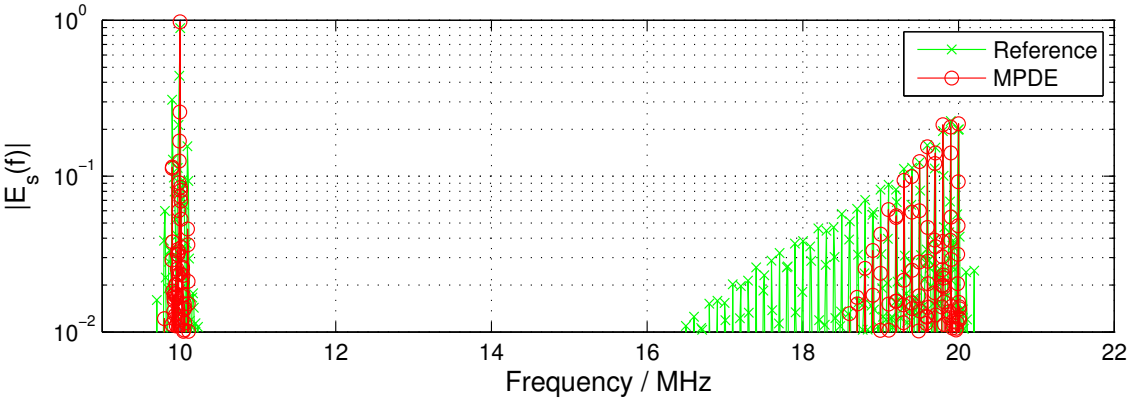

(b) $|E_s(f)|$ amplitude spectra

Figure 6.18: MPDE solution with $\Delta t_2 = 20\Delta t_1$, $M = 18$ for Case (III).

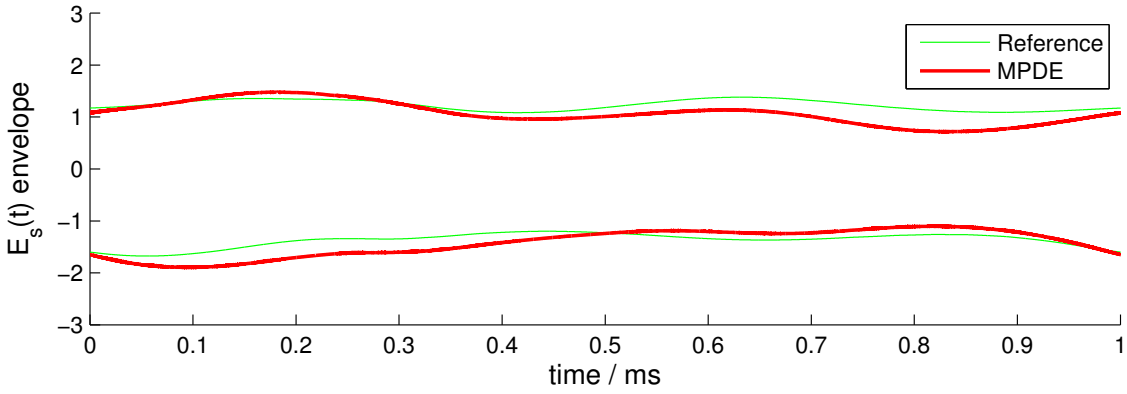

(a) $E_s(t)$ envelope for MPDE and reference FDTD solution

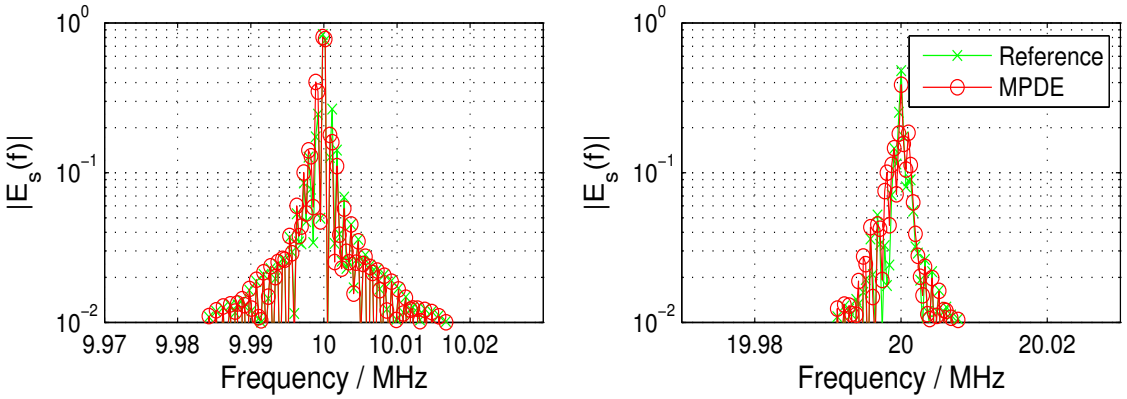

(b) $|E_s(f)|$ amplitude spectra

Figure 6.19: MPDE solution for case study (IV) with $\Delta t_2 = 1000\Delta t_1$.

[8]. This example explores the use of the MPDE method to an EM problem for which the interaction with the electromagnetic wave may stem from acoustic phenomena. The time resolution Δt_1 in the MPDE scheme is chosen to be the same as Δt for the univariate reference solution. The results for $\Delta t_2 = q\Delta t_1$, with $q = 10^3$ are plotted in Figure 6.19. The envelope of MPDE solution captures the envelope of the reference solution well. Intermodulation frequencies in the amplitude spectra are spaced at $\Delta f \approx 1$ kHz. The time to compute the MPDE solution amounts to 2% of the computation time of the reference solution for our MATLAB program.

6.6 Conclusion

In this chapter, we have developed an MPDE formulation to solve EM wave problems with widely separated time scales in one dimension. We have demonstrated the formulation for the case of a domain with space- and time-dependent permittivity. In this case the time variation of the permittivity is much slower in oscillation than the EM signal. We have considered this example for different choices in the permittivity properties. One of these choices is motivated by applications that involve acoustically induced time-varying material and/or domain properties. In a further example, the permittivity was neither space nor time dependent but rather had a time-dependent termination of the domain. The termination had a slow oscillatory impedance variation.

The computed results yield good agreement with the reference solutions obtained for the conventional univariate PDEs by applying the explicit Yee scheme. With proper parameter sets chosen for the MPDE scheme, the scheme may significantly reduce computation time while delivering solutions which have characterized our reference solutions very well. The reduction of the computation time can be influenced easily by changing the refinement of the numerical discretizations and the integration step size of the time envelope approach. While accurate solutions may be obtained faster than with a univariate approach, a degradation of the solution will eventually occur if the temporal resolution and integration time step become too coarse.

We give a complexity estimation for the number of operations to solve the PDE and the MPDE in Table 6.2. For the MPDE the estimation is done for a solution performing an LU factorization with and without taking advantage of the sparsity and bandedness of the matrix [152, 153]. The number of operations is estimated for a one-, two-, and three-dimensional problem, where $J = J_x J_y J_z$ is the total number of spatial sample points, and J_i, $i = \{x, y, z\}$, the number of sample points along each

Table 6.2: Estimation of the number of operations to solve the single and mutli-time PDE schemes for one-, two-, and three-dimensional problems. J is the number of spatial sample points, $M = T_1/\Delta t$, and $\hat{M} = T_1/\Delta t_1$. N_s and $\bar{N}_s$ are the numbers of slow periods in the univariate case and the multivariate case respectively. k is the matrix bandwidth.

	Explicit univariate PDE scheme	Implicit MPDE scheme with LU factorization	Implicit MPDE scheme with LU factorization for a sparse banded matrix
1D	$2JM\frac{T_2}{T_1}N_s$	$\frac{5}{3}(2J\hat{M})^3\frac{T_2}{T_1}\frac{\hat{M}\bar{N}_s}{q}$	$4k^2 2J\hat{M}\frac{T_2}{T_1}\frac{\hat{M}\bar{N}_s}{q}$
2D	$3JM\frac{T_2}{T_1}N_s$	$\frac{5}{3}(3J\hat{M})^3\frac{T_2}{T_1}\frac{\hat{M}\bar{N}_s}{q}$	$4k^2 3J\hat{M}\frac{T_2}{T_1}\frac{\hat{M}\bar{N}_s}{q}$
3D	$6JM\frac{T_2}{T_1}N_s$	$\frac{5}{3}(6J\hat{M})^3\frac{T_2}{T_1}\frac{\hat{M}\bar{N}_s}{q}$	$4k^2 6J\hat{M}\frac{T_2}{T_1}\frac{\hat{M}\bar{N}_s}{q}$

spatial dimension. In Table 6.2, we choose $M = T_1/\Delta t$ to represent the temporal resolution of the fast scale for the univariate case, and $\hat{M} = T_1/\Delta t_1$ for the multi-time case. N_s and $\bar{N}_s$ are the numbers of slow periods in the univariate case and the multivariate case respectively. The ratio of the complexity of the explicit FDTD to that of the MPDE scheme is found from Table 6.2 as

$$\frac{\text{complexity explicit FDTD}}{\text{complexity implict MPDE}} = \frac{N_s}{\bar{N}_s}\frac{qM}{(2k\hat{M})^2}\,, \tag{6.66}$$

where k is the matrix bandwidth. Geometries with very fine features that require fine grid size, and hence fine temporal sampling, will produce results with the MPDE in cases with $\hat{M} << M$. For one-dimensional problems the matrix bandwidth is small. Hence, we expect computational gains from the use of implicit MPDE for such problems. For three-dimensional problems the matrix bandwidth will be large in general. For this case iterative sparse solvers are needed to keep the complexity low [154].

Chapter 7

Discussion

7.1 Summary

This work has been concerned with challenges that arise in the numerical modeling of phenomena that involve coupling of electromagnetic field theory with other physical domains. The challenging issues for these problems of multi-domain physical interactions are to achieve high modeling accuracy and modeling efficiency despite highly disparate spatial and temporal scales.

The emphasis in this work is on three technically important cases of electromagnetic multiphysics phenomena. We investigated the electromagnetic wave propagation through the adjacent surfaces of a metallic contact. A methodology for the phenomenological modeling of PIM generation due to electron tunneling in metallic contacts, known as the *rusty bolt effect*, has been developed. This treatment yields a nonlinear telegrapher's equation with distributed nonlinear voltage controlled current sources. Surface roughness and skin effect are included in the derived model which is compatible with nonlinear network analysis tools like SPICE. The developed model is the first multi-scale model put forward which allows for the quantitative analysis of this problem and, hence, enables us to analyze the impact of various parameters of the structure on the PIM levels.

The second methodology developed is the Lagrangian mapping approach for the modeling of electromagnetic phenomena in domains with curved moving boundaries.

It is implemented in the FDTD method. By defining a mapping of a deformed (physical) domain onto a reference domain with Cartesian boundaries, the standard FDTD scheme on a rectangular grid can be utilized to model time-varying curved boundaries. The map of the Maxwell equation system yields a modified nabla operator for the LM method. Other methods, which use orthogonal grids for modeling curved boundaries, may require substantial spatial oversampling to achieve good accuracy. The LM method, however, significantly relaxes these spatial oversampling requirements. Furthermore, the complexity in the mesh generation is not increased for the LM method, and a complex development of the discrete forms of the curl operators is not necessary either. Hence, the Lagrangian mapping method provides high accuracy and improved modeling and computational efficiency.

The third development is a multi-time partial differential equation formulation for the modeling of one-dimensional EM wave phenomena. Large disparity between governing time scales leads to increased computational cost and hence to increased computation time and memory requirements for obtaining a response. The MPDE method introduces multiple time scales and, as a consequence, reduces the temporal oversampling requirements. In our studies we have shown that the MPDE formulation can achieve substantial reductions of the computation time for some problems with respect to the computation time required for the solution of the single time PDE. The MPDE method has not been applied to problems of distributed wave phenomena prior to this work. The MPDE method was able to provide solutions with very good accuracy with respect to the reference solutions and with (significantly) reduced processing time.

7.2 Future Work

Regarding the statistical method to model the problem of PIM in RF contacts, presented in Chapter 3, it would be of great interest to research this model in conjunction with empirical data. The prediction of PIM levels remains very difficult to this date. Performing a statistical analysis with empirical data may improve the understanding of the effects causing passive intermodulation. A derivation of macro-models for RF connectors based on prior statistical modeling may help in the design and analysis of RF systems.

The Lagrangian mapping method provides high accuracy while relaxing spatial oversampling requirements and hence the computational cost. The anisotropic FDTD implementation is known for issues regarding the long-term stability of the algorithm resulting from the fact that the different components of the electric and magnetic field are defined on spatially separated sampling points [110]. In particular the analysis of problems with widely separated time scales is hampered by these instability issues. Hence, it is of interest to improve the robustness of the algorithm, for example by an improved averaging scheme of the field components. The implementation of the LM method with other numerical techniques, such as the TLM method, is clearly of interest, too. In the TLM method field components are defined not on a staggered but on a common grid. This may help to reduce long-term instabilities. Though there is work on anisotropic schemes for the TLM method available [155, 156], further research will be necessary to implement a Lagrangian mapping scheme in the TLM method.

With respect to the MPDE method it will be of interest to extend the MPDE scheme for the electromagnetic wave equation to problems of two and three dimensions. The MPDE method reduces the number of integration steps required for a numerical solution of the problem. This can help to reduce the computational cost

of solving the univariate PDE problem depending on the scaling of the parameters involved. Due to the reduced number of integration steps, this will provide progress toward a method that avoids or delays the occurrence of long-term instabilities, as discussed with regard to the previous problem. If this proves successful, a combination of the MPDE and the LM methods will be a further goal of interest.

References

[1] A. A. Oliner, *Acoustic Surface Waves*. Berlin, Germany: Springer, 1978. [Online]. Available: http://dx.doi.org/10.1007/3-540-08575-0

[2] G. Karniadakis, A. Beskok, and N. R. Aluru, *Microflows and Nanoflows - Fundamentals and Simulation*, ser. Interdisciplinary applied mathematics. New York, NY: Springer, 2005. [Online]. Available: http://dx.doi.org/10.1007/0-387-28676-4

[3] M. Bown and C. Meinhart, "AC electroosmotic flow in a DNA concentrator," *Microfluidics and Nanofluidics*, vol. 2, no. 6, pp. 513–523, Nov. 2006. [Online]. Available: http://dx.doi.org/10.1007/s10404-006-0097-4

[4] T. Kohashi and H. Onishi, "Electro-osmotic printer," *Journal of the Society for Information Display*, vol. 5, no. 4, pp. 405–410, Dec. 1997. [Online]. Available: http://link.aip.org/link/?JSI/5/405/1

[5] G. M. Rebeiz, *RF MEMS - Theory, Design, and Technology*. Hoboken, NJ: Wiley, 2003.

[6] W. A. Goddard III, D. W. Brenner, S. E. Lyshevski, and G. J. Iafrate (Editors), *Handbook of Nanoscience, Engineering, and Technology*, 2nd ed. Boca Raton, FL: CRC Press, 2007.

[7] M. B. Steer, "Multi physics multi scale modeling of microwave circuits and systems hybridizing circuit, electromagnetic and thermal modeling," in *15th International Conference on Microwaves, Radar and Wireless Communications (MIKON)*, vol. 3, May 2004, pp. 1097–1105. [Online]. Available: http://dx.doi.org/10.1109/MIKON.2004.1358579

[8] R. Weigel, D. Morgan, J. Owens, A. Ballato, K. Lakin, K. Hashimoto, and C. Ruppel, "Microwave acoustic materials, devices, and applications," *IEEE Transactions on Microwave Theory and Techniques*, vol. 50, no. 3, pp. 738–749, Mar. 2002. [Online]. Available: http://dx.doi.org/10.1109/22.989958

[9] K. A. Ingebrigtsen, "Surface waves in piezoelectrics," *Journal of Applied Physics*, vol. 40, no. 7, pp. 2681–2686, June 1969. [Online]. Available: http://link.aip.org/link/?JAP/40/2681/1

[10] H. F. Tiersten, "Wave propagation in an infinite piezoelectric plate," *The Journal of the Acoustical Society of America*, vol. 35, no. 2, pp. 234–239, Feb. 1963. [Online]. Available: http://link.aip.org/link/?JAS/35/234/1

[11] J. J. Campbell and W. R. Jones, "A method for estimating optimal crystal cuts and propagation directions for excitation of piezoelectric surface waves," *IEEE Transactions on Sonics and Ultrasonics*, vol. 15, no. 4, pp. 209–217, Oct. 1968.

[12] H. Meier and P. Russer, "Analysis of leaky surface acoustic wave reflections," in *Proceedings of the IEEE, Ultrasonics Symposium*, vol. 1, 31 Oct.-3 Nov. 1993, pp. 201–204. [Online]. Available: http://dx.doi.org/10.1109/ULTSYM.1993.339678

[13] T. E. McKnight, C. T. Culbertson, S. C. Jacobson, and J. M. Ramsey, "Electroosmotically induced hydraulic pumping with integrated electrodes on microfluidic devices," *Analytical Chemistry*, vol. 73, no. 16, pp. 4045–4049, Aug. 2001. [Online]. Available: http://dx.doi.org/10.1021/ac010048a

[14] S. Chakraborty and D. Paul, "Microchannel flow control through a combined electromagnetohydrodynamic transport," *Journal of Physics D: Applied Physics*, vol. 39, no. 24, pp. 5364–5371, Dec. 2006. [Online]. Available: http://www.iop.org/EJ/abstract/0022-3727/39/24/038

[15] A. V. Oppenheim, A. S. Willsky, and S. H. Nawab, *Signals & Systems*, 2nd ed., ser. Prentice-Hall signal processing series. Upper Saddle River, NJ: Prentice Hall, 1997.

[16] K. S. Kundert, J. K. White, and A. L. Sangiovanni-Vincentelli, *Steady-State Methods for Simulating Analog and Microwave Circuits*, 1st ed. Boston, MA: Kluwer Academic Publishers, 1990.

[17] S. A. Maas, *Nonlinear Microwave and RF Circuits*, 2nd ed. Boston, MA: Artech House Publishers, 2003.

[18] R. F. Harrington, *Field Computation by Moment Methods*. New York, NY: Macmillan, 1968.

[19] J. Jin, *The Finite Element Method in Electromagnetics*, 2nd ed. New York, NY: Wiley, 2002.

[20] K. S. Yee, "Numerical solution of initial boundary value problems involving Maxwell's equations in isotropic media," *IEEE Transactions on Antennas and Propagation*, vol. 14, pp. 302–307, May 1966. [Online]. Available: http://dx.doi.org/10.1109/TAP.1966.1138693

[21] A. Taflove and S. Hagness, *Computational Electrodynamics: The Finite-Difference Time-Domain Method*. Boston, MA: Artech House, 2005.

[22] W. J. R. Hoefer, "The transmission-line matrix method – Theory and applications," *IEEE Transactions on Microwave Theory and Technique*, vol. 33, pp. 882–893, Oct. 1985. [Online]. Available: http://dx.doi.org/10.1109/TMTT.1985.1133146

[23] T. Itoh, *Numerical Techniques for Microwave and Millimeter-Wave Passive Structures*. New York, NY: Wiley-Interscience, Apr. 1989.

[24] L. W. NAGEL, "SPICE2: A computer program to simulate semi-conductor circuits," Ph.D. dissertation, University of California, Berkeley, 1975.

[25] A. Vladimirescu, *The SPICE Book*. New York, NY: Wiley, 1994.

[26] J. Chen, S. Kang, J. Zou, C. Liu, and J. Schutt-Ainé, "Reduced-order modeling of weakly nonlinear MEMS devices with Taylor-series expansion and Arnoldi approach," *Journal of Microelectromechanical Systems*, vol. 13, no. 3, pp. 441–451, June 2004. [Online]. Available: http://dx.doi.org/10.1109/JMEMS.2004.828704

[27] A. E. Ruehli and A. C. Cangellaris, "Progress in the methodologies for the electrical modeling of interconnects and electronic packages," *Proceedings of the IEEE*, vol. 89, no. 5, pp. 740–771, May 2001. [Online]. Available: http://dx.doi.org/10.1109/5.929652

[28] K. Hess, *Monte Carlo Device Simulation: Full Band and Beyond*, 1st ed. Boston, MA: Kluwer Academic Publishers, Aug. 1991.

[29] H. Tsuchiya and U. Ravaioli, "Particle Monte Carlo simulation of quantum phenomena in semiconductor nanostructures," *Journal of Applied Physics*, vol. 89, no. 7, pp. 4023–4029, Apr. 2001. [Online]. Available: http://link.aip.org/link/?JAP/89/4023/1

[30] G. R. Liu, *Mesh Free Methods: Moving Beyond the Finite Element Method*, 1st ed. Boca Raton, FL: CRC Press, July 2003.

[31] D. Peyrou, P. Pons, H. Granier, D. Leray, A. Ferrand, K. Yacine, M. Saadaoui, A. Nicolas, J. Tao, and R. Plana, "Multiphysics softwares benchmark on Ansys / Comsol applied for RF MEMS switches packaging simulations," in *7th International Conference on Thermal, Mechanical and Multiphysics Simulation and Experiments in Micro-Electronics and Micro-Systems (EuroSime)*, Apr. 2006, pp. 1–8. [Online]. Available: http://dx.doi.org/10.1109/ESIME.2006.1644011

[32] W. B. J. Zimmerman, *Multiphysics Modelling with Finite Element Methods*. Hackensack, NJ: World Scientific, 2006.

[33] C. A. Balanis, *Advanced Engineering Electromagnetics*. New York, NY: Wiley, 1989.

[34] W. S. Weiglhofer and A. Lakhtakia, *Introduction to Complex Mediums for Optics and Electromagnetics*. Bellingham, WA: SPIE Publications, 2003.

[35] G. D. Smith, *Numerical Solution of Partial Differential Equations - Finite Difference Methods*, 3rd ed. Oxford, United Kingdom: Oxford University Press, 1999.

[36] L. Lapidus and G. F. Pinder, *Numerical Solution of Partial Differential Equations in Science and Engineering*, 1st ed. New York, NY: Wiley, 1982.

[37] M. N. O. Sadiku, *Numerical Techniques in Electromagnetics*, 2nd ed. Boca Raton, FL: CRC Press, 2000.

[38] J. Crank and P. Nicolson, "A practical method for numerical evaluation of solutions of partial differential equations of the heat-conduction type," *Advances in Computational Mathematics*, vol. 6, no. 1, pp. 207–226, Dec. 1996. [Online]. Available: http://dx.doi.org/10.1007/BF02127704

[39] P. D. Lax and R. D. Richtmyer, "Survey of the stability of linear finite difference equations," *Communications on Pure and Applied Mathematics*, vol. 9, no. 2, pp. 267–293, May 1956. [Online]. Available: http://dx.doi.org/10.1002/cpa.3160090206

[40] R. D. Richtmyer and K. W. Morton, *Difference Methods for Initial-Value Problems*, 2nd ed. Malabar, FL: Krieger, 1994.

[41] V. G. Ganzha and E. V. Vorozhtsov, *Computer-Aided Analysis of Difference Schemes for Partial Differential Equations*. New York, NY: Wiley, 1996.

[42] R. Courant, K. Friedrichs, and H. Lewy, "Über die partiellen Differenzengleichungen der mathematischen Physik," *Mathematische Annalen*, vol. 100, no. 1, pp. 32–74, Dec. 1928. [Online]. Available: http://dx.doi.org/10.1007/BF01448839

[43] A. Sommerfeld, "Die Greensche Funktion der Schwingungsgleichung." *Jahresbericht der Deutschen Mathematiker-Vereinigung*, vol. 21, pp. 309–353, 1912. [Online]. Available: http://resolver.sub.uni-goettingen.de/purl?GDZPPN002123851

[44] A. Sommerfeld, *Partial Differential Equations in Physics*. New York, NY: Academic Press, 1949.

[45] A. Bayliss and E. Turkel, "Radiation boundary conditions for wave-like equations," *Communications on Pure and Applied Mathematics*, vol. 33, no. 6, pp. 707–725, Nov. 1980. [Online]. Available: http://dx.doi.org/10.1002/cpa.3160330603

[46] B. Engquist and A. Majda, "Absorbing boundary conditions for the numerical simulation of waves," *Mathematics of Computation*, vol. 31, no. 139, pp. 629–651, July 1977. [Online]. Available: http://www.jstor.org/stable/2005997

[47] G. Mur, "Absorbing boundary conditions for the finite-difference approximation of the time-domain electromagnetic-field equations," *IEEE Transactions on Electromagnetic Compatibility*, vol. EMC-23, no. 4, pp. 377–382, Nov. 1981. [Online]. Available: http://dx.doi.org/10.1109/TEMC.1981.303970

[48] J.-P. Bérenger, "A perfectly matched layer for the absorption of electromagnetic waves," *Journal of Computational Physics*, vol. 114, no. 2, pp. 185–200, Oct. 1994. [Online]. Available: http://dx.doi.org/10.1006/jcph.1994.1159

[49] J.-P. Bérenger, *Perfectly Matched Layer (PML) for Computational Electromagnetics*. San Rafael, CA: Morgan & Claypool, Feb. 2007. [Online]. Available: http://www.morganclaypool.com/doi/abs/10.2200/S00030ED1V01Y200605CEM008

[50] S. Hienonen, "Studies on microwave antennas: Passive intermodulation distortion in antenna structures and design of microstrip antenna elements," Ph.D. dissertation, Helsinki University of Technology Radio Laboratory Publications, Espoo, Finland, 2005.

[51] C. P. Vicente Quiles, "Passive intermodulation and corona discharge for microwave structures in communications satellites," Ph.D. dissertation, Technischen Universität Darmstadt, Germany, 2005. [Online]. Available: http://d-nb.info/976147394

[52] J. S. Petit and A. D. Rawlins, "The impact of passive intermodulation on specifying and characterising components," in *Electronic Component Conference - EECC'97*, ser. ESA Special Publication, B. Kaldeich-Schürmann, Ed., vol. 395, July 1997, pp. 45–49.

[53] R. Holm, *Electric Contacts: Theory and Application*, 4th ed. Berlin, Germany: Springer, 1999.

[54] C. Vicente and H. Hartnagel, "Passive-intermodulation analysis between rough rectangular waveguide flanges," *IEEE Transactions on Microwave Theory and Techniques*, vol. 53, no. 8, pp. 2515–2525, Aug. 2005. [Online]. Available: http://dx.doi.org/10.1109/TMTT.2005.852771

[55] C. Vicente, D. Wolk, H. L. Hartnagel, B. Gimeno, V. E. Boria, and D. Raboso, "Experimental analysis of passive intermodulation at waveguide flange bolted connections," *IEEE Transactions on Microwave Theory and Techniques*, vol. 55, no. 5, pp. 1018–1028, May 2007. [Online]. Available: http://dx.doi.org/10.1109/TMTT.2007.895400

[56] S. M. Sze and K. K. Ng, *Physics of Semiconductor Devices*, 3rd ed. New York, NY: Wiley-Interscience, Oct. 2006.

[57] R. Sorrentino and P. Mezzanotte, "Electromagnetic modelling of RF MEMS structures," in *XXVIIth General Assembly of the U.R.S.I.*, Maastricht, Netherlands, 17-24 Aug. 2002, pp. 1364–1367.

[58] N. Bushyager, B. McGarvey, and M. M. Tentzeris, "Adaptive numerical modeling of RF structures requiring the coupling of Maxwell's, mechanical and solid-state equations," in *17th Annual Review of Progress in Applied Computational Electromagnetics*, Monterey, CA, Mar. 2001, pp. 1–8.

[59] L. Vietzorreck, "EM modeling of RF MEMS," in *7th International Conference on Thermal, Mechanical and Multiphysics Simulation and Experiments in Micro-Electronics and Micro-Systems (EuroSime)*, Como, Italy, 24-26 Apr. 2006, pp. 1–4. [Online]. Available: http://dx.doi.org/10.1109/ESIME.2006.1644057

[60] A. Dec and K. Suyama, "Micromachined electro-mechanically tunable capacitors and their applications to RF IC's," *IEEE Transactions on Microwave Theory and Techniques*, vol. 46, no. 12, pp. 2587–2596, Dec. 1998. [Online]. Available: http://dx.doi.org/10.1109/22.739251

[61] M. Shavezipur, A. Khajepour, and S. M. Hashemi, "Development of novel segmented-plate linearly tunable MEMS capacitors," *Journal Micromechanics and Microengineering*, vol. 18, no. 3, pp. 035 035–1–8, Mar. 2008. [Online]. Available: http://dx.doi.org/10.1088/0960-1317/18/3/035035

[62] D. Peroulis, S. Pacheco, K. Sarabandi, and L. P. Katehi, "MEMS devices for high isolation switching and tunable filtering," in *IEEE MTT-S International Microwave Symposium Digest*, vol. 2, 11-16 June 2000, pp. 1217–1220. [Online]. Available: http://dx.doi.org/10.1109/MWSYM.2000.863578

[63] I. S. Kim and W. J. R. Hoefer, "A local mesh refinement algorithm for the time domain-finite difference method using Maxwell's curl equations," *IEEE Transactions on Microwave Theory and Techniques*, vol. 38, no. 6, pp. 812–815, June 1990. [Online]. Available: http://dx.doi.org/10.1109/22.130985

[64] M. Krumpholz and L. P. B. Katehi, "MRTD: New time-domain schemes based on multiresolution analysis," *IEEE Transactions on Microwave Theory and Techniques*, vol. 44, no. 4, pp. 555–571, Apr. 1996. [Online]. Available: http://dx.doi.org/10.1109/22.491023

[65] N. Bushyager and M. M. Tentzeris, *MRTD (Multi Resolution Time Domain) Method in Electromagnetics*. San Rafael, CA: Morgan & Claypool, 2006. [Online]. Available: http://dx.doi.org/10.2200/S00009ED1V01Y200508CEM002

[66] C. D. Sarris, *Adaptive Mesh Refinement for Time-Domain Numerical Electromagnetics*. San Rafael, CA: Morgan & Claypool, Dec. 2006. [Online]. Available: http://dx.doi.org/10.2200/S00052ED1V01Y200609CEM011

[67] C. Christopoulos, *The Transmission Line Matrix Method TLM*. New York, NY: IEEE Press, 1995.

[68] U. Mueller, A. Beyer, and W. Hoefer, "Moving boundaries in 2-D and 3-D TLM simulations realized by recursive formulas," *IEEE Transactions on Microwave Theory and Techniques*, vol. 40, no. 12, pp. 2267–2271, Dec. 1992. [Online]. Available: http://dx.doi.org/10.1109/22.179889

[69] P. L. Lui, "A study of intermodulation interference due to non-linearities in metallic structures," Ph.D. dissertation, University of Kent, Canterbury, United Kingdom, 1990.

[70] V. Golikov, S. Hienonen, and P. Vainikainen, "Passive intermodulation distortion measurements in mobile communication antennas," in *Proceedings of the IEEE VTS Vehicular Technology Conference, VTC2001-Fall*, vol. 4, Atlantic City, NJ, 7-11 Oct. 2001, pp. 2623–2625. [Online]. Available: http://dx.doi.org/10.1109/VTC.2001.957226

[71] J. A. Jargon, "Measurement comparison of a low-intermodulation termination for the U.S. wireless industry," NIST, Technical Note 1521, July 2001.

[72] V. Golikov, S. Hienonen, and P. Vainikainen, "Effect of impedance loading at higher harmonics on passive intermodulation in antennas," in *Proceedings of the IEEE Antennas Propagation Society International Symposium*, vol. 4, Columbus, OH, 22-27 June 2003, pp. 378–381. [Online]. Available: http://dx.doi.org/10.1109/APS.2003.1220200

[73] P. L. Lui, A. D. Rawlins, and D. W. Watts, "Measurement of intermodulation products generated by structural components," *Electronics Letters*, vol. 24, pp. 1005–1007, Aug. 1988. [Online]. Available: http://dx.doi.org/10.1049/el:19880684

[74] P. L. Lui, "Passive intermodulation interference in communication systems," *Electronics and Communication Engineering Journal*, vol. 2, pp. 109–118, June 1990. [Online]. Available: http://dx.doi.org/10.1049/ecej:19900029

[75] J. D. Lavers and R. S. Timsit, "Constriction resistance at high signal frequencies," *IEEE Transactions on Components and Packaging Technologies*, vol. 25, pp. 446–452, Sept. 2002. [Online]. Available: http://dx.doi.org/10.1109/TCAPT.2002.804610

[76] G. Macchiarella, G. B. Stracca, and L. Miglioli, "Experimental study of passive intermodulation in coaxial cavities for cellular base stations duplexers," in

Proceedings of the 34th European Microwave Conference (EuMC 2004), Amsterdam, Netherlands, 12-14 Oct. 2004, pp. 981–984.

[77] M. Runde, "Mass transport in stationary contact points," *IEEE Transactions on Components, Hybrids and Manufacturing Technology*, vol. 10, pp. 89–99, Mar. 1987. [Online]. Available: http://dx.doi.org/10.1109/TCHMT.1987.1134705

[78] J. G. Simmons, "Generalized formula for the electric tunnel effect between similar electrodes separated by a thin insulating film," *Journal of Applied Physics*, vol. 34, pp. 1793–1803, June 1963. [Online]. Available: http://link.aip.org/link/?JAPIAU/34/1793/1

[79] F. Forlani and N. Minnaja, "Rectification by means of metal-dielectric-metal sandwiches," *Nuovo Cimento*, vol. 31, pp. 1246–1257, Mar. 1964. [Online]. Available: http://dx.doi.org/10.1007/BF02733594

[80] W. H. Higa, "Spurious signals generated by electron tunneling on large reflector antennas," *Proceedings of the IEEE*, vol. 63, pp. 306–313, Feb. 1975. [Online]. Available: http://dx.doi.org/10.1109/PROC.1975.9736

[81] C. D. Bond, C. S. Guenzer, and C. A. Carosella, "Intermodulation generation by electron tunneling through aluminum-oxide films," *Proceedings of the IEEE*, vol. 67, pp. 1643–1652, Dec. 1979.

[82] J. Russer, A. Ramachandran, A. Cangellaris, and P. Russer, "Phenomenological modeling of passive intermodulation (PIM) due to electron tunneling at metallic contacts," in *IEEE MTT-S International Microwave Symposium Digest*, 11-16 June 2006, pp. 1129–1132. [Online]. Available: http://dx.doi.org/10.1109/MWSYM.2006.249389

[83] K. T. Hecht, *Quantum Mechanics*. New York, NY: Springer, 2000.

[84] P. M. Morse and H. Feshbach, *Methods of Theoretical Physics - Part 2*. New York, NY: McGraw-Hill, 1953.

[85] K. M. Coperich, J. M. V. I. Okhmatovski, A. C. Cangellaris, and A. E. Ruehli, "Systematic development of transmission-line models for interconnects with frequency-dependent losses," *IEEE Transactions on Microwave Theory and Technique*, vol. 49, pp. 1677–1685, Oct. 2001. [Online]. Available: http://dx.doi.org/10.1109/22.954771

[86] B. Gustavsen and A. Semlyen, "Rational approximation of frequency domain responses by vector fitting," *IEEE Transactions on Power Delivery*, vol. 14, pp. 1052–1061, July 1999. [Online]. Available: http://dx.doi.org/10.1109/61.772353

[87] G. V. Samsonov, *The Oxide Handbook*. New York, NY: IFI/Plenum, 1973.

[88] W. Feller, *An Introduction to Probability Theory and Its Applications*. New York, NY: Wiley, 1950.

[89] A. Papoulis, *Probability, Random Variables, and Stochastic Processes*. New York, NY: McGraw-Hill, 1965.

[90] R. Holland, "Finite-difference solutions of Maxwell's equations in generalized nonorthogonal coordinates," *IEEE Transactions on Nuclear Science*, vol. 30, pp. 4589–4591, Dec. 1983. [Online]. Available: http://dx.doi.org/10.1109/TNS.1983.4333176

[91] K. K. Mei, A. Cangellaris, and D. J. Angelakos, "Conformal time domain finite difference method," *Radio Science*, vol. 19, pp. 1145–1147, Sept.-Oct. 1984. [Online]. Available: http://dx.doi.org/10.1029/RS019i005p01145

[92] A. C. Cangellaris, C.-C. Lin, and K. K. Mei, "Point-matched time domain finite element methods for electromagnetic radiation and scattering," *IEEE Transactions on Antennas and Propagation*, vol. 35, pp. 1160–1173, Oct. 1987. [Online]. Available: http://dx.doi.org/10.1109/TAP.1987.1143981

[93] R. M. Mäkinen, H. De Gersem, T. Weiland, and M. A. Kivikoski, "Modeling of lossy curved surfaces in 3-D FIT/FDTD techniques," *IEEE Transactions on Antennas and Propagation*, vol. 54, pp. 3490–3498, Nov. 2006. [Online]. Available: http://dx.doi.org/10.1109/TAP.2006.884212

[94] W. Yu, Y. Liu, T. Su, N.-T. Huang, and R. Mittra, "A robust parallel conformal finite-difference time-domain processing package using the MPI library," *IEEE Antennas and Propagation Magazine*, vol. 47, pp. 39–59, June 2005. [Online]. Available: http://dx.doi.org/10.1109/MAP.2005.1532540

[95] C. Fumeaux, D. Baumann, and R. Vahldieck, "Finite-volume time-domain analysis of a cavity-backed Archimedean spiral antenna," *IEEE Transactions on Antennas and Propagation*, vol. 54, pp. 844–851, Mar. 2006. [Online]. Available: http://dx.doi.org/10.1109/TAP.2006.869935

[96] A. C. Cangellaris and D. B. Wright, "Analysis of the numerical error caused by the stair-stepped approximation of a conducting boundary in FDTD simulations of electromagnetic phenomena," *IEEE Transactions on Antennas and Propagation*, vol. 39, pp. 1518–1525, Oct. 1991. [Online]. Available: http://dx.doi.org/10.1109/8.97384

[97] H. Minkowski, "Die Grundgleichungen für die elektromagnetischen Vorgänge in bewegten Körpern," *Nachrichten von der Gesellschaft der Wissenschaften zu Göttingen*, pp. 53–111, 1908. [Online]. Available: http://resolver.sub.uni-goettingen.de/purl?GDZPPN00250152X

[98] J. G. Van Bladel, *Electromagnetic Fields*, 2nd ed. New York, NY: John Wiley, 2007. [Online]. Available: http://dx.doi.org/10.1002/047012458X

[99] R. C. Costen and D. Adamson, "Three dimensional derivation of the electromagnetic jump condition and momentum–energy laws at a moving boundary," *Proceedings of the IEEE*, vol. 53, pp. 1181–1196, Sept. 1965. [Online]. Available: http://dx.doi.org/10.1109/PROC.1965.4162

[100] B. L. Michielsen, G. C. Herman, A. T. de Hoop, and D. de Zutter, "Three-dimensional relativistic scattering of electromagnetic waves by an object in uniform translational motion," *Journal of Mathematical Physics*, vol. 22, no. 11, pp. 2716–2722, Nov. 1981. [Online]. Available: http://link.aip.org/link/?JMP/22/2716/1

[101] F. Harfoush, A. Taflove, and G. A. Kriegsmann, "A numerical technique for analyzing electromagnetic wave scattering from moving surfaces in one and two dimensions," *IEEE Transactions on Antennas and Propagation*, vol. 37, pp. 55–63, Jan. 1989. [Online]. Available: http://dx.doi.org/10.1109/8.192164

[102] D. S. Chandrasekharaiah and L. Debnath, *Continuum Mechanics*. San Diego, CA: Academic Press, 1994.

[103] G. Li and N. R. Aluru, "A Lagrangian approach for electrostatic analysis of deformable conductors," *Journal Microelectromechanical Systems*, vol. 11, pp. 245–254, June 2002. [Online]. Available: http://dx.doi.org/10.1109/JMEMS.2002.1007403

[104] J. A. Russer, P. S. Sumant, and A. C. Cangellaris, "A Lagrangian approach for the handling of curved boundaries in the finite-difference time-domain method," in *IEEE MTT-S International Microwave Symposium*, Honolulu, HI, 3-8 June 2007, pp. 717–720. [Online]. Available: http://dx.doi.org/10.1109/MWSYM.2007.380021

[105] J. A. Russer, P. S. Sumant, and A. C. Cangellaris, "Modeling of curved boundaries in the finite-difference time-domain method using a Lagrangian approach," *Springer Proceedings in Physics*, vol. 121, pp. 55–68, 2008. [Online]. Available: http://dx.doi.org/10.1007/978-3-540-68768-9_5

[106] J. A. Russer and A. C. Cangellaris, "An efficient methodology for the modeling of electromagnetic wave phenomena in domains with moving boundaries," in *IEEE MTT-S International Microwave Symposium*, Atlanta, GA, 15-20 June 2008, pp. 157–160. [Online]. Available: http://dx.doi.org/10.1109/MWSYM.2008.4633127

[107] A. J. Ward and J. B. Pendry, "Refraction and geometry in Maxwell's equations," *Journal of Modern Optics*, vol. 43, no. 4, pp. 773–793, Apr. 1996. [Online]. Available: http://www.informaworld.com/10.1080/09500349608232782

[108] A. Sommerfeld, *Mechanics of Deformable Bodies (Lectures on Theoretical Physics, Vol. 2)*. New York, NY: Academic Press, 1950.

[109] R. D. Cook, D. S. Malkus, M. E. Plesha, and R. J. Witt, *Concepts and Applications of Finite Element Analysis*. New York, NY: John Wiley, 2001.

[110] G. R. Werner and J. R. Cary, "A stable FDTD algorithm for non-diagonal, anisotropic dielectrics," *Journal of Computational Physics*, vol. 226, no. 1, pp. 1085–1101, Sept. 2007. [Online]. Available: http://www.sciencedirect.com/science/article/B6WHY-4NSMMXV-3/2/76a39541944c77b6c01c0bc77ab557ab

[111] S. Zhong, Z. Lai, S. Liu, and S. Liu, "The numerical dispersion relation and stability analysis of PLCDRC-FDTD method for anisotropic magnetized plasma," in *International Conference on Microwave and Millimeter Wave Technology (ICMMT)*, vol. 2, 21-24 Apr. 2008, pp. 666–669. [Online]. Available: http://dx.doi.org/10.1109/ICMMT.2008.4540483

[112] T. Kashiwa, H. Kudo, Y. Sendo, T. Ohtani, and Y. Kanai, "The phase velocity error and stability condition of the three-dimensional nonstandard FDTD method," *IEEE Transactions on Magnetics*, vol. 38, no. 2, pp. 661–664, Mar. 2002. [Online]. Available: http://dx.doi.org/10.1109/20.996172

[113] W. Beck and M. Mirotznik, "Generalized analysis of stability and numerical dispersion in the discrete-convolution FDTD method," *IEEE Transactions on Antennas and Propagation*, vol. 48, no. 6, pp. 887–894, June 2000. [Online]. Available: http://dx.doi.org/10.1109/8.865220

[114] R. F. Harrington, *Time Harmonic Electromagnetic Fields*. New York, NY: John Wiley, 2001.

[115] L. Brillouin, *Wave Propagation in Periodic Structures*. New York, NY: Dover, 1953.

[116] J. C. Slater, "Interaction of waves in crystals," *Reviews of Modern Physics*, vol. 30, no. 1, pp. 197–222, Jan. 1958. [Online]. Available: http://link.aps.org/doi/10.1103/RevModPhys.30.197

[117] A. Oliner and A. Hessel, "Guided waves on sinusoidally-modulated reactance surfaces," *IRE Transactions on Antennas and Propagation*, vol. 7, no. 5, pp. 201–208, Dec. 1959. [Online]. Available: http://dx.doi.org/10.1109/TAP.1959.1144771

[118] J.-C. Simon, "Action of a progressive disturbance on a guided electromagnetic wave," *IRE Transactions on Microwave Theory and Techniques*, vol. 8, no. 1, pp. 18–29, Jan. 1960. [Online]. Available: http://dx.doi.org/10.1109/TMTT.1960.1124657

[119] A. Hessel and A. Oliner, "Wave propagation in a medium with a progressive sinusoidal disturbance," *IRE Transactions on Microwave Theory*

and Techniques, vol. 9, no. 4, pp. 337–343, July 1961. [Online]. Available: http://dx.doi.org/10.1109/TMTT.1961.1125340

[120] E. Cassedy and A. Oliner, "Dispersion relations in time-space periodic media: Part I – Stable interactions," *Proceedings of the IEEE*, vol. 51, no. 10, pp. 1342–1359, Oct. 1963. [Online]. Available: http://dx.doi.org/10.1109/PROC.1963.2566

[121] T. Tamir, H. Wang, and A. Oliner, "Wave propagation in sinusoidally stratified dielectric media," *IEEE Transactions on Microwave Theory and Techniques*, vol. 12, no. 3, pp. 323–335, May 1964. [Online]. Available: http://dx.doi.org/10.1109/TMTT.1964.1125815

[122] C. Yeh, K. Casey, and Z. Kaprielian, "Transverse magnetic wave propagation in sinusoidally stratified dielectric media," *IEEE Transactions on Microwave Theory and Techniques*, vol. 13, no. 3, pp. 297–302, May 1965. [Online]. Available: http://dx.doi.org/10.1109/TMTT.1965.1125993

[123] L. Matekovits, G. Colome, and M. Orefice, "Propagation of electromagnetic waves in a sinusoidally modulated dielectric substrate," *IEEE Antennas and Wireless Propagation Letters*, vol. 6, pp. 207–210, 2007. [Online]. Available: http://dx.doi.org/10.1109/LAWP.2007.893098

[124] P. Russer, *Electromagnetics, Microwave Circuit and Antenna Design for Communications Engineering*, 2nd ed. Boston, MA: Artech House, 2006.

[125] C. Elachi, "Waves in active and passive periodic structures: A review," *Proceedings of the IEEE*, vol. 64, no. 12, pp. 1666–1698, Dec. 1976. [Online]. Available: http://dx.doi.org/10.1109/PROC.1976.10409

[126] R. E. Collin, *Foundations for Microwave Engineering.* New York, NY: McGraw-Hill, 1966.

[127] É. Mathieu, "Mémoire sur le mouvement vibratoire d'une membrane de forme elliptique," *Journal des Mathématiques Pures et Appliquées*, vol. 13, pp. 137–203, 1868.

[128] N. W. McLachlan, *Theory and Application of Mathieu Functions.* Oxford, United Kingdom: Clarendon, 1951.

[129] P. M. Morse and H. Feshbach, *Methods of Theoretical Physics - Part 1.* New York, NY: McGraw-Hill, 1953.

[130] G. Floquet, "Sur les équations différentielles linéaires à coefficients périodiques," *Annales Scientifiques de L'É.N.S.*, vol. 2, no. 12, pp. 47–88, 1883. [Online]. Available: http://www.numdam.org/item?id=ASENS_1883_2_12__47_0

[131] R. E. Collin, *Field Theory of Guided Waves.* New York, NY: IEEE Press, 1991.

[132] J. Manley and H. Rowe, "Some general properties of nonlinear elements - Part I. General energy relations," *Proceedings of the IRE*, vol. 44, no. 7, pp. 904–913, July 1956. [Online]. Available: http://dx.doi.org/10.1109/JRPROC.1956.275145

[133] G. N. Burlak, N. Y. Kotsarenko, and S. V. Koshevaya, "Interaction of electromagnetic and acoustic waves in solids," *Russian Physics Journal*, vol. 24, no. 8, pp. 732–742, Aug. 1981. [Online]. Available: http://dx.doi.org/10.1007/BF00941343

[134] C. T. Kelley, *Solving Nonlinear Equations with Newton's Method*. Philadelphia, PA: SIAM (Society for Industrial and Applied Mathematics), 2003.

[135] M. Born and E. Wolf, *Principles of Optics*, 7th ed. Cambridge, United Kingdom: Cambridge University Press, 2002.

[136] K. S. Kundert, "Introduction to RF simulation and its application," *IEEE Journal of Solid-State Circuits*, vol. 34, no. 9, pp. 1298–1319, Sept. 1999. [Online]. Available: http://dx.doi.org/10.1109/4.782091

[137] T. Namiki, "A new FDTD algorithm based on alternating-direction implicit method," *IEEE Transactions on Microwave Theory and Techniques*, vol. 47, no. 10, pp. 2003–2007, Oct. 1999. [Online]. Available: http://dx.doi.org/10.1109/22.795075

[138] S. Ju, K.-Y. Jung, and H. Kim, "Investigation on the characteristics of the envelope FDTD based on the alternating direction implicit scheme," *IEEE Microwave and Wireless Components Letters*, vol. 13, no. 9, pp. 414–416, Sept. 2003. [Online]. Available: http://dx.doi.org/10.1109/LMWC.2003.815696

[139] T. Namiki and K. Ito, "Investigation of numerical errors of the two-dimensional ADI-FDTD method [for Maxwell's equations solution]," *IEEE Transactions on Microwave Theory and Techniques*, vol. 48, no. 11, pp. 1950–1956, Nov. 2000. [Online]. Available: http://dx.doi.org/10.1109/22.883876

[140] H. Rao, R. Scarmozzino, and R. M. Osgood, "An improved ADI-FDTD method and its application to photonic simulations," *IEEE Photonics Technology Letters*, vol. 14, no. 4, pp. 477–479, Apr. 2002. [Online]. Available: http://dx.doi.org/10.1109/68.992583

[141] C. T. M. Choi and S.-H. Sun, "Numerical performance and applications of the envelope ADI-FDTD method," *IEEE Transactions on Microwave Theory and Techniques*, vol. 54, no. 1, pp. 256–264, Jan. 2006. [Online]. Available: http://dx.doi.org/10.1109/TMTT.2005.860301

[142] H. G. Brachtendorf, G. Welsch, R. Laur, and A. Bunse-Gerstner, "Numerical steady state analysis of electronic circuits driven by multi-tone signals,"

Electrical Engineering (Archiv für Elektrotechnik), vol. 79, no. 2, pp. 103–112, Apr. 1996. [Online]. Available: http://dx.doi.org/10.1007/BF01232919

[143] E. Ngoya and R. Larchevèque, "Envelop transient analysis: A new method for the transient and steady state analysis of microwave communication circuits and systems," in *IEEE MTT-S International Microwave Symposium Digest*, vol. 3, 17-21 June 1996, pp. 1365–1368. [Online]. Available: http://dx.doi.org/10.1109/MWSYM.1996.512189

[144] J. Roychowdhury, "Analyzing circuits with widely separated time scales using numerical PDE methods," *IEEE Transactions on Circuits and Systems I: Fundamental Theory and Applications*, vol. 48, no. 5, pp. 578–594, May 2001. [Online]. Available: http://dx.doi.org/10.1109/81.922460

[145] R. Pulch and M. Günther, "A method of characteristics for solving multirate partial differential equations in radio frequency application," *Applied Numerical Mathematics*, vol. 42, no. 1-3, pp. 397–409, Aug. 2002. [Online]. Available: http://dx.doi.org/10.1016/S0168-9274(01)00163-5

[146] A. Ramachandran, "Methodologies for transient simulation of hybrid electromagnetic/circuit systems with multiple time scales," Ph.D. dissertation, University of Illinois at Urbana-Champaign, May 2009. [Online]. Available: http://hdl.handle.net/2142/11977

[147] D. Gottlieb and S. A. Orszag, *Numerical Analysis of Spectral Methods: Theory and Applications*. Philadelphia, PA: SIAM (Society for Industrial and Applied Mathematics), 1977.

[148] C. Canuto, M. Y. Hussaini, A. Quarteroni, and T. A. Zang, *Spectral Methods*. Berlin, Germany: Springer, 2006. [Online]. Available: http://dx.doi.org/10.1007/978-3-540-30726-6

[149] L. N. Trefethen, *Spectral Methods in MATLAB*. Philadelphia, PA: SIAM (Society for Industrial and Applied Mathematics), Feb. 2001.

[150] J. P. Boyd, *Chebyshev and Fourier Spectral Methods*, 2nd ed. Mineola, NY: Dover Publications, Dec. 2001.

[151] E. Landau, *Handbuch der Lehre von der Verteilung der Primzahlen.* Leipzig, Germany: Teubner, 1909.

[152] J. Stoer and R. Bulirsch, *Introduction to Numerical Analysis*, 2nd ed. Berlin, Germany: Springer, 1992.

[153] G. H. Golub and C. F. Van Loan, *Matrix Computations*, 3rd ed. Baltimore, MD: The Johns Hopkins University Press, 1996.

[154] Y. Saad, *Iterative Methods for Sparse Linear Systems*, 2nd ed. Philadelphia, PA: SIAM (Society for Industrial and Applied Mathematics), 2003.

[155] J. Huang and K. Wu, "A unified TLM model for wave propagation of electrical and optical structures considering permittivity and permeability tensors," *IEEE Transactions on Microwave Theory and Techniques*, vol. 43, no. 10, pp. 2472–2477, Oct. 1995. [Online]. Available: http://dx.doi.org/10.1109/22.466182

[156] L. R. A. X. de Menezes and W. J. R. Hoefer, "Modeling of general constitutive relationships in SCN TLM," *IEEE Transactions on Microwave Theory and Techniques*, vol. 44, no. 6, pp. 854–861, June 1996. [Online]. Available: http://dx.doi.org/10.1109/22.506444

Appendix A

Derivation of the Modified Maxwell's Equations

This appendix gives a more detailed description on how to obtain Maxwell's equations in their modified form based on the Lagrangian approach presented in Chapter 4.

$$\begin{pmatrix} A_x \\ A_y \\ A_z \end{pmatrix} = \begin{bmatrix} \frac{d\alpha}{dx} & \frac{d\beta}{dx} & \frac{d\gamma}{dx} \\ \frac{d\alpha}{dy} & \frac{d\beta}{dy} & \frac{d\gamma}{dy} \\ \frac{d\alpha}{dz} & \frac{d\beta}{dz} & \frac{d\gamma}{dz} \end{bmatrix} \begin{pmatrix} A_\alpha \\ A_\beta \\ A_\gamma \end{pmatrix} \tag{A.1}$$

We expand Maxwell's equations (2.1)-(2.2) for the source-free case and hence find Ampère's law as

$$\frac{\partial H_x}{\partial t} = \frac{1}{\mu}\Big(\frac{\partial E_y}{\partial z} - \frac{\partial E_z}{\partial y}\Big) \tag{A.2}$$

$$\frac{\partial H_y}{\partial t} = \frac{1}{\mu}\Big(\frac{\partial E_z}{\partial x} - \frac{\partial E_x}{\partial z}\Big) \tag{A.3}$$

$$\frac{\partial H_z}{\partial t} = \frac{1}{\mu}\Big(\frac{\partial E_x}{\partial y} - \frac{\partial E_y}{\partial x}\Big), \tag{A.4}$$

and Faraday's law as

$$\frac{\partial E_x}{\partial t} = \frac{1}{\varepsilon}\Big(\frac{\partial H_z}{\partial y} - \frac{\partial H_y}{\partial z}\Big) \tag{A.5}$$

$$\frac{\partial E_y}{\partial t} = \frac{1}{\varepsilon}\Big(\frac{\partial H_x}{\partial z} - \frac{\partial H_z}{\partial x}\Big) \tag{A.6}$$

$$\frac{\partial E_z}{\partial t} = \frac{1}{\varepsilon}\Big(\frac{\partial H_y}{\partial x} - \frac{\partial H_x}{\partial y}\Big). \tag{A.7}$$

Using the map of (A.1) we obtain for (A.2)-(A.4)

$$\frac{\partial H_x}{\partial t} = \frac{1}{\mu}\Big(\frac{\partial}{\partial z}(\frac{\partial \alpha}{\partial y}E_\alpha + \frac{\partial \beta}{\partial y}E_\beta + \frac{\partial \gamma}{\partial y}E_\gamma) - \frac{\partial}{\partial y}(\frac{\partial \alpha}{\partial z}E_\alpha + \frac{\partial \beta}{\partial z}E_\beta + \frac{\partial \gamma}{\partial z}E_\gamma)\Big) \tag{A.8}$$

$$\frac{\partial H_y}{\partial t} = \frac{1}{\mu}\Big(\frac{\partial}{\partial x}(\frac{\partial \alpha}{\partial z}E_\alpha + \frac{\partial \beta}{\partial z}E_\beta + \frac{\partial \gamma}{\partial z}E_\gamma) - \frac{\partial}{\partial z}(\frac{\partial \alpha}{\partial x}E_\alpha + \frac{\partial \beta}{\partial x}E_\beta + \frac{\partial \gamma}{\partial x}E_\gamma)\Big) \tag{A.9}$$

$$\frac{\partial H_z}{\partial t} = \frac{1}{\mu}\Big(\frac{\partial}{\partial y}(\frac{\partial \alpha}{\partial x}E_\alpha + \frac{\partial \beta}{\partial x}E_\beta + \frac{\partial \gamma}{\partial x}E_\gamma) - \frac{\partial}{\partial x}(\frac{\partial \alpha}{\partial y}E_\alpha + \frac{\partial \beta}{\partial y}E_\beta + \frac{\partial \gamma}{\partial y}E_\gamma)\Big)\,. \tag{A.10}$$

For the partial derivative of a vector $\boldsymbol{A}$ in the reference system $\{\hat{\alpha}, \hat{\beta}, \hat{\gamma}\}$ with respect to the spatial coordinates in the system of $\{\hat{x}, \hat{y}, \hat{z}\}$, we find

$$\frac{\partial A_\alpha}{\partial x} = \frac{\partial \alpha}{\partial x}\frac{\partial A_\alpha}{\partial \alpha} + \frac{\partial \beta}{\partial x}\frac{\partial A_\alpha}{\partial \beta} + \frac{\partial \gamma}{\partial x}\frac{\partial A_\alpha}{\partial \gamma}\,. \tag{A.11}$$

Using this relation in (A.8)-(A.10) yields

$$\begin{aligned}
\frac{\partial H_x}{\partial t} = \frac{1}{\mu}\Big(&\frac{\partial E_\alpha}{\partial \alpha}(\frac{\partial \alpha}{\partial y}\frac{\partial \alpha}{\partial z} - \frac{\partial \alpha}{\partial z}\frac{\partial \alpha}{\partial y}) + \frac{\partial E_\alpha}{\partial \beta}(\frac{\partial \alpha}{\partial y}\frac{\partial \beta}{\partial z} - \frac{\partial \alpha}{\partial z}\frac{\partial \beta}{\partial y}) + \\
&\frac{\partial E_\alpha}{\partial \gamma}(\frac{\partial \alpha}{\partial y}\frac{\partial \gamma}{\partial z} - \frac{\partial \alpha}{\partial z}\frac{\partial \gamma}{\partial y}) + \frac{\partial E_\beta}{\partial \alpha}(\frac{\partial \beta}{\partial y}\frac{\partial \alpha}{\partial z} - \frac{\partial \beta}{\partial z}\frac{\partial \alpha}{\partial y}) + \\
&\frac{\partial E_\beta}{\partial \beta}(\frac{\partial \beta}{\partial y}\frac{\partial \beta}{\partial z} - \frac{\partial \beta}{\partial z}\frac{\partial \beta}{\partial y}) + \frac{\partial E_\beta}{\partial \gamma}(\frac{\partial \beta}{\partial y}\frac{\partial \gamma}{\partial z} - \frac{\partial \beta}{\partial z}\frac{\partial \gamma}{\partial y}) + \\
&\frac{\partial E_\gamma}{\partial \alpha}(\frac{\partial \gamma}{\partial y}\frac{\partial \alpha}{\partial z} - \frac{\partial \gamma}{\partial z}\frac{\partial \alpha}{\partial y}) + \frac{\partial E_\gamma}{\partial \beta}(\frac{\partial \gamma}{\partial y}\frac{\partial \beta}{\partial z} - \frac{\partial \gamma}{\partial z}\frac{\partial \beta}{\partial y}) + \\
&\frac{\partial E_\gamma}{\partial \gamma}(\frac{\partial \gamma}{\partial y}\frac{\partial \gamma}{\partial z} - \frac{\partial \gamma}{\partial z}\frac{\partial \gamma}{\partial y})\Big) \\
&= \frac{1}{\mu}\Big((D^{\alpha\beta}_{yz}\frac{\partial}{\partial \beta} + D^{\alpha\gamma}_{yz}\frac{\partial}{\partial \gamma})E_\alpha + (-D^{\alpha\beta}_{yz}\frac{\partial}{\partial \alpha} + D^{\beta\gamma}_{yz}\frac{\partial}{\partial \gamma})E_\beta + \\
&(-D^{\alpha\gamma}_{yz}\frac{\partial}{\partial \alpha} - D^{\beta\gamma}_{yz}\frac{\partial}{\partial \beta})E_\gamma)\Big)\,,
\end{aligned} \tag{A.12}$$

$$
\begin{aligned}
\frac{\partial H_y}{\partial t} = \frac{1}{\mu}\Big(& \frac{\partial E_\alpha}{\partial \alpha}\Big(\frac{\partial \alpha}{\partial z}\frac{\partial \alpha}{\partial x} - \frac{\partial \alpha}{\partial x}\frac{\partial \alpha}{\partial z}\Big) + \frac{\partial E_\alpha}{\partial \beta}\Big(\frac{\partial \alpha}{\partial z}\frac{\partial \beta}{\partial x} - \frac{\partial \alpha}{\partial x}\frac{\partial \beta}{\partial z}\Big) + \\
& \frac{\partial E_\alpha}{\partial \gamma}\Big(\frac{\partial \alpha}{\partial z}\frac{\partial \gamma}{\partial x} - \frac{\partial \alpha}{\partial x}\frac{\partial \gamma}{\partial z}\Big) + \frac{\partial E_\beta}{\partial \alpha}\Big(\frac{\partial \beta}{\partial z}\frac{\partial \alpha}{\partial x} - \frac{\partial \beta}{\partial x}\frac{\partial \alpha}{\partial z}\Big) + \\
& \frac{\partial E_\beta}{\partial \beta}\Big(\frac{\partial \beta}{\partial z}\frac{\partial \beta}{\partial x} - \frac{\partial \beta}{\partial x}\frac{\partial \beta}{\partial z}\Big) + \frac{\partial E_\beta}{\partial \gamma}\Big(\frac{\partial \beta}{\partial z}\frac{\partial \gamma}{\partial x} - \frac{\partial \beta}{\partial x}\frac{\partial \gamma}{\partial z}\Big) + \\
& \frac{\partial E_\gamma}{\partial \alpha}\Big(\frac{\partial \gamma}{\partial z}\frac{\partial \alpha}{\partial x} - \frac{\partial \gamma}{\partial x}\frac{\partial \alpha}{\partial z}\Big) + \frac{\partial E_\gamma}{\partial \beta}\Big(\frac{\partial \gamma}{\partial z}\frac{\partial \beta}{\partial x} - \frac{\partial \gamma}{\partial x}\frac{\partial \beta}{\partial z}\Big) + \\
& \frac{\partial E_\gamma}{\partial \gamma}\Big(\frac{\partial \gamma}{\partial z}\frac{\partial \gamma}{\partial x} - \frac{\partial \gamma}{\partial x}\frac{\partial \gamma}{\partial z}\Big)\Big) \\
& = \frac{1}{\mu}\Big(\Big(-D_{xz}^{\alpha\beta}\frac{\partial}{\partial \beta} - D_{xz}^{\alpha\gamma}\frac{\partial}{\partial \gamma}\Big)E_\alpha + \Big(D_{xz}^{\alpha\beta}\frac{\partial}{\partial \alpha} - D_{xz}^{\beta\gamma}\frac{\partial}{\partial \gamma}\Big)E_\beta + \\
& \Big(D_{xz}^{\alpha\gamma}\frac{\partial}{\partial \alpha} + D_{xz}^{\beta\gamma}\frac{\partial}{\partial \beta}\Big)E_\gamma\Big)\Big),
\end{aligned}
\tag{A.13}
$$

$$
\begin{aligned}
\frac{\partial H_z}{\partial t} = \frac{1}{\mu}\Big(& \frac{\partial E_\alpha}{\partial \alpha}\Big(\frac{\partial \alpha}{\partial x}\frac{\partial \alpha}{\partial y} - \frac{\partial \alpha}{\partial y}\frac{\partial \alpha}{\partial x}\Big) + \frac{\partial E_\alpha}{\partial \beta}\Big(\frac{\partial \alpha}{\partial x}\frac{\partial \beta}{\partial y} - \frac{\partial \alpha}{\partial y}\frac{\partial \beta}{\partial x}\Big) + \\
& \frac{\partial E_\alpha}{\partial \gamma}\Big(\frac{\partial \alpha}{\partial x}\frac{\partial \gamma}{\partial y} - \frac{\partial \alpha}{\partial y}\frac{\partial \gamma}{\partial x}\Big) + \frac{\partial E_\beta}{\partial \alpha}\Big(\frac{\partial \beta}{\partial x}\frac{\partial \alpha}{\partial y} - \frac{\partial \beta}{\partial y}\frac{\partial \alpha}{\partial x}\Big) + \\
& \frac{\partial E_\beta}{\partial \beta}\Big(\frac{\partial \beta}{\partial x}\frac{\partial \beta}{\partial y} - \frac{\partial \beta}{\partial y}\frac{\partial \beta}{\partial x}\Big) + \frac{\partial E_\beta}{\partial \gamma}\Big(\frac{\partial \beta}{\partial x}\frac{\partial \gamma}{\partial y} - \frac{\partial \beta}{\partial y}\frac{\partial \gamma}{\partial x}\Big) + \\
& \frac{\partial E_\gamma}{\partial \alpha}\Big(\frac{\partial \gamma}{\partial x}\frac{\partial \alpha}{\partial y} - \frac{\partial \gamma}{\partial y}\frac{\partial \alpha}{\partial x}\Big) + \frac{\partial E_\gamma}{\partial \beta}\Big(\frac{\partial \gamma}{\partial x}\frac{\partial \beta}{\partial y} - \frac{\partial \gamma}{\partial y}\frac{\partial \beta}{\partial x}\Big) + \\
& \frac{\partial E_\gamma}{\partial \gamma}\Big(\frac{\partial \gamma}{\partial x}\frac{\partial \gamma}{\partial y} - \frac{\partial \gamma}{\partial y}\frac{\partial \gamma}{\partial x}\Big)\Big) \\
& = \frac{1}{\mu}\Big(\Big(D_{xy}^{\alpha\beta}\frac{\partial}{\partial \beta} + D_{xy}^{\alpha\gamma}\frac{\partial}{\partial \gamma}\Big)E_\alpha + \Big(-D_{xy}^{\alpha\beta}\frac{\partial}{\partial \alpha} + D_{xy}^{\beta\gamma}\frac{\partial}{\partial \gamma}\Big)E_\beta + \\
& \Big(-D_{xy}^{\alpha\gamma}\frac{\partial}{\partial \alpha} - D_{xy}^{\beta\gamma}\frac{\partial}{\partial \beta}\Big)E_\gamma\Big)\Big),
\end{aligned}
\tag{A.14}
$$

where we have defined

$$
D_{xy}^{\alpha\beta} := \frac{\partial(\alpha,\beta)}{\partial(x,y)} := \det\begin{pmatrix} \alpha_x & \alpha_y \\ \beta_x & \beta_y \end{pmatrix}. \tag{A.15}
$$

Next, we define

$$\tilde{\mathcal{D}} = \begin{bmatrix} -D_{yz}^{\beta\gamma} & D_{yz}^{\alpha\gamma} & -D_{yz}^{\alpha\beta} \\ D_{xz}^{\beta\gamma} & -D_{xz}^{\alpha\gamma} & D_{xz}^{\alpha\beta} \\ -D_{xy}^{\beta\gamma} & D_{xy}^{\alpha\gamma} & -D_{xy}^{\alpha\beta} \end{bmatrix}, \tag{A.16}$$

which allows us to modify Maxwell's equations describing Ampère's law to the form

$$\frac{\partial}{\partial t}\begin{pmatrix} H_x \\ H_y \\ H_z \end{pmatrix} = \frac{1}{\mu}\tilde{D}\begin{bmatrix} 0 & -\frac{\partial}{\partial\gamma} & \frac{\partial}{\partial\beta} \\ \frac{\partial}{\partial\gamma} & 0 & -\frac{\partial}{\partial\alpha} \\ -\frac{\partial}{\partial\beta} & \frac{\partial}{\partial\alpha} & 0 \end{bmatrix}\begin{pmatrix} E_\alpha \\ E_\beta \\ E_\gamma \end{pmatrix} \tag{A.17}$$

$$= \frac{1}{\mu}\tilde{\mathcal{D}}\Big(\begin{pmatrix} \frac{\partial}{\partial\alpha} \\ \frac{\partial}{\partial\beta} \\ \frac{\partial}{\partial\gamma} \end{pmatrix} \times \begin{pmatrix} E_\alpha \\ E_\beta \\ E_\gamma \end{pmatrix}\Big). \tag{A.18}$$

Considering that the H field components are mapped from the $\{\hat{\alpha}, \hat{\beta}, \hat{\gamma}\}$ system to the system of $\{\hat{x}, \hat{y}, \hat{z}\}$ by

$$\begin{pmatrix} H_x \\ H_y \\ H_z \end{pmatrix} = \mathcal{F}\begin{pmatrix} H_\alpha \\ H_\beta \\ H_\gamma \end{pmatrix}, \tag{A.19}$$

with

$$\mathcal{F} = \begin{bmatrix} \frac{\partial\alpha}{\partial x} & \frac{\partial\beta}{\partial x} & \frac{\partial\gamma}{\partial x} \\ \frac{\partial\alpha}{\partial y} & \frac{\partial\beta}{\partial y} & \frac{\partial\gamma}{\partial y} \\ \frac{\partial\alpha}{\partial z} & \frac{\partial\beta}{\partial z} & \frac{\partial\gamma}{\partial z} \end{bmatrix}, \tag{A.20}$$

we obtain the modified equations of the Lagrangian mapping method

$$\frac{\partial}{\partial t}\begin{pmatrix} H_\alpha \\ H_\beta \\ H_\gamma \end{pmatrix} = \frac{1}{\mu}\mathcal{F}^{-1}\tilde{\mathcal{D}}\Big(\nabla \times \begin{pmatrix} E_\alpha \\ E_\beta \\ E_\gamma \end{pmatrix}\Big). \tag{A.21}$$

The remaining equations based on Faraday's law are obtained mutatis mutandis.

Author's Biography

Johannes Anton Russer received his Diplom Ingenieur degree in electrical engineering and information technology from the Universität Karlsruhe, Germany, in 2003. In the same year he was a visiting scholar at the University of Colorado at Boulder while working on an optically controlled phase shifter for his diploma thesis. In 2004 he joined the University of Illinois at Urbana-Champaign as a research assistant in pursuit of his Ph.D. degree. Since 2007 he has been working for Qualcomm Inc. as an intern. In 2008 he won second place in the student paper competition of the IEEE MTT-S International Microwave Symposium in Atlanta. He has authored eight papers published at international conferences or in refereed journals. He is a member of the Institute of Electrical and Electronics Engineers, of the VDE-ITG (German Association for Electrical, Electronic and Information Technologies), and of the Eta Kappa Nu honor society.